National Library of Canada
Bibliothèque nationale du Canada

Canadian Theses Service
Service des thèses canadiennes

Ottawa, Canada
K1A 0N4

NOTICE

The quality of this microform is heavily dependent upon the quality of the original thesis submitted for microfilming. Every effort has been made to ensure the highest quality of reproduction possible.

If pages are missing, contact the university which granted the degree.

Some pages may have indistinct print especially if the original pages were typed with a poor typewriter ribbon or if the university sent us an inferior photocopy.

Reproduction in full or in part of this microform is governed by the Canadian Copyright Act, R.S.C. 1970, c. C-30, and subsequent amendments.

AVIS

La qualité de cette microforme dépend grandement de la qualité de la thèse soumise au microfilmage. Nous avons tout fait pour assurer une qualité supérieure de reproduction.

S'il manque des pages, veuillez communiquer avec l'université qui a conféré le grade.

La qualité d'impression de certaines pages peut laisser à désirer, surtout si les pages originales ont été dactylographiées à l'aide d'un ruban usé ou si l'université nous a fait parvenir une photocopie de qualité inférieure.

La reproduction, même partielle, de cette microforme est soumise à la Loi canadienne sur le droit d'auteur, SRC 1970, c. C-30, et ses amendements subséquents.

NL-339 (r. 88/04) c

Canada

UNIVERSITY OF ALBERTA

Evaluation and Modification of Electron Beam Treatment Planning Algorithms

by

John Anthony Antolak

©

A thesis submitted to the Faculty of Graduate Studies and Research in partial fulfillment of the requirements for the degree of Doctor of Philosophy

in

Medical Physics.

Department Of Physics

Edmonton, Alberta

Spring 1992

National Library of Canada
Bibliothèque nationale du Canada

Canadian Theses Service
Service des thèses canadiennes

Ottawa, Canada
K1A 0N4

The author has granted an irrevocable non-exclusive licence allowing the National Library of Canada to reproduce, loan, distribute or sell copies of his/her thesis by any means and in any form or format, making this thesis available to interested persons.

L'auteur a accordé une licence irrévocable et non exclusive permettant à la Bibliothèque nationale du Canada de reproduire, prêter, distribuer ou vendre des copies de sa thèse de quelque manière et sous quelque forme que ce soit pour mettre des exemplaires de cette thèse à la disposition des personnes intéressées.

The author retains ownership of the copyright in his/her thesis. Neither the thesis nor substantial extracts from it may be printed or otherwise reproduced without his/her permission.

L'auteur conserve la propriété du droit d'auteur qui protège sa thèse. Ni la thèse ni des extraits substantiels de celle-ci ne doivent être imprimés ou autrement reproduits sans son autorisation.

ISBN 0-315-73083-8

Canada

UNIVERSITY OF ALBERTA

RELEASE FORM

NAME OF AUTHOR: **John Anthony Antolak**

TITLE OF THESIS: **Evaluation and Modification of Electron Beam Treatment Planning Algorithms**

DEGREE: **Doctor of Philosophy**

YEAR THIS DEGREE GRANTED: **1992**

Permission is hereby granted to the University of Alberta Library to reproduce single copies of this thesis and to lend or sell such copies for private, scholarly, or scientific research purposes only.

The author reserves all other publication and other rights in association with the copyright in the thesis, and except as hereinbefore provided neither the thesis or any substantial portion thereof may be printed or otherwise reproduced in any material form whatever without the author's prior written permission.

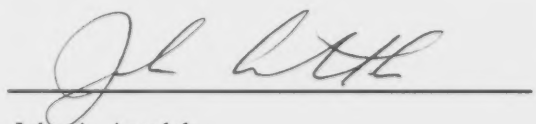

John A. Antolak
6044-105 Street
Edmonton, Alberta
Canada T6H 2N4

April 21, 1992

The whole of science is nothing more than a refinement of everyday thinking.

A. Einstein, 1936

UNIVERSITY OF ALBERTA

FACULTY OF GRADUATE STUDIES AND RESEARCH

The undersigned certify that they have read, and recommend to the Faculty of Graduate Studies and Research for acceptance, a thesis entitled **Evaluation and Modification of Electron Beam Treatment Planning Algorithms** submitted by **John Anthony Antolak** in partial fulfillment of the requirements for the degree of Doctor of Philosophy in Medical Physics.

Dr. J.W. Scrimger

Dr. G. Roy

Dr. Z.W. Gortel

Dr. H.R. Hooper

Dr. R. Pearcey

Dr. K.R. Hogstrom

March 27, 1992

Dedication

I dedicate this thesis to my loving wife, Debbie, and our (soon to be two) children. They have supported my efforts in many ways, too numerous to mention. Together, we have come to realize that the most important thing in life is the love and caring that we have for each other and those around us.

Debbie, I thank you for the years we have had together, and a lifetime to follow.

Abstract

Megavoltage electron beams are commonly used for radiotherapy treatment due in part to their advantageous dose deposition characteristics. Because electrons interact heavily with the electromagnetic field of the medium traversed, electron beams have a characteristic maximum penetration into the material, which is quite shallow compared to megavoltage photon beams.

This thesis deals mainly with the experimental verification and further development of the electron dose calculation algorithms implemented in the Alberta Treatment Planning (ATP) system (Battista *et al* 1984). The stationary beam algorithm is based on the pencil beam algorithm developed at the M.D. Anderson Hospital (MDAH) by Hogstrom *et al* (1981). The theory on which the algorithm is based is reviewed, and the necessary approximations in the theory and its computer implementation are discussed.

Chapter III presents of a series of three studies investigating the performance of the stationary beam algorithm. Experimental data is presented which shows that the MDAH algorithm performs reasonably well, but has deficiencies in certain circumstances. The progression of phantoms from 2D to 3D geometry is also discussed, with implications for 3D treatment planning.

The MDAH arc electron pencil beam algorithm (Hogstrom *et al* 1989) is validated in chapter IV. The results show some systematic discrepancies compared to measurement. A qualitative argument is presented to show that the discrepancies occur as a result of the algorithm's failure to model both large angle scattering and range straggling of the electrons.

The final component of the thesis presents an empirical solution to the problem of range straggling in the MDAH algorithms. The solution is similar to methods proposed by Werner *et al* (1982) and Lax *et al* (1983), but is derived from measured data. Incorporating

the empirical modification into the stationary beam and arc electron algorithms gives better agreement with measurement for homogeneous phantoms. Monte Carlo experiments show that this method is valid for heterogeneous slab media, which implies that the empirical modification should apply to heterogeneous phantoms.

Acknowledgements

I would like to acknowledge some of the people who have guided and supported my efforts through the years. First of all, I want to thank my supervisor, Dr. J.W. Scrimger, who made me feel that a Ph.D. in Medical Physics was worth pursuing, and gave me plenty of moral support. The whole physics staff at the Cross Cancer Institute were a joy to work with, and I appreciate the technical help that was provided.

I am grateful to the physics department at the University of Alberta, especially Mrs. H. Biltek and Ms. L. Chandler for ensuring that all of the forms were filled in correctly and on time through my undergraduate and graduate years. I also appreciated the experience gained as a graduate teaching assistant in the physics department.

I would like to thank all of the members of my graduate committee, who were very helpful and kept me on my toes. I would especially like to thank Dr. K.R. Hogstrom. Despite pressing personal obligations, his comments and questions regarding this thesis were very thorough and appreciated by the rest of the examination committee. His willingness to discuss the progress of the research, at several times in the past, was very much appreciated.

I would also like to acknowledge the financial support of the Natural Sciences and Engineering Research Council, the Alberta Heritage Fund for Medical Research, and the University of Alberta Department of Physics.

Last, but certainly not least, I would like to thank my family, parents, and in-laws, for their prayers and good wishes for the successful completion of this Ph.D. program. I hope they all know how much their love and support means to me.

Table of Contents

I. Introduction 1

II. Theory 9

A. Scattering Power 9

B. Stopping Power 10

C. Dose Calculation 11

1. General equation 11

2. Monte Carlo methods 12

D. Fermi-Eyges Theory 14

1. Fermi's derivation 15

2. Eyges' extension to Fermi scattering 17

E. MDAH Algorithm 19

1. Stationary electron beams 19

2. Arced electron beams 24

F. Other Algorithms 26

III. Stationary Beams 28

A. Wax Phantoms 28

1. Experimental method 28

2. Results and discussion 34

B. Polystyrene Phantoms 44

1. Experimental method 44

2. Results and discussion 48

C. Anthropomorphic Phantom 65

1. Statement of problem 65

2. Method and results 65

3. Results and discussion 73

D. Conclusion 75

IV. Arc Electron Beams 78

A. Introduction 78

B. Experimental Method 78

C. Homogeneous Phantom 83

D. Lung Phantom 91

E. Discussion 95

V. Range Straggling Modification 102

A. Introduction 102

B. Empirical Modification of the Pencil Beam Width 105

1. *FMCS* modification 105

2. Scattering power modification 108

C. Monte Carlo Results 112

1. Homogeneous phantoms 113

2. Heterogeneous phantoms 116

D. Application to Clinical Beams 121

VI. Conclusion 131

References 134

List of Tables

III.1 Experimental wax phantoms 33

III.2 The maximum discrepancies between measurement and calculation for a 1 cm rod in polystyrene for 10 MeV and 18 MeV electrons 62

List of Figures

I.1 Percentage depth dose for 16 MeV beam showing parameters characterizing the depth dose....2

I.2 Schematic diagram of the electron beam subsystem for stationary electron beams....4

I.3 Schematic diagram of a typical medical linear accelerator showing the geometric relationship and possible motions of the major components....6

III.1 Schematic diagram of the setup used for measuring dose profiles behind wax phantoms with high and/or low density inclusions....29

III.2 Diode angular response, normalized to the response at 0°....31

III.3 Comparison of measured and calculated isodoses for a 10×10 cm^2 beam of 10 MeV electrons incident on a water phantom....32

III.4 Lateral dose profiles beyond a single 'long rib' in water....35

III.5 Lateral dose profiles beyond two 'long ribs' separated by 1 cm....37

III.6 Lateral dose profiles beyond two 'short ribs' separated by 1 cm....39

III.7 Lateral dose profiles beyond a single 'vertebral body'....40

III.8 Lateral dose profiles beyond the spine'....42

III.9 Lateral dose profiles beyond the 'trachea' and 'spine'....43

III.10 Schematic diagram of the setup used for measuring dose distributions behind polystyrene phantoms with high density inclusions....45

III.11 The data acquisition and analysis system used for measuring dose distributions with the polystyrene phantoms....47

III.12 Dose distribution behind a 1 cm long aluminum rod irradiated by a 10 cm square field of 10 MeV electrons (measured vs. 2D calculation)....50

III.13 Dose distribution behind a 1 cm long aluminum rod irradiated by a 10 cm square field of 10 MeV electrons (measured vs. 3D calculation)....51

III.14 Dose distribution behind a 1 cm long hard bone rod irradiated by a 10 cm square field of 10 MeV electrons (measured vs. 2D calculation)....52

III.15 Dose distribution behind a 1 cm long hard bone rod irradiated by a 10 cm square field of 10 MeV electrons (measured vs. 3D calculation)....53

III.16 Dose distribution behind a 1 cm long soft bone rod irradiated by a 10 cm square field of 10 MeV electrons (measured vs. 2D calculation)....54

III.17 Dose distribution behind a 1 cm long soft bone rod irradiated by a 10 cm square field of 10 MeV electrons (measured vs. 3D calculation)..... 55

III.18 Dose distribution behind a 1 cm long aluminum rod irradiated by a 10 cm square field of 18 MeV electrons (measured vs. 2D calculation)..... 56

III.19 Dose distribution behind a 1 cm long aluminum rod irradiated by a 10 cm square field of 18 MeV electrons (measured vs. 3D calculation)..... 57

III.20 Dose distribution behind a 1 cm long hard bone rod irradiated by a 10 cm square field of 18 MeV electrons (measured vs. 2D calculation)..... 58

III.21 Dose distribution behind a 1 cm long hard bone rod irradiated by a 10 cm square field of 18 MeV electrons (measured vs. 3D calculation)..... 59

III.22 Dose distribution behind a 1 cm long soft bone rod irradiated by a 10 cm square field of 18 MeV electrons (measured vs. 2D calculation)..... 60

III.23 Dose distribution behind a 1 cm long soft bone rod irradiated by a 10 cm square field of 18 MeV electrons (measured vs. 3D calculation)..... 61

III.24 Mean of the squares of the differences between the measured 10 cm rod dose distribution for 10 MeV, and the measured dose distributions for other lengths 64

III.25 Mean of the squares of the differences between the calculated 10 cm rod dose distribution for 10 MeV, and the calculated dose distributions for other lengths 64

III.26 Treatment plan for thyroid, in the central plane with no bolus..... 67

III.27 Treatment plan for thyroid, in the central plane with 'old' bolus..... 68

III.28 Treatment plan for thyroid, in the central plane with 'optimized' bolus 69

III.29 Sagital view of the optimized bolus contour 71

III.30 Comparison of calculated dose profile at a depth of 5.7 cm under the bolus of figure III.28 (in a wax phantom), to point measurements (TLD-100 LiF chips) at the same depth 72

III.31 Monte Carlo simulation of a central axis percentage depth dose for 16 MeV electrons, incident on a water phantom 74

IV.1 Schematic diagram of the reference beam setup for arc electron beams..... 79

IV.2 Schematic diagram of the polystyrene phantom used for film measurements in arc electron beams 81

IV.3 Schematic diagram of the water phantom used for measurements in arc electron beams 82

IV.4 Percentage depth doses for 0° arcs on a 17.5 cm radius water (or polystyrene) phantom, for nominal energies of 6, 12, and 20 MeV 84

IV.5 Mid-arc percentage depth dose for a 6 MeV 90° arc on a 17.5 cm radius phantom 85

IV.6 Mid-arc percentage depth dose for a 12 MeV 90° arc on a 17.5 cm radius phantom 86

IV.7 Mid-arc percentage depth dose for a 12 MeV 145° arc on a 17.5 cm radius phantom 87

IV.8 Mid-arc percentage depth dose for a 16 MeV 90° arc on a 17.5 cm radius phantom 89

IV.9 Mid-arc percentage depth dose for a 20 MeV 90° arc on a 17.5 cm radius phantom 90

IV.10 Calculated and measured (film) isodose lines for a 90° arc of 12 MeV electrons incident on a 17.5 cm radius polystyrene phantom 92

IV.11 Schematic representation of the lung phantom geometry 93

IV.12 Calculated and measured doses profiles for a 12 MeV, 80° arc incident on the lung phantom 94

IV.13 Calculated and measured doses profiles for a 16 MeV, 80° arc incident on the lung phantom 96

IV.14 Calculated and measured doses profiles for a 20 MeV, 80° arc incident on the lung phantom 97

IV.15 The percentage depth dose for a 90° arc of 16 MeV electrons incident on a 17.5 cm radius water phantom, as the multiple Coulomb scattering factor, *FMCS*, varies from 1.0 to 1.4 100

V.1 Pencil beam width for 12 MeV electrons incident on a water phantom 103

V.2 Percentage depth dose for 12 MeV electrons incident on a water phantom, for various densities of water 107

V.3 Lateral dose distribution for 12 MeV electrons incident on a homogeneous water phantom of varying density 107

V.4 Comparison of multiplicative pencil beam width correction factors calculated for a 12 MeV monoenergetic electron beam 114

V.5 Comparison of pencil beam width corrections calculated for a 12 MeV monoenergetic electron beam incident on a water phantom 114

V.6 Comparison of scattering power used by the scattering power correction to ICRU scattering powers 117

V.7 Calculated pencil beam widths for 12 MeV electrons incident on a water phantom composed of 1 cm of unit density water followed by water of density 0.8 g/cm^3 119

V.8 Calculated pencil beam widths for 12 MeV electrons incident on a water phantom composed of 1 cm of unit density water followed by water of density 1.25 g/cm^3 119

V.9 Calculated pencil beam widths for 12 MeV electrons incident on a water phantom composed of 1 cm of unit density water followed by water of density 2.0 g/cm^3 120

V.10 Calculated pencil beam widths for 12 MeV electrons incident on a water phantom composed of 1 cm of unit density water followed by water of density 0.32 g/cm^3 120

V.11 Pencil beam widths for a clinical electron beam 123

V.12 *FMCS* correction parameter, $\xi(z')$, for the range of electron energies available from a Varian 2100C linear accelerator 123

V.13 Isodose lines for a 10×10 cm^2 field of 16 MeV electrons incident on a water phantom 125

V.14 Mid-arc percentage depth dose for a 16 MeV 90° arc on a 17.5 cm radius phantom 126

V.15 Mid-arc percentage depth dose for a 20 MeV 90° arc on a 17.5 cm radius phantom 127

V.16 Calculated and measured (film) isodose lines for a 90° arc of 12 MeV electrons incident on a 17.5 cm radius polystyrene phantom 129

I. Introduction

Megavoltage electron beams are commonly used for radiotherapy treatment, because of their advantageous dose deposition characteristics. Microscopically, both photons and electrons deposit energy in the same way, by setting electrons in motion. Macroscopically, the energy deposition occurs very differently. Because they are uncharged, high energy photons can penetrate a large amount of material before interacting and depositing energy. Electrons, on the other hand, interact heavily with the electromagnetic field of the medium traversed, and have a characteristic maximum penetration into the material.

Figure I.1 shows a percentage depth dose (pdd) for a 16 MeV electron beam incident on a water phantom. The horizontal axis is the depth in the water phantom, and the vertical axis is the dose deposited (energy per unit mass) in the water, normalized to a maximum of 100%. The surface dose (D_s) is generally between 70–95% for clinical electron beams. The dose rapidly reaches a maximum (at R_{100}) within a few centimeters, and then falls off quickly to an approximately constant bremsstrahlung 'tail' (D_x). The bremsstrahlung tail consists of photons generated by electron interactions in the head of the treatment machine, and in the water.

The 80% depth (R_{80}) is the maximum depth that can be treated with a dose of 90% ± 10%, and is sometimes referred to as the therapeutic depth. Some radiotherapists prefer better homogeneity of the dose distribution, and therefore prefer the 90% depth (R_{90}). The 50% depth (R_{50}) is approximately proportional to the average energy of the electron beam at the surface of the water phantom (Brahme and Svensson 1976). The practical range (R_p) is indicative of the most probable energy at the surface, and is obtained by finding the depth at which the tangents of the depth dose curve at R_{50} and D_x intersect.

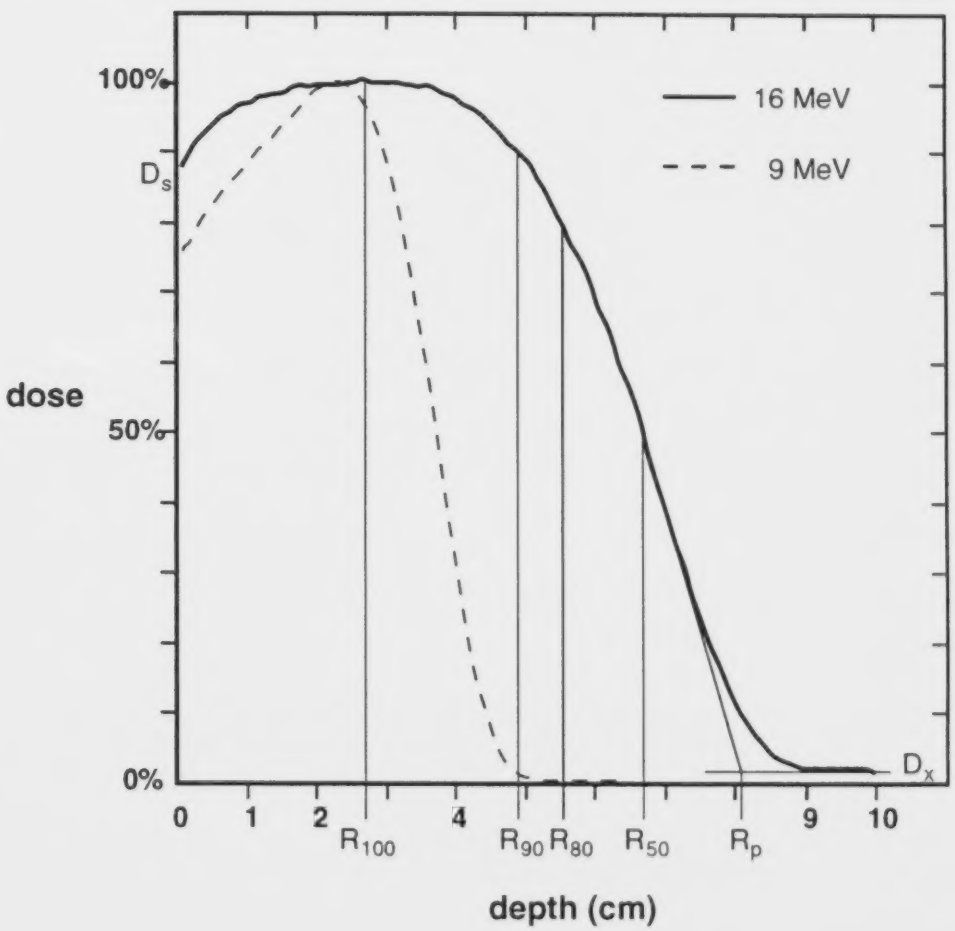

Figure I.1. Percentage depth dose for 16 MeV beam showing parameters characterizing the depth dose. A 9 MeV depth dose is shown for comparison.

Figure I.1 also shows a depth dose curve for a 9 MeV beam as a dashed curve. For a given treatment machine, the surface dose generally increases with increasing initial energy of the beam. The therapeutic depth, 50% depth, and practical range also increase with increasing energy. The higher energy electrons also produce more bremsstrahlung, which implies that D_x also increases with increasing beam energy. The relationship between the incident energy and the parameters D_s, D_x, R_{100}, and R_{80}, is very much dependent on the exact details of the electron beam subsystem, shown in figure I.2.

A narrow beam of megavoltage electrons is produced in an accelerating waveguide (not shown)†, and is delivered to the electron beam subsystem using an electromagnetic optical system. The narrow beam is dispersed by one or two thin scattering foils‡. As an alternative, some manufacturers use magnets to scan a defocussed narrow beam over a broad area. This implies less bremsstrahlung contamination in the beam. The broadened beam then passes through the monitor ion chamber that is used, among other functions, to control the beam's 'on' time. The secondary collimator provides the initial collimation for the electron beam*. The electron applicator attaches to the accessory mount of the LINAC, and provides the final collimation for the beam. The applicator is usually in contact with or very close to the patient. Without the electron applicator, the electron scattering in the air space between the secondary collimation and the patient surface would give a very diffuse beam edge, which is usually not desirable.

The exact configuration and composition of the above components affects the final beam quality. This causes variations of D_s, D_x, R_{100}, and R_{80} from machine to machine, for a given initial beam energy from the accelerating waveguide. For example, if the

---

† Some electron treatment machines use a betatron as a source of high energy electrons.

‡ To produce a photon beam, the scattering foil is removed from the narrow beam's path, and a thick, high atomic number target is introduced into the beam path..

* In some accelerators, the scattering foil is upstream of the primary collimator, as well.

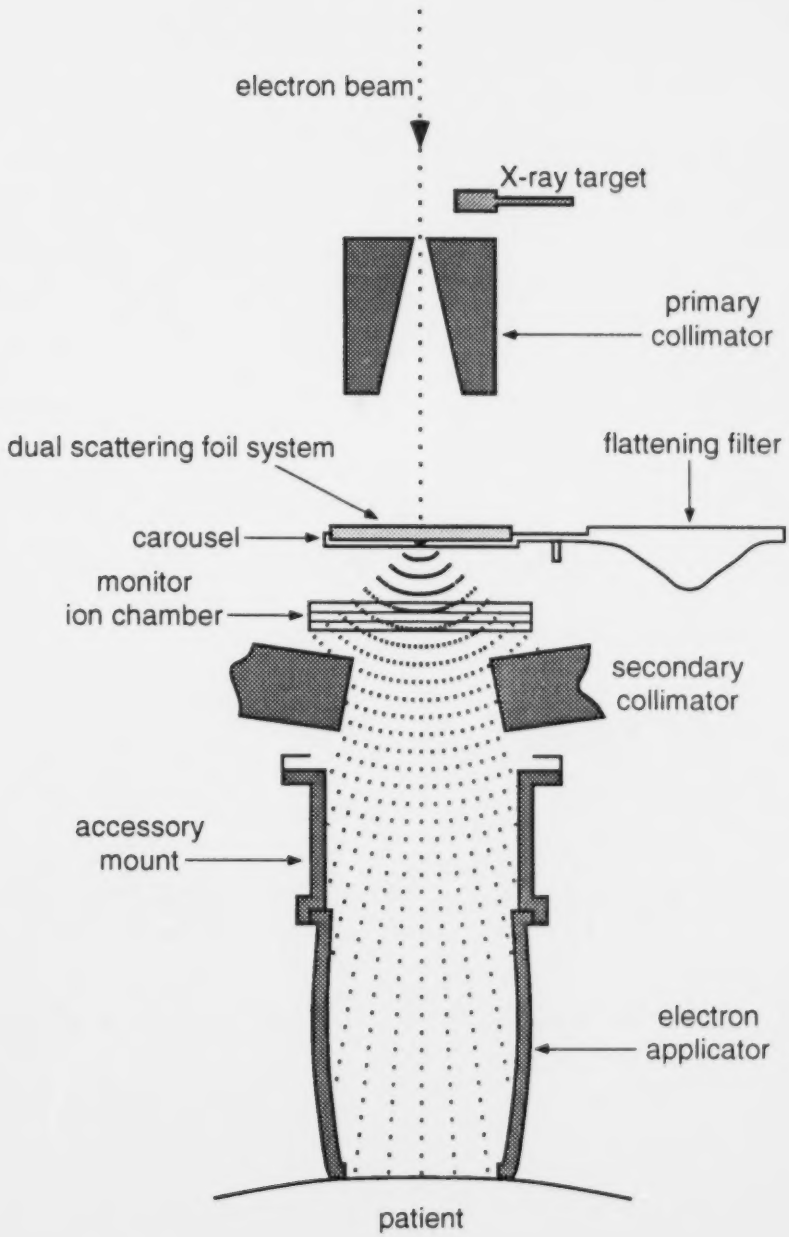

Figure I.2. Schematic diagram of the electron beam subsystem (Varian Clinac 2100C) for stationary electron beams.

scattering foil is chosen to give a more isotropic fluence, then more bremsstrahlung is usually produced. If the scattering foil is thinner, there is less bremsstrahlung contamination, but the fluence is not uniform. The applicator must then be used to scatter electrons into the field, to flatten the dose profile, rather than just collimating the beam. The choice of monitor chamber composition also affects the properties of the electron beam (El Khatib *et al* 1991).

Most modern medical linear accelerators are isocentric machines, and a typical treatment machine geometry is shown in figure I.3. Note that the treatment couch and gantry both rotate about a single point in space, called the isocenter. By positioning a treatment volume at the isocenter, the treatment couch and gantry can be rotated to any position and still maintain the beam axis through the treatment volume. This results in easier multiple field treatments for photon beams. For electrons, however, the penetration of the electron beam is usually insufficient to allow for multiple field treatments. There is also the added complication of the electron applicator that usually comes very close to isocenter, and could interfere with the safe movement from one gantry position to another.

In order to successfully treat a patient, the treatment volume must first be identified, using clinical examination, computed tomography (CT), or a simulator. A simulator is a diagnostic X-ray machine that mimics the gantry and treatment couch movements of the treatment machine. After identifying the treatment volume, the energy and size of the needed electron field are chosen. The energy is chosen by matching the therapeutic depth of the electron beam to the maximum depth of the treatment volume. Similarly, the size of the electron field is chosen to cover the projection of the treatment volume onto a plane perpendicular to the beam axis. If the irradiated tissue is homogeneous and water-like, then treatment can continue. If heterogeneities (e.g., lung, bone) are within the treatment field, or the patient surface is not flat, a calculation of the effect of the heterogeneities and/or surface irregularities should be made. This is usually done on a treatment planning

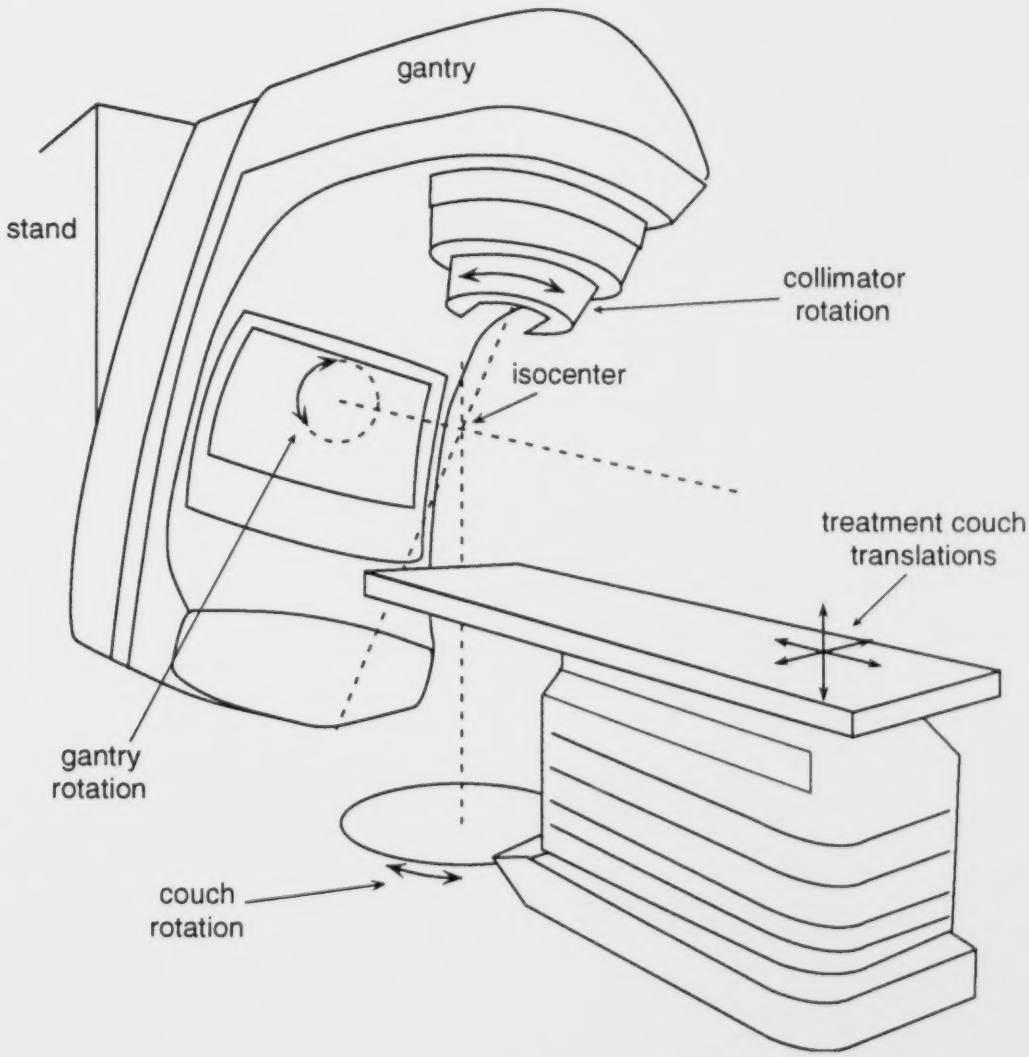

Figure I.3. Schematic diagram of a typical medical linear accelerator showing the geometric relationship and possible motions of the major components.

computer, and may lead to modification of the treatment geometry to produce the desired dose distribution. The final stage is verification of the dose delivered, which can be measured on the surface of the patient using thermoluminescent crystals (TLD) or small semiconductor detectors.

This thesis deals mainly with the experimental verification and further development of the electron dose calculation algorithms implemented in the Alberta Treatment Planning (ATP) system (Battista *et al* 1984). The stationary beam algorithm is based on the pencil beam algorithm developed at the M.D. Anderson Hospital (MDAH) by Hogstrom *et al* (1981).The next chapter reviews the theory upon which the MDAH algorithm is based. The necessary approximations in the theory and its computer implementation are discussed. Chapter III consists of a series of three studies investigating the performance of the stationary beam algorithm. Experimental data is presented which shows that the MDAH algorithm performs reasonably well, but has deficiencies in certain circumstances. The progression of phantoms from 2D to 3D geometry is also discussed, with implications for 3D treatment planning.

The MDAH arc electron pencil beam algorithm (Hogstrom *et al* 1989) is validated in chapter IV. The results show some systematic discrepancies compared to measurement. A qualitative argument is presented to show that the discrepancies occur as a result of the algorithm's failure to model both large angle scattering and range straggling of the electrons.

An empirical solution to the above problem has been found and is presented in chapter V. The solution is similar to methods proposed by Werner *et al* (1982) and Lax *et al* (1983), but is derived from measured data. Incorporating the empirical modification into the stationary beam and arc electron algorithms gives better agreement with measurement for homogeneous phantoms. Monte Carlo experiments show that this method is valid for

heterogeneous slab media, which implies that the empirical modification should be valid for heterogeneous phantoms.

II. Theory

Electron transport is a very complicated process. Because of the small mass of the electron, there is a large amount of scattering and energy loss associated with the transport. The energy losses can be collisional, imparting energy to 'free' electrons in the medium, and radiative, creating bremsstrahlung photons. This chapter will not cover the topic of electron transport in great detail, but will give some of the fundamental aspects governing the scattering and energy deposition. The calculation algorithms used by the Alberta Treatment Planning system (Battista *et al* 1984) to calculate dose deposition due to electron beams, will be described along with the underlying approximations in the transport theory and the implementation. This will be used as a base for the following chapters, where the algorithms will be tested experimentally.

A. Scattering Power

The most important interaction mechanism for electrons is with the electromagnetic field of the material through which the electron is travelling. Multiple Coulomb scattering refers to the scattering of electrons due to the electromagnetic field of the nucleus. Because of the mass of the nucleus, this is mostly an elastic process. If we let $\xi(\Theta)d\Omega dx$ be the probability that an electron scatters into the solid angle $d\Omega$ at angle Θ, when traversing a thickness of material dx (g/cm^2), then (Mott 1929)

$$\xi(\Theta)d\Omega dx = \frac{N}{A}\left(\frac{Zr_e\mu_e}{2p\beta}\right)^2\left(1 - \beta^2\sin^2(\Theta/2)\right)\frac{d\Omega dx}{\sin^4(\Theta/2)} \qquad \text{(II.1)}$$

where N is Avogadro's number, Z is the atomic weight and A is the atomic number of the material. The relativistic momentum and velocity of the electron are p and β, and r_e and μ_e are the classical electron radius and mass of the electron, respectively. The finite size of the nucleus restricts scattering events to angles smaller than some angle Θ_{max}. Screening effects due to the atomic electrons also restrict scattering events to angles larger than Θ_{min}. Recommended values of these angles are (ICRU 1984a)

$$\Theta_{min} = 1.13\,\frac{\alpha Z^{1/3}}{\beta(\tau+1)} \qquad \text{(II.2)}$$

$$\Theta_{max} = \frac{2A^{-1/3}}{\alpha\beta(\tau+1)} \qquad \text{(II.3)}$$

where α is the fine structure constant ($1/137$) and τ is the ratio of the kinetic energy of the electron to its rest mass.

Because of the long range of the electromagnetic interaction, the electron has a high probability of undergoing a deflection in the thickness dx. This implies that the nuclear scattering is a statistical process. Therefore the change in mean square scattering angle is a meaningful quantity, and is given by (Rossi and Greissen 1941)

$$\left(T/\rho\right) = \frac{d(\overline{\Theta^2})}{dx} = \int_{\Theta_{min}}^{\Theta_{max}} \xi(\Theta)\, 2\pi\Theta d\Theta \qquad \text{(II.4)}$$

where $\left(T/\rho\right)$ is the mass scattering power. Evaluating equation (II.4) gives (ICRU 1984a)

$$\frac{T}{\rho} = \frac{\pi N}{A}\left(\frac{2r_e Z}{(\tau+1)\beta^2}\right)^2 \left\{ \ln\left[1 + \left(\frac{\Theta_{max}}{\Theta_{min}}\right)^2\right] - 1 + \left[1 + \left(\frac{\Theta_{max}}{\Theta_{min}}\right)^2\right]^{-1} \right\} \qquad \text{(II.5)}$$

as the mass scattering power of the element. For compounds and mixtures, the scattering power is a weighted average (percentage mass) of the scattering powers of the elements. Equation (II.5) only considers the scattering of the electrons from the nucleus. The accepted method of accounting for additional electron-electron scattering is to increase the scattering power by replacing Z^2 by $Z(Z+1)$ in equation (II.5).

B. Stopping Power

Unlike scattering from the nucleus, electron-electron scattering is not an elastic process for the incident electron, because the masses of the scatterer and target are equal. Because the incident and target particles are not distinguishable, the energy transferred in an electron-electron collision is less than half the incident energy. Most of the time, the energy transferred is very small and leads to atomic excitation. Occasionally, the incident electron

will transfer enough energy to ionize the atom, and the electron with the lower energy after the collision, is a delta ray.

As with multiple Coulomb scattering, the distance between interactions is small, leading to continuous energy loss of the electron on a macroscopic scale. The energy loss is characterized by the collisional mass stopping power, $(S/\rho)_{col}$, which is the energy lost by the incident electron per unit length of material traversed. For therapeutic energies (1-30 MeV) and tissue-like atomic numbers ($Z \approx 6$), the collisional mass stopping power is relatively constant at ≈ 2 MeV cm^2 g^{-1}.

The electron can also lose energy to bremsstrahlung radiation in the electromagnetic field of the nucleus, and is characterized by the radiative mass stopping power, $(S/\rho)_{rad}$. The probability of bremsstrahlung radiation increases with the atomic number, Z, of the material traversed and the energy of the electron. For therapeutic energies and tissue-like atomic numbers, the radiative stopping power is small compared to the collisional stopping power.

C. Dose Calculation

1. General equation

The ultimate goal of treatment planning is to calculate the dose deposited in the patient. For all types of ionizing radiation, the final dose deposition is due to electrons, either directly from the radiation beam, or set in motion by the radiation beam. If we define the fluence $\Phi(E,\Omega,\boldsymbol{r})dEd\Omega$ as the number of electrons at point $\boldsymbol{r}$ with energy in the interval dE around E which cross a unit area with normal Ω, within $d\Omega$ of Ω, then it can be shown that the dose at point $\boldsymbol{r}$ is given by (ICRU 1984a)

$$D(\boldsymbol{r}) = -\int_{4\pi}\int_{0}^{\infty}\left\{\frac{dE}{ds}\,\Phi(E,\Omega,\boldsymbol{r}) + E\,\frac{d\Phi(E,\Omega,\boldsymbol{r})}{ds}\right\}dEd\Omega \qquad \text{(II.6)}$$

where s is the mass traversed per unit surface area along the direction Ω. The first term is

simply the collisional loss of the electrons as they cross the small volume around $\boldsymbol{r}$, while the second term is the energy deposited by electrons stopping in the volume.

To solve equation (II.6), we need to obtain $\Phi(E,\Omega,\boldsymbol{r})$ by solving a transport equation, which is very difficult for the general case. It is a coupled equation even for pure electron beams, because primary electrons produce bremsstrahlung photons, which in turn can set more electrons in motion. The Monte Carlo method is a practical method for obtaining accurate solutions to equation (II.6) for simple geometries.

2. Monte Carlo methods

The difficulty of solving equation (II.6) analytically, for 'realistic' geometries, has led to Monte Carlo computer simulations of the radiation transport. The Monte Carlo method tries to reproduce the fluence, $\Phi(E,\Omega,\boldsymbol{r})$, by repeated simulations of the transport of single particles. By transporting enough particles, the calculated fluence should approach the actual fluence. The amount of computing time necessary to do the simulation depends on many factors such as transport geometry, energy of the particles, and the resolution required. At the present time, the Monte Carlo method is the most accurate general method of calculating dose and fluence distributions in radiotherapy beams, but computing time for realistic geometries is prohibitive for any sort of routine use. It is however, a useful tool for understanding aspects of radiation transport and calculating dose or fluence in cases where measurements would be impractical or impossible. The EGS4† code system (Nelson *et al* 1985) is described below, although the general principles hold for many other Monte Carlo codes.

The general principle of Monte Carlo simulations is quite simple. The user starts by defining the geometry of the phantom materials, including scattering properties, particle

---

† Electron Gamma Shower, version 4.

creation probabilities, and so on. This step also includes describing the quantities of interest (eg. fluence, dose) and the regions where these quantities should be 'scored'. The next step is to create a particle to transport through the specified geometry. The initial conditions of the particle (position and velocity) may be randomly chosen from a distribution to more accurately simulate a 'real' beam. This particle is then transported through the phantom geometry and if the particle passes through a region of interest, we accumulate (or score) the data. Any particles created by the original incident particle are transported through the geometry as well. The 'history' is complete when the primary particle and all of its progeny complete their transport, by leaving the phantom geometry or falling below a user-defined cutoff energy. A complete simulation usually consists of several hundred thousand or several million histories, and can take several hours or days of computing time. Provided that the Monte Carlo code is performing properly, the Monte Carlo solution will approach the 'true' solution with the variance of the difference between the two solutions approaching zero as $1/n$, where n is the number of incident electrons in the simulation. To reduce the uncertainty of the Monte Carlo solution by a factor of two, four times as many histories are needed, since the uncertainty of the Monte Carlo results is proportional to the square root of the variance. To provide an estimate of the standard error of the Monte Carlo results, a Monte Carlo run is divided into 'batches', and the results of the batches are compared using standard statistical techniques.

The EGS4 code system is a Monte Carlo code originally intended for use in very high energy electromagnetic cascades of electrons and photons. The code has been extended for use in the therapeutic energy range and is now used extensively by medical physicists. The user must supply two subroutines, one to describe the geometry of the simulation, and another to accumulate the calculated data. The basic method for transporting photons and electrons in the code is different. High energy photons do not interact very much with the electromagnetic field of the material traversed, which gives

them a macroscopic mean free path. It is therefore computationally practical to simulate every single interaction for photons. However, the distance between interactions for electrons is on a microscopic scale, so it is not computationally feasible to simulate every interaction discretely. The electrons are transported in macroscopic steps, and multiple scattering theory is used to calculate the resultant electron parameters. The quality of the results depends on the choice of electron transport parameters, particularly step size. In order to remove this dependence, the PRESTA‡ algorithm (Bielajew and Rogers 1986) was developed and incorporated as an option within the EGS4 code system. The PRESTA algorithm has been shown to be independent of step size.

D. Fermi-Eyges Theory

In principle, solving the Boltzmann equation for electron transport is not difficult, but adapting the problem to clinical electron beams causes several problems. Even for monoenergetic, monodirectional beams, the computing time needed is unrealistic from a clinical perspective. For routine treatment planning, beam calculation times of more than a few minutes are unrealistic. Even though computing speed is quickly increasing with advances in computer hardware, full calculations typically take many hours or days of CPU time. As a compromise between accuracy of results and computing time, most modern electron beam calculation algorithms use an approximation to the Boltzmann transport equation known as Fermi-Eyges theory.

Fermi-Eyges theory describes the probability distribution for an electron entering a semi-infinite medium. For simplicity, we will start the electron at $x,y,z=0$, with an initial direction along the positive z axis. We will also assume that the medium is homogeneous. At a depth z, the electron is described by its spatial coordinates (x,y), and its direction

---

‡ Parameter Reduced Electron-Step Transport Algorithm.

projected onto orthogonal planes (θ_x,θ_y). The probability of an electron having coordinates (x,y,θ_x,θ_y) is given by $f(z,x,y,\theta_x,\theta_y)dxdyd\theta_x d\theta_y$.

Since we have azimuthal symmetry about the z axis, the x and y scattering probabilities are independent. This implies that

$$f(z,x,y,\theta_x,\theta_y) = f(z,x,\theta_x) \times f(z,y,\theta_y) \quad , \tag{II.7}$$

where the probability distributions on the right hand side of equation (II.7) are identical except for the x and y variables. Therefore, obtaining a solution for $f(z,x,\theta_x)$ gives the complete probability distribution through equation (II.7).

1. Fermi's derivation[†]

If we let $\rho(\theta_x)d\theta_x dz$ be the probability that a particle traversing a thickness of material dz scatters into an angle $d\theta_x$, then

$$\rho(\theta_x) = \rho(-\theta_x) \quad , \tag{II.8}$$

$$\int_{-\infty}^{\infty} \rho(\theta_x)d\theta_x = 1 \quad , \tag{II.9}$$

$$\int_{-\infty}^{\infty} \theta_x \rho(\theta_x)d\theta_x = 0 \quad , \tag{II.10}$$

and

$$\int_{-\infty}^{\infty} \theta_x^2 \rho(\theta_x)d\theta_x = d\overline{\theta_x^2} = \frac{d\overline{\theta_x^2}}{dz}dz \tag{II.11}$$

define the constraints on $\rho(\theta_x)$. Equations (II.9) through (II.11) assume that the scattering angles are small, and $\rho(\theta_x)$ is sharply peaked about θ_x=0. Therefore, we can extend the integrals from $-\infty$ to $+\infty$, rather than from $-\pi$ to $+\pi$.

A differential equation for the distribution function can be formulated by considering the change in the distribution function from the coordinate z to $z+\Delta z$. The

---

[†] Rossi and Greissen 1941, page 265.

lateral (x) distribution changes because of existing angular deviations at depth z, and because of scatter in the layer Δz. The scatter is generally a much smaller effect and can be ignored. Therefore,

$$f(z+\Delta z,x,\theta_x)_x = f(z,x-\theta_x\Delta z,\theta_x) = f(z,x,\theta_x) - \theta_x\Delta z\left(\frac{\partial f}{\partial x}\right) \tag{II.12}$$

describes the change in the x distribution. We can then use $\rho(\theta_x)$ as a Green's function to describe the change in the θ_x distribution. This implies that

$$f(z+\Delta z,x,\theta_x)_{\theta_x} = \int_{-\infty}^{\infty} f(z,x,\theta_x')\ \rho(\theta_x-\theta_x')\ d\theta_x' \tag{II.13}$$

and since $\rho(\theta_x-\theta_x')$ is sharply peaked about $\theta_x=\theta_x'$, we expand the integral into a Taylor series in $(\theta_x-\theta_x')$. Keeping the first non-constant term,

$$f(z+\Delta z,x,\theta_x)_{\theta_x} = f(z,x,\theta_x) + \frac{1}{2}\frac{\partial^2 f}{\partial\theta_x^2}\left(\frac{d\overline{\theta_x^2}}{dz}\right)dz \tag{II.14}$$

which implies that the full differential equation for the distribution function is given by

$$\frac{\partial f}{\partial z} = -\frac{\partial f}{\partial x} + \frac{1}{\omega^2}\frac{\partial^2 f}{\partial\theta_x^2} \tag{II.15}$$

where

$$\frac{1}{\omega^2} = \frac{1}{2}\frac{d\overline{\theta_x^2}}{dz} \tag{II.16}$$

is proportional to the linear angular scattering power of the medium traversed by the electron. As long as the electron does not lose very much momentum, ω^2 is a constant for a given medium. The solution of equation (II.15) is

$$f(z,x,\theta_x) = \frac{\sqrt{3}\omega^2}{2\pi z^2}\exp\left[-\omega^2\left(\frac{\theta_x^2}{z} - \frac{3x\theta_x}{z^2} + \frac{3x^2}{z^3}\right)\right], \tag{II.17}$$

which can be verified by substitution. The marginal distributions of $f(z,x,\theta_x)$ are Gaussian,

$$f(z,\theta_x) = \int f(z,x,\theta_x)\ dx = \frac{\omega}{2\sqrt{\pi z}}\exp\left[\frac{-\omega^2\theta_x^2}{4z}\right], \tag{II.18}$$

$$f(z,x) = \int f(z,x,\theta_x)\, d\theta_x = \frac{\sqrt{3}\omega}{2\sqrt{\pi z^3}} \exp\left[\frac{-3\omega^2 x^2}{4z^3}\right] , \qquad \text{(II.19)}$$

which is why Fermi-Eyges theory is often referred to as the Gaussian approximation‡. As z approaches zero, the Gaussian marginal distributions approach Dirac δ functions as required by our initial conditions. Equations (II.18) and (II.19) also imply that the mean square lateral displacement is proportional to the mean square angular deviation,

$$\overline{x^2} = \frac{2z^3}{3\omega^2} = \frac{1}{3} z^2 \left(\frac{2z}{\omega^2}\right) = \frac{1}{3} z^2 \overline{\theta_x^2} \qquad \text{(II.20)}$$

which implies that we only need to calculate the mean square angular deviation of the electron distribution to find the spatial distribution at a depth z.

2. *Eyges' extension to Fermi scattering*

Eyges (1948) extended Fermi's theory by assuming that ω^2 in equation (II.15) is not constant, but a function of z. This is the 'slab' approximation. Another assumption implicit in Fermi-Eyges theory, is that momentum of the electrons is constant for a given depth. To first order, this is true. However, electrons near the edges of the spatial distribution will, on average, have travelled a larger distance through the medium and therefore lost more energy. If we assume that ω^2 is a slowly varying function of electron momentum, then equation (II.15) should still be valid if ω^2 is a function of z.

If we Fourier transform equation (II.15) with respect to x and θ_x, we get

$$\frac{\partial g}{\partial z} = \alpha \frac{\partial g}{\partial \zeta} - \frac{\zeta^2}{\omega^2(z)} g \qquad \text{(II.21)}$$

where

$$g(z,\alpha,\zeta) = \frac{1}{2\pi} \int dx \int d\theta_x\, f(z,x,\theta_x) \exp\left[-i\,(\alpha x + \zeta\theta_x)\right] . \qquad \text{(II.22)}$$

If we change variables to

$$\xi = z + \zeta/\alpha , \qquad z' = z \qquad \text{(II.23)}$$

---

‡ The Gaussian distributions can also be derived using the central limit theorem, as a natural result of *many, small* deflections.

then

$$\frac{\partial g}{\partial z'} = -\frac{\alpha^2(\xi - z')^2}{\omega^2(z')}\, g \tag{II.24}$$

which implies that

$$g(z,\alpha,\zeta) = h(\xi)\, \exp\left[-\alpha^2 \int_k^{z'} \frac{(\xi-\eta)^2}{\omega^2(\eta)}\, d\eta \right] \tag{II.25}$$

where $h(\xi)$ is a constant of integration and k must be determined by the boundary condition,

$$f(0,x,\theta_x) = \delta(x)\ \delta(\theta_x) \tag{II.26}$$

which transforms to

$$g(0,\alpha,\zeta) = \frac{1}{2\pi}\ . \tag{II.27}$$

The boundary condition in equation (II.27) is satisfied by

$$k = 0\ , \qquad \text{and } h(\xi) = \frac{1}{2\pi} \tag{II.28}$$

which can be verified by substituting into equation (II.25). If we define functions A_0, A_1, and A_2 such that

$$A_0(z) = \int_0^z \frac{d\eta}{\omega^2(\eta)} \tag{II.29}$$

$$A_1(z) = \int_0^z \frac{(z-\eta)}{\omega^2(\eta)}\, d\eta \tag{II.30}$$

$$A_2(z) = \int_0^z \frac{(z-\eta)^2}{\omega^2(\eta)}\, d\eta \tag{II.31}$$

then

$$g(z,\alpha,\zeta) = \frac{1}{2\pi} \exp\left[-(A_0\zeta^2 + 2A_1\zeta\alpha + A_2\alpha^2) \right]\ . \tag{II.32}$$

The functions A_0, A_1, and A_2 are the zero, first and second order scattering moments.

To solve for the distribution function in real space, we reverse the Fourier transform to obtain

$$f(z,x,\theta_x) = \frac{1}{2\pi\sqrt{B(z)}} \exp\left(-\frac{\theta_x^2 A_2 - 2x\theta_x A_1 + x^2 A_0}{4A_0 B(z)}\right) \qquad \text{(II.33)}$$

where

$$B(z) = A_0 A_2 - A_1^2 \ . \qquad \text{(II.34)}$$

If ω^2 is constant, then equation (II.33) reduces to equation (II.17). We can also obtain the marginal distributions,

$$f(z,\theta_x) = \int f(z,x,\theta_x)\, dx = \frac{1}{2\sqrt{\pi A_0}} \exp\left[\frac{-\theta_x^2}{4A_0}\right] \ , \qquad \text{(II.35)}$$

$$f(z,x) = \int f(z,x,\theta_x)\, d\theta_x = \frac{1}{2\sqrt{\pi A_2}} \exp\left[\frac{-x^2}{4A_2}\right] \qquad \text{(II.36)}$$

where the scattering moments are usually integrated numerically.

The above equations form the basis for most current pencil beam algorithms. The main restriction is the slab approximation, and the implications of this are discussed in a later section. Recent developments have given solutions to the electron transport equation that are accurate to second order in angle (Jette and Bielajew 1989) and have relaxed the slab approximation by reformulating equation (II.15) in three dimensions and allowing ω^2 to be an arbitrary function of x, y, and z (Jette 1991), but they have yet to be adapted for clinical use.

E. MDAH Algorithm

1. Stationary electron beams

Fermi-Eyges theory has been a useful approximation for electron transport in radiotherapy. An electron dose calculation algorithm developed at M.D. Anderson Hospital (Hogstrom *et al* 1981) is implemented in the Alberta Treatment Planning system (Battista *et al* 1984). It is a pencil beam algorithm that uses X-ray computed tomography (CT) information to account for heterogeneities in the path of the beam. The correlation between

the CT information and electron scattering and stopping powers is incorporated into the algorithm (Hogstrom *et al* 1984). This algorithm, implemented in 2D, is also available in a commercial treatment planning system (Hogstrom *et al* 1984).

We can start by writing down the spatial probability distribution for an electron incident at the origin, with a direction along the z axis as

$$f(x,y,z) = \frac{1}{2\pi\sigma_{MCS}^2} \exp\left(-\frac{x^2+y^2}{2\sigma_{MCS}^2}\right) \tag{II.37}$$

where σ_{MCS}^2 is the variance of the pencil beam fluence due to multiple Coulomb scattering. Comparing with equation (II.36), we see that

$$\sigma_{MCS}^2 = 2A_2 = 2\int_0^z \frac{(z-\eta)^2}{\omega^2(\eta)}\,d\eta = \frac{1}{2}\int_0^z (z-\eta)^2\,T(\eta)\,d\eta \tag{II.38}$$

where $T(\eta) = \omega^{-2}(\eta)$ is the linear scattering power at depth η.

Equation (II.37) also describes the planar fluence for a 'pencil' beam incident at the origin. To calculate the planar fluence for a broad beam, we need to integrate the pencil beam fluence over the extent of the broad beam. This gives

$$\Phi^p(x,y,z) = \int_{-B}^{B} dy' \int_{-A}^{A} dx'\, S(x',y')\, f(x-x',y-y',z) \tag{II.39}$$

where $\Phi^p(x,y,z)$ is the number of particles crossing the x-y plane at coordinates (x,y,z). $S(x',y')$ is the incident planar fluence at (x',y') and the field has half-widths A and B in the x and y directions respectively. If we assume that the source has a constant unit strength, $S(x',y') = 1$, then we can integrate equation (II.39) using error functions† giving

$$\Phi^p(x,y,z) = \frac{1}{4}\left[\mathrm{erf}\left(\frac{A-x}{\sqrt{2}\,\sigma_{MCS}}\right) + \mathrm{erf}\left(\frac{A+x}{\sqrt{2}\,\sigma_{MCS}}\right)\right] \times \left[\mathrm{erf}\left(\frac{B-y}{\sqrt{2}\,\sigma_{MCS}}\right) + \mathrm{erf}\left(\frac{B+y}{\sqrt{2}\,\sigma_{MCS}}\right)\right] \tag{II.40}$$

---

† $\mathrm{erf}(x) = \frac{2}{\sqrt{\pi}}\int_0^x e^{-u^2}\,du$

for the planar fluence at any point. Of course, this assumes that σ_{MCS} only varies with depth (i.e., the phantom has slab geometry). If the incident planar fluence is not constant, then equation (II.39) can be integrated numerically by summing equation (II.40) over small intervals.

Equation (II.40) is valid as long as the electrons are initially directed along the z axis. In practice, the broad beam incident on a patient has been scattered by the air gap between the electron source (e.g., scattering foil) and the patient. This implies that the electrons at any point on the surface of the patient are not monodirectional but have some distribution in angle. Fermi-Eyges theory predicts that this distribution is Gaussian, and can be characterized by some parameter σ_θ which is the standard deviation of the angular distribution of the electrons with respect to the source. This changes the boundary condition for the pencil beam to have a Gaussian distribution of angles at z=0, instead of a δ function. It can be shown that the resulting distribution as a function of depth is still Gaussian with a variance given by

$$\sigma_{med}^2 = \sigma_{air}^2 + \sigma_{MCS}^2 \qquad \text{(II.41)}$$

where

$$\sigma_{air} = z \times \sigma_\theta \ . \qquad \text{(II.42)}$$

The clinical beam is also diverging from the source, so the MDAH algorithm corrects the fluence and width of the 'pencil beam' using a simple geometric divergence term. At this point, an empirical multiple Coulomb scattering factor, *FMCS*, is introduced, which increases the pencil beam variance due to multiple scattering (Hogstrom 1987). Equation (II.41) is modified such that

$$\sigma_{med}^2 = \sigma_{air}^2 + FMCS \times \sigma_{MCS}^2 \qquad \text{(II.43)}$$

is the total pencil beam variance. The *FMCS* parameter is needed because low energy contamination in 'clinical' beams and large angle scattering (which is not modeled) lead to larger measured pencil beam widths than calculated using equation (II.38).

To calculate dose, we need to multiply the total fluence by the mean collisional mass stopping power. To convert from the planar fluence in equation (II.37) to total fluence, we can multiply by the inverse of the average cosine of the polar angle with respect to the z axis, which gives the approximate expression

$$d(x,y,z) = f(x,y,z) \times \left(\overline{\cos \Theta} \right)^{-1} \times \left(\overline{S/\rho} \right)_{col} \qquad \text{(II.44)}$$

where $d(x,y,z)$ is the dose deposited by the pencil beam. If we use the pencil beam fluence as given by equation (II.37), then equation (II.44) ignores delta ray production, bremsstrahlung losses, and energy and range straggling. Rather than explicitly taking other processes into account, the MDAH algorithm calculates the electron pencil beam dose deposition using

$$d(x,y,z) = f(x,y,z) \times g(z) \qquad \text{(II.45)}$$

where

$$g(z) = \frac{D_{ref}(0,0,z)}{\int\limits_{ref} f(-x,-y,z)dxdy} \qquad \text{(II.46)}$$

is the fluence to dose conversion factor. The numerator of equation (II.46) is a measured central axis depth dose for a reference field in a water phantom, the denominator is the integral of the pencil beam fluence over the extent of the reference field. Solving eqaution (II.46) gives the fluence to dose conversion factor as

$$g(z) = \frac{D_{ref}(0,0,z)}{\text{erf}\left(\frac{A}{\sqrt{2}\,\sigma_{MCS}}\right) \times \text{erf}\left(\frac{B}{\sqrt{2}\,\sigma_{MCS}}\right)} \qquad \text{(II.47)}$$

for a rectangular field of dimension $2A \times 2B$. It is easy to show that $g(z)$ is the depth dose for an infinite field size for the same quality beam as the reference beam. The total dose distribution is given by

$$D(x,y,z) = \int\limits_{-B}^{B} dy' \int\limits_{-A}^{A} dx'\, S(x',y')\, d(x-x',y-y',z) \quad , \qquad \text{(II.48)}$$

where the integral is over the applied electron field. Since $g(z)$ is derived from data measured in water, equation (II.48) calculates the dose to a small volume of water at the

same point in the material. If we want the actual dose to the material, then we have to multiply by the ratio of mass stopping power of the material to the mass stopping power of water.

As mentioned above, equation (II.39) could be solved for non-uniform source strength by dividing the broad beam into smaller 'pencil' beams where the source strength would be approximately constant, and then summed to give the final fluence distribution. The same approach is used to solve equation (II.48) in cases where the phantom is not homogeneous. Since Fermi-Eyges theory is only valid where the scattering properties are a function of depth in the medium (slab approximation), the MDAH algorithm calculates the fluence distribution assuming that the pencil beam is transported in a slab geometry defined by the composition of the phantom along the pencil's central axis. The 'central axis approximation' implies that each pencil 'sees' only what is along its central axis.

When applying the MDAH algorithm to heterogeneous phantoms, some modifications must be made to some of the parameters. The fluence to dose conversion factor for the pencil beam is now given by

$$g_{med}(z) = g_{H_2O}(z_{eff}) \tag{II.49}$$

where

$$z_{eff}(z) = \int_0^z \frac{(S_{col})_{med}}{(S_{col})_{H_2O}} \, dz' \tag{II.50}$$

defines an effective depth for the pencil beam. Assuming a linear relationship between energy and effective depth (Harder 1965), the mean energy at depth z is approximately

$$\overline{E_z} = \overline{E_0}\left(1 - \frac{z_{eff}}{R_p}\right) \tag{II.51}$$

where E_0 is the energy at the surface and R_p is the practical range of the broad beam determined from a measured depth dose curve. The mean energy at depth is needed to evaluate equation (II.38).

As presented, the MDAH algorithm does not explicitly deal with bremsstrahlung losses and delta ray production. It can be argued that the fluence to dose conversion factor, $g(z)$, includes the effects of delta ray production, since it converts the 'primary' fluence into the total dose deposition due to electrons. Bremsstrahlung production is a minor component at clinically relevant energies and atomic numbers, so the MDAH algorithm assumes that the electron beam has a constant photon background (geometrically diverging from the source), obtained from the bremsstrahlung tail of the reference central axis depth dose. When calculating the fluence to dose conversion factor, the constant bremsstrahlung background is subtracted from the central axis depth dose, so that $D_{ref}(0,0,z)$ includes only the electron component of the reference beam dose deposition. Of course, there are geometric divergence corrections in all of the above equations since the beam originates at the scattering foil of the accelerator. We will not present the corrected formulae since they would not enhance the understanding of the MDAH electron calculation algorithms.

Because of computing time constraints, a 2D version of the above algorithm was first implemented (Hogstrom *et al* 1984). The 2D implementation needs only a single CT slice, and assumes that the patient geometry is invariant, in and out of the plane of the CT slice. This allows us to do the y integration in equation (II.39) explicitly, decomposing the broad beam into 'strip beams'. The 2D implementation of the MDAH algorithm cannot see heterogeneities outside the CT slice used by the calculation. A 3D version of the code has been implemented (Mah *et al* 1989, Starkschall *et al* 1991), and is now practical for routine use in a clinical setting. As will be seen below, the 3D algorithm shows better agreement with measurement in some cases.

2. *Arced electron beams*

The MDAH algorithm for electron beam dose calculation has also been applied to the calculation of dose deposition resulting from arced electron beams. In an arc electron treatment, the patient is usually positioned at the isocenter of the treatment unit. The gantry

of the treatment unit is rotated while the electron beam is on. This allows, for example, the treatment of large chest wall lesions, without the complications due to overlapping fields. A simple way to calculate the dose distribution due to an arced beam is to sum the dose contributions of many stationary beams at discrete angles. If, for example, we wanted to calculate the dose distribution for a 90° arc from 0°–90° using 1° intervals, then we would have to calculate the dose distributions for 90 stationary beams and then sum the results. Computing time constraints imply that such an approach is only practical if no heterogeneity corrections are made, allowing for table lookup methods of calculating the dose distributions. However, lung tissue is a major heterogeneity in chest wall treatment and must be accounted for.

In order to allow for heterogeneity corrections, the simplest approach is to use the available pencil beam theories, as applied above. However, calculating a dose distribution at each angle of the arc is inefficient. To speed up the calculation, the MDAH arc electron algorithm (Hogstrom *et al* 1989) divides the arc electron transport into two stages. In the first stage, for each gantry position, the resultant electron fluence at the patient surface is calculated and summed into 'pencils' at the patient surface. Each 'pencil' can then be transported in the same fashion as for the stationary beam algorithm described above. At this time, the algorithm has only been implemented in two dimensions, but a 3D implementation for multi-slice treatment planning should be easy to accomplish. The main advantage of the MDAH arc electron algorithm over other algorithms (Leavitt *et al* 1986, Pla *et al* 1988, Pla *et al* 1989) is that patient heterogeneities are taken account of in a manner similar to the stationary beam algorithm which has been tested and works reasonably well (Hogstrom and Almond 1983, Hogstrom *et al* 1984, Cygler *et al* 1987, Mah *et al* 1989). This should give better estimates of the dose to lung tissue, which is a sensitive structure in chest wall treatments.

F. Other Algorithms

The main disadvantage of most dose calculation algorithms based Fermi-Eyges theory is the central axis approximation. The lateral spread of a pencil beam of electrons incident on a water phantom can be much larger than the anatomical resolution as the electrons approach the end of their range. However, the dose distribution for the pencil beam depends only on the material along the central axis of the pencil beam. This means that a pencil can 'miss' a heterogeneity when, in fact, the lateral spread at depth is such that some electrons pass through the heterogeneity. This becomes more of a problem at large depths, compared to the practical range.

There are at least three ways to overcome this limitation. One way is to relax Eyges' requirement that the scattering power be a function of depth alone (the slab approximation), and allow the scattering properties to vary in all three dimensions. An analytical solution has been found (Jette 1991), but it remains to be seen whether the solution can be implemented in a practical manner.

Another approach is to use the results of Fermi-Eyges theory, but vary the implementation of the algorithm. This has been done by Shiu and Hogstrom (1987, 1991), but calculation times are still prohibitive for routine use. Their approach has been to transport the pencil beams a small distance in the phantom (≈0.5 cm), and then redistribute the electrons into new pencil beams at depth. This means that the lateral extent of the pencil beam is small at all stages of the calculation, implying that the central axis approximation is still appropriate. Their 'redefinition' algorithm also allows the pencil beams to have a distribution in energy, implying that range straggling can occur naturally. A similar algorithm has been developed by Storchi and Huizenga (1985), but their algorithm does not allow for variations in the energy spectrum of the electrons with depth.

A third approach is the so-called OMEGA† project (Mackie *et al* 1990). This group hopes to accelerate the Monte Carlo (EGS4) calculation of the radiation transport using a combination of networked supercomputers, software optimization, and variance reduction techniques. This project is in its infancy, and it remains to be seen whether or not a practical calculation method results from this research.

---

† Ottawa Madison Electron Gamma Algorithm.

III. Stationary Beams

In the previous chapter, we have seen the theoretical basis for the MDAH electron calculation algorithm and some of the details important in its implementation. Several approximations have been identified in the Fermi-Eyges electron transport theory, and the computer implementation. Experimental data is therefore needed to test the accuracy and limitations of the current algorithm so that we can be aware of situations that will cause inaccurate dose predictions and the approximate magnitude of the inaccuracies. Some comparisons between calculation and measurement have been reported (Hogstrom *et al* 1984, Lax 1989), but the number of geometries tested has been small. Generally, a single configuration has been measured and compared with pencil beam calculations. The following sections will report on a study that systematically tested some of the effects of phantom geometry on the discrepancies between calculation and measurement, for two-dimensional and three-dimensional versions of the MDAH pencil beam calculation code.

A. Wax Phantoms

1. Experimental method

The first measurements in this study (Cygler *et al* 1987) were performed as an initial verification of the MDAH algorithm as implemented in the Alberta Treatment Planning system (Battista *et al* 1984). The electron beam was produced by a medical linear accelerator (Siemens Mevatron XX) which uses the scattering foil method to give a broad beam. A thin phantom, consisting of one or more aluminum (or air) inclusions embedded in wax, was attached to the end of the 10×10 cm^2 electron applicator in a horizontal position, as shown in figure III.1. The detector was a small p-type diode manufactured commercially (Therados) after the design of Rikner and Grusell (Rikner and Grusell 1983, Rikner 1985, Rikner and Grusell 1987). The directional dependence of the diode was determined experimentally at 5 cm depth in water for 18 MeV incident electrons, and is

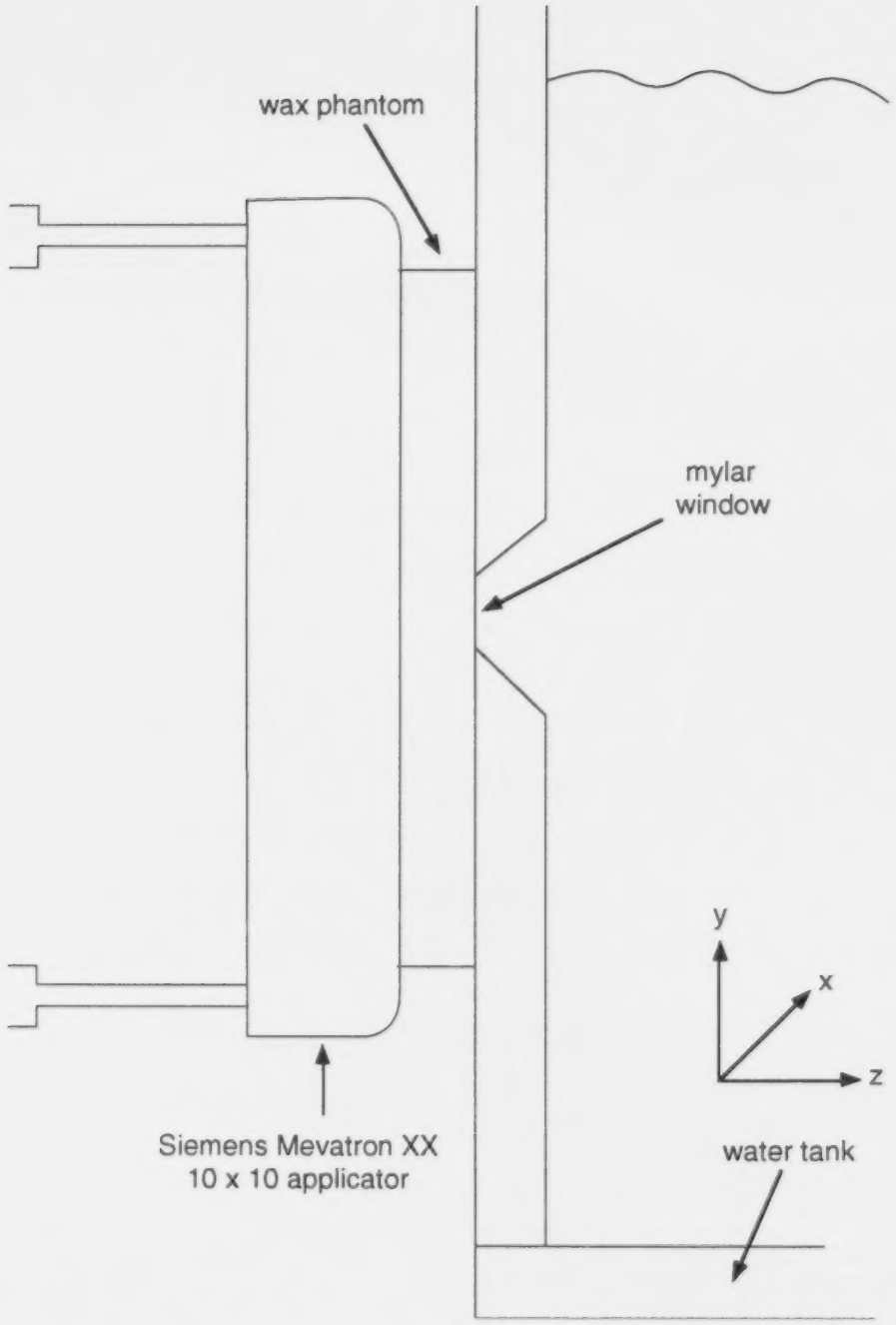

Figure III.1. Schematic diagram of the setup used for measuring dose profiles behind wax phantoms with high and/or low density inclusions.

shown in figure III.2. The response was deemed to be constant enough that corrections for detector angular response (Brahme 1985) would be small compared to other dose uncertainties and could therefore be ignored.

The beam entered the side of a large water tank ($50 \times 50 \times 40$ cm^3) through a thin (0.01 cm) mylar window. The source to surface distance (SSD) was 100 cm The diode was scanned laterally (in the x direction in figure III.1) using a one dimensional scanning dosimetry system (Therados LSC-2), which has a positioning accuracy of 0.05 cm and a reproducibility of 0.02 cm. The LSC-2 scanner also has electrometer circuitry designed for use with two diode dosimeters. An extra diode (reference) was placed in the radiation field outside of the region of interest, and the dose output of the unit was the ratio of the scanning (field) diode's output to the reference output. This allowed us to compensate for temporal fluctuations in the output of the linear accelerator. The position and dose output signals were captured by a digital X-Y recorder (Hewlett Packard HP7090A) and stored in its internal buffers. After the scan was complete, the voltages were manually recorded for further analysis. Repeated measurements showed that day to day stability of the system was better than 1%, which indicated that there was no significant radiation damage to the p-type diode (Rikner and Grusell 1983).

The phantoms were irradiated with electron beams with nominal energies of 10 MeV and 18 MeV. The beam parameters needed for the calculation (Hogstrom *et al* 1984) were measured and input into the treatment planning system. Comparison of measured and calculated isodose lines, shown for 10 MeV in figure III.3, was used to confirm correct entry of the required parameters. The beam energy was obtained from the linear energy-range relationship used by the MDAH algorithm (Markus 1961).

The phantoms were constructed to resemble heterogeneities found in chest wall and neck irradiation, and consisted of air and aluminum embedded in wax, which simplified mounting on the electron applicator. The wax was composed of equal weights paraffin and

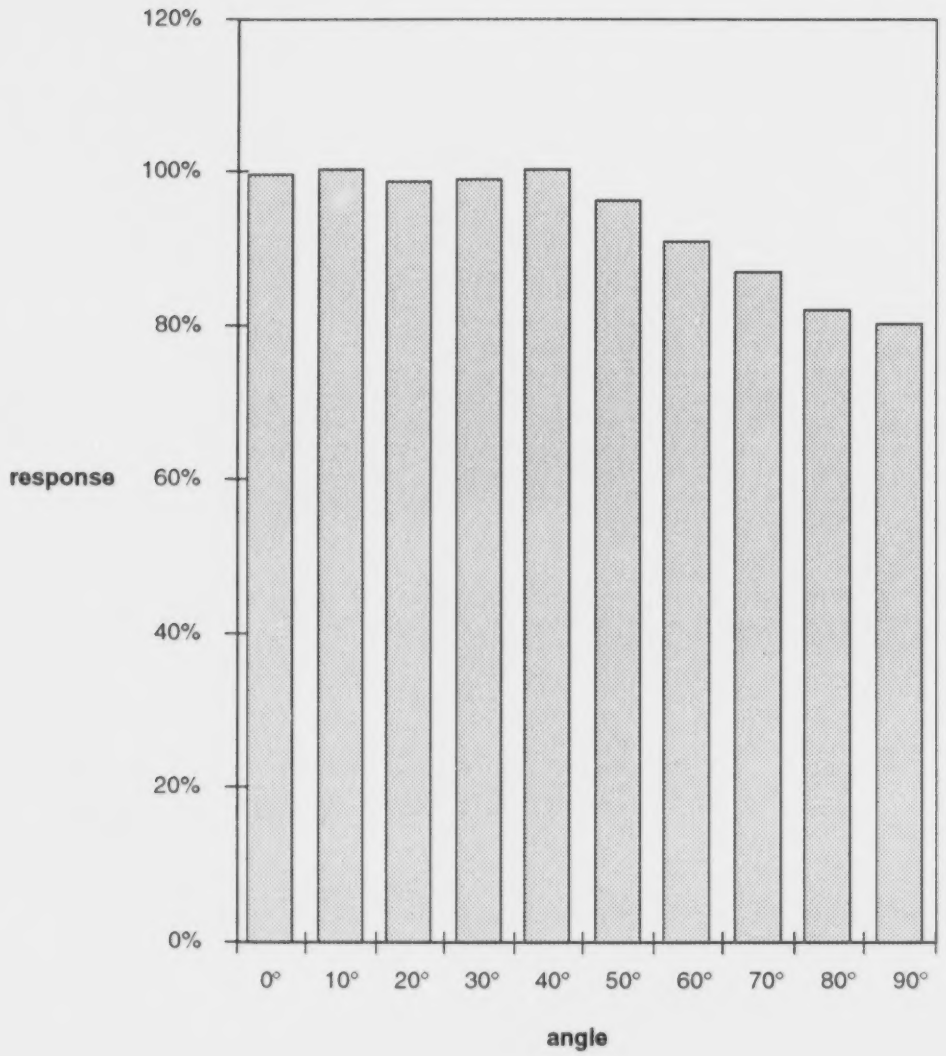

Figure III.2. Diode angular response, normalized to the response at 0°. The response was measured near the depth of maximum dose on the central axis of a 10×10 cm^2 beam of 18 MeV electrons incident on a water phantom.

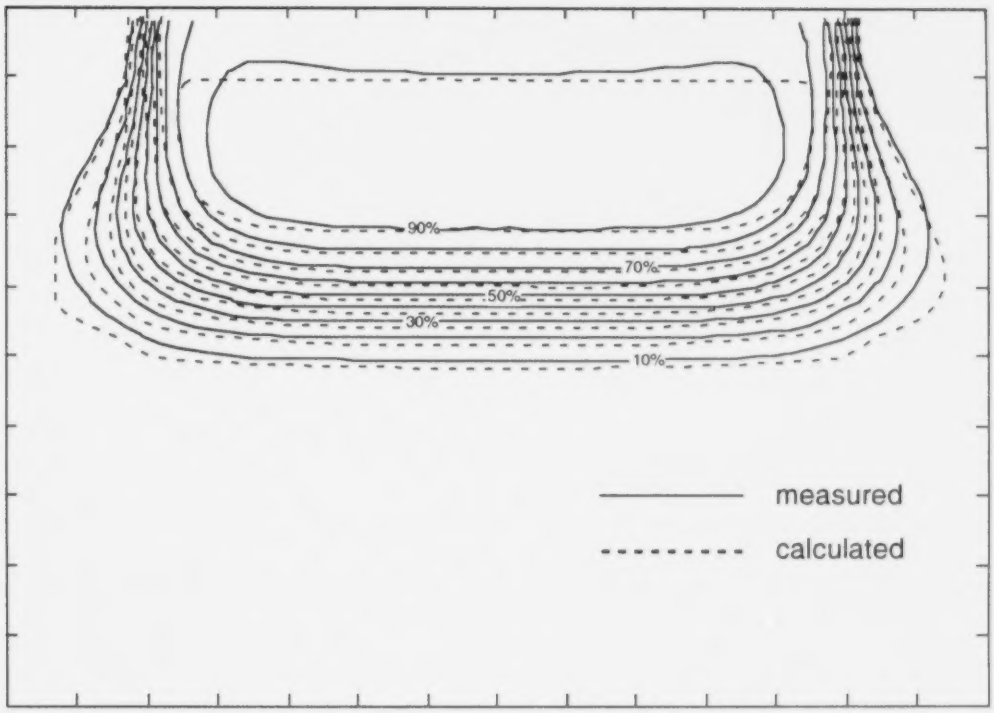

Figure III.3. Comparison of measured and calculated isodoses for a 10×10 cm^2 beam of 10 MeV electrons incident on a water phantom.

beeswax 'doped' with powdered resin. The electron density of the wax was 0.91 (relative to water), and was taken into consideration for the calculations. The aluminum was intentionally chosen to 'stress test' the algorithm (Brahme 1983). The phantom geometries are summarized in table III.1.

For each phantom configuration, four profiles were measured. One profile was measured with the diode at the mylar window, and the second profile at a depth of 1 cm. The sensitive volume of the detector is approximately 0.1 cm from the front of the detector, which gave profile depths of 0.1 and 1.1 cm behind the wax phantom. The profiles were measured for electron energies of both 10 MeV and 18 MeV. To compare with the calculations, the diode signal was normalized to the signal at a depth of maximum dose in the water phantom without the wax phantom present.

The MDAH algorithm also requires measured CT (X-ray Computed Tomography) numbers for the phantom materials to calculate stopping and scattering powers for the medium. These were measured using a commercially available scanner (General Electric 8800), yielding CT numbers of –94 and 2227 Houndsfield units for the wax and aluminum, respectively. The algorithm's stopping and scattering power tables were also

Table III.1. Experimental wax phantoms.

Figure	Phantom
III.4	Single 'long rib'—aluminum rod, 0.96 cm diameter, 10 cm length, embedded in wax, 1.0 cm thick.
III.5	Pair of 'long ribs' as in III.4, with edges separated by 1.0 cm.
III.6	'Short rib' phantom as in III.5, but with 'rib' shortened to 1.0 cm.
III.7	'Vertebral body'—aluminum coin, 2.50 cm diameter, 1.0 cm thick embedded in wax, 1.15 cm thick.
III.8	'Spine'—triplet of aluminum coins as in III.7 with edges separated by 0.50 cm.
III.9	'Trachea and spine'—phantom similar to III.8 except the aluminum coins are embedded in wax, 1.40 cm thick, and overlayed by an air rod, 2.6 cm diameter, 10 cm wide, and an additional thin layer of wax, 0.26 cm thick.

updated to be consistent with more recent data (ICRU 1984a,b), and to allow proper extrapolation for aluminum.

2. *Results and discussion*

The experimental results are presented in figures III.4–III.9. Each figure follows the same format where the left hand side (a) shows results for a 10 MeV beam, while the right hand side (b) shows results for an 18 MeV beam. The top of each side (A) shows the profile at the mylar window of the water tank (or 0.1 cm behind the wax phantom), and the bottom (B) shows the profile at 1.1 cm behind the wax phantom. The data were normalized to maximum dose in a homogeneous water phantom for a 10×10 cm^2 field size. The horizontal dotted line shows the calculated dose taking into account the wax, but without any of the aluminum or air inclusions.

For the purposes of discussion, 'hot spot' refers to a region of local dose maximum, and likewise 'cold spot' refers to a region of local dose minimum. The term 'underpredicted hot spot' means that the calculated 'hot spot' has lower dose than the measured 'hot spot'. The term 'underpredicted cold spot' indicates that the calculated 'cold spot' has a higher dose than (or is not as cold as) the measured 'cold spot'. All dose differences are quoted as the difference in percentage values, and not the percentage difference in local dose.

In figure III.4, we compare the results of measurements and calculations for a single long aluminum 'rib', 10 cm in length. Since the field size is 10×10 cm^2, the rod satisfies the 2D assumption of the original MDAH algorithm, and is similar to a standard geometry (Brahme 1983). The agreement between calculation and measurement is very good. The only region significant disagreement is at the shallower depth for the 10 MeV electron beam. The cold spot in the shadow of the rod is underpredicted by 9%.

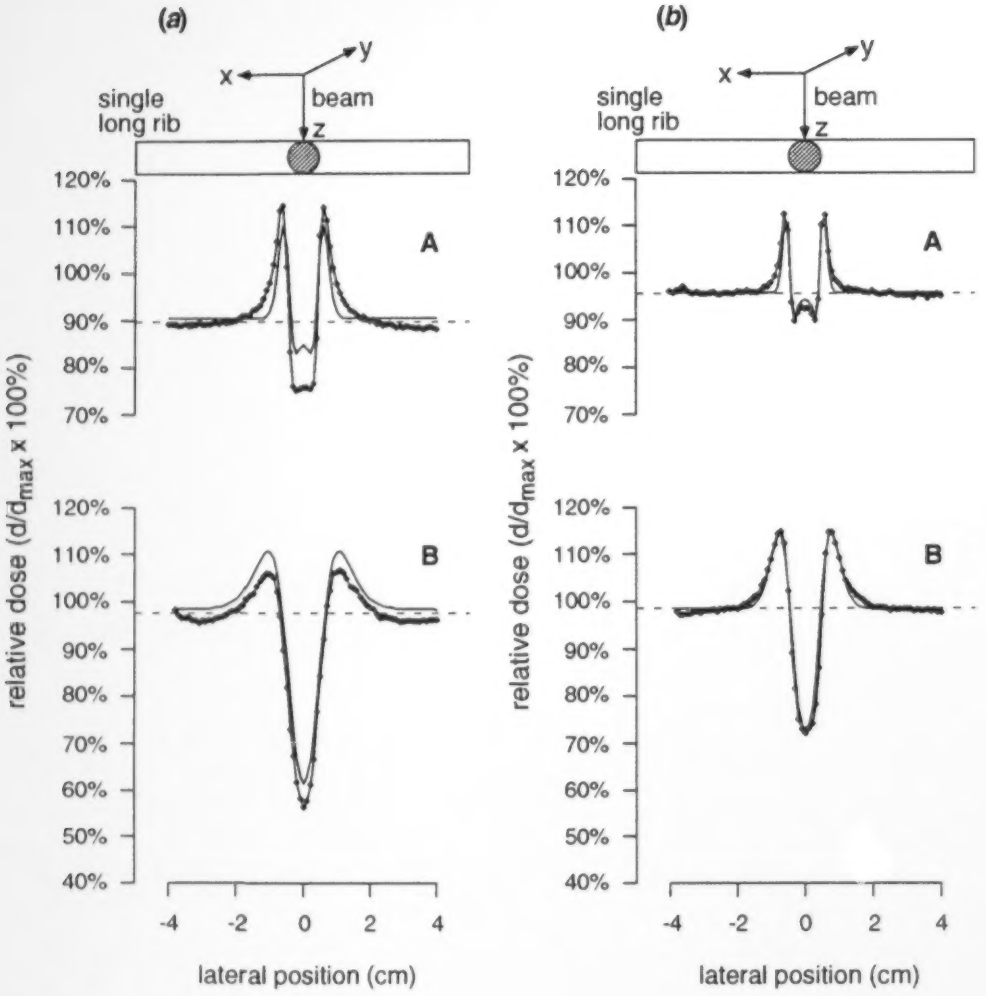

Figure III.4. Lateral dose profiles beyond a single 'long rib' in water irradiated with 10 MeV (a) and 18 MeV (b) electrons. The diamonds are experimental data; the solid line is calculated; the dashed line is the dose in a homogeneous water phantom at the same depth. The profiles were at depths of 0.1 cm (A) and 1.1 cm (B) beyond the phantom, or 1.1 cm and 2.1 cm from the surface.

Figure III.5 shows a similar phantom, but with two rods, separated by 1.0 cm. As expected, the calculated and measured profiles are superpositions of the profiles from figure III.4, and the magnitudes of the hot and cold spots are very similar. For the shallower depth at 10 MeV, the cold spot is underpredicted by 8%. There is also a discrepancy of approximately 9% in the region between the rods. In figure III.4 we see that the hot spots at the edges of the ribs are slightly underpredicted, which implies that after superposition, there will be an even larger discrepancy, which is consistent with the data in figure III.5.

For both figure III.4 and III.5, the agreement between measurement and calculation is better for 18 MeV than for 10 MeV. Qualitatively, this is explained by the small angle approximation of Fermi-Eyges theory. The 10 MeV electrons are more likely to be scattered into large angles, so the fluence distribution is not modeled as accurately as for 18 MeV electrons, which, for the same depth of penetration, undergo less large angle scattering.

Another interesting feature of figure III.5 is the inability of the calculation to mimic the slight dip in the measured dose at x=0. This highlights another shortcoming of Fermi-Eyges theory. The process of Fermi-Eyges electron transport can be compared to applying a filter to the anatomical information. At each depth of the calculation, we take anatomical information along the ray paths emanating from the radiation source, and essentially filter this data. The filter has a smoothing effect over a distance comparable to the width of the pencil beam at that depth. In other words, the width of the pencil beam specifies the resolving power of the calculation algorithm as a function of depth in the phantom. The pencil beam width at a depth of 2 cm is approximately 0.3 cm, as opposed to 0.1 cm at a depth of 1 cm. Since the separation of the dose peaks between the rods in figure III.5 is only 0.6 cm, we cannot expect the calculation to resolve this 'dip' when the pencil beam standard deviation is of the order of 0.3 cm.

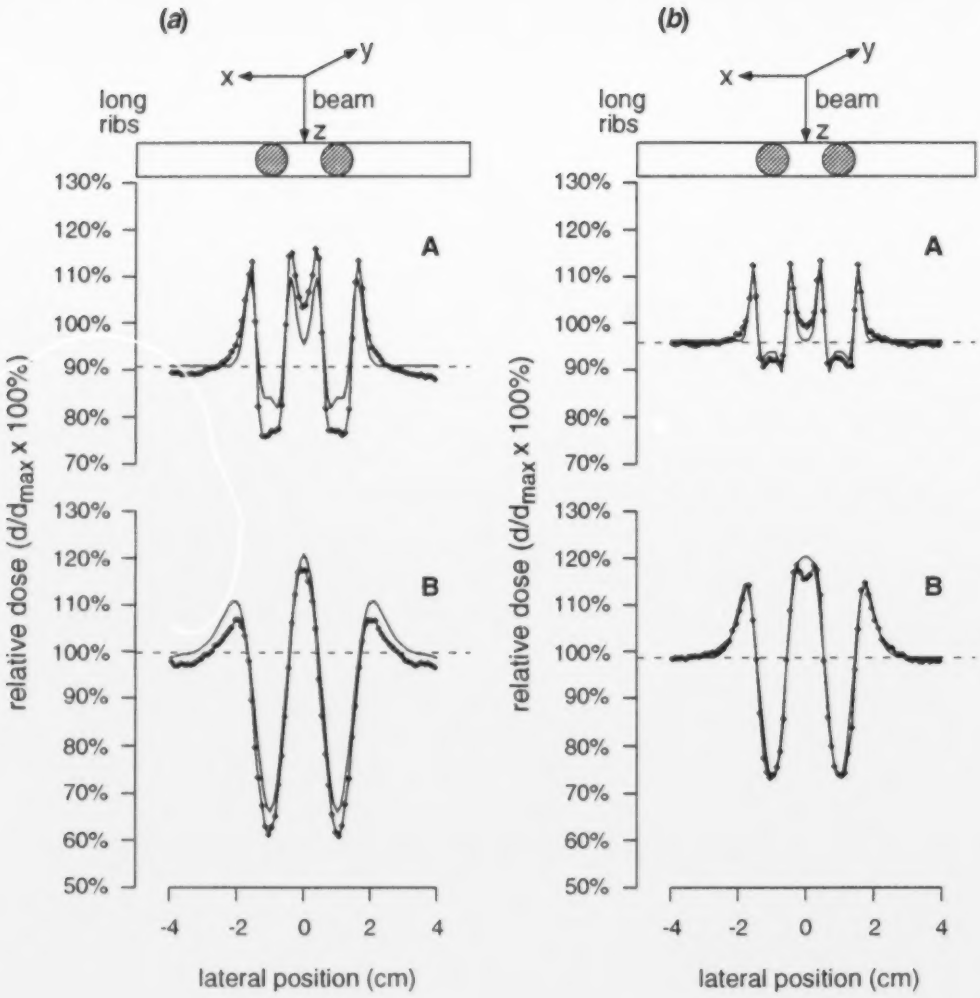

Figure III.5. Lateral dose profiles beyond two 'long ribs' separated by 1 cm and irradiated with 10 MeV (a) and 18 MeV (b) electrons. The diamonds are experimental data; the solid line is calculated; the dashed line is the dose in a homogeneous water phantom at the same depth. The profiles were at depths of 0.1 cm (A) and 1.1 cm (B) beyond the phantom, or 1.1 cm and 2.1 cm from the surface.

Figure III.6 shows the results for the same phantom as figure III.5, except that the rods have been shortened to 1.0 cm in length. This is similar to a standard 3D phantom (Brahme 1983), and was measured to test the magnitude of the effect of the 2D assumption in the original MDAH algorithm. The calculated dose is identical to figure III.5, because the 2D assumption does not 'know' the length of the rod and assumes that it extends across the entire field. The measured dose, however, changes significantly. At shallower depths, the magnitudes of the hot spots are predicted quite accurately. In fact, for 10 MeV, there is actually better agreement than for figure III.5. This is a result of the lack of scatter from the 'missing' ends of the aluminum rods. However, this is just fortuitous. The missing scatter also leads to less measured dose in the shadow of the rods, where the cold spots are underpredicted by 21% and 7% for 10 MeV and 18 MeV respectively.

In contrast with figure III.5, the agreement between measurement and calculation fails to improve with depth, and the measured dose is systematically lower than the measured dose. This is a result of the 2D assumption in the original implementation of the MDAH algorithm, which results in excess scatter from a 10 cm rod rather than a 1 cm rod.

Figure III.7 shows the results for our 'vertebral body', consisting of a single 2.5 cm diameter 'coin' embedded in a wax phantom 1.15 cm thick. The results are qualitatively similar to figure III.6, which was also a 3D phantom. At the shallower depth, the hot spots at the edge of the coin are accurately predicted. However, the dose in the shadow of the coin is overestimated for 10 MeV and predicted accurately for 18 MeV. This means that for 10 MeV, 2.5 cm (the lateral dimension of the coin) is still not large enough to be considered a 2D phantom, at least for the shallower depth. For 18 MeV, the contribution to the dose in the shadow of the coin by electrons originating more than 1.25 cm away is insignificant, and the coin is a 2D heterogeneity at the shallower depth. At

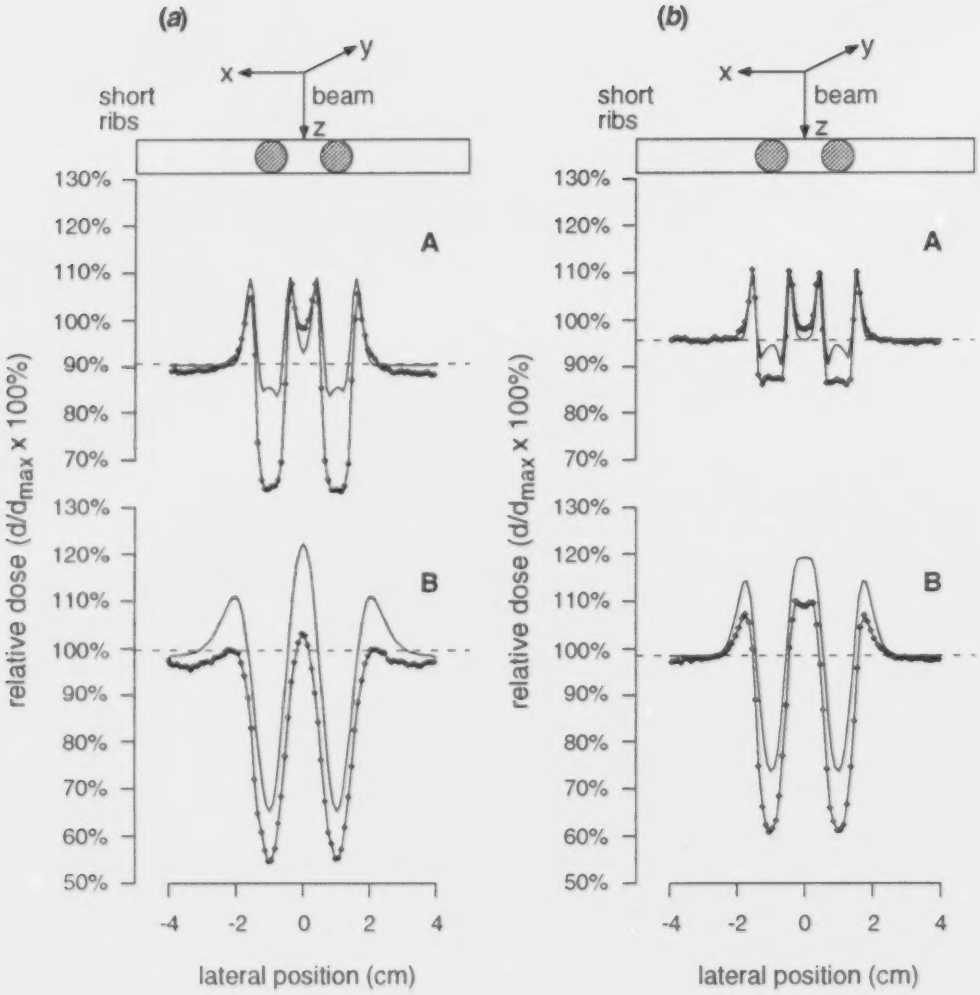

Figure III.6. Lateral dose profiles beyond two 'short ribs' separated by 1 cm and irradiated with 10 MeV (a) and 18 MeV (b) electrons. The diamonds are experimental data; the solid line is calculated; the dashed line is the dose in a homogeneous water phantom at the same depth. The profiles were at depths of 0.1 cm (A) and 1.1 cm (B) beyond the phantom, or 1.1 cm and 2.1 cm from the surface.

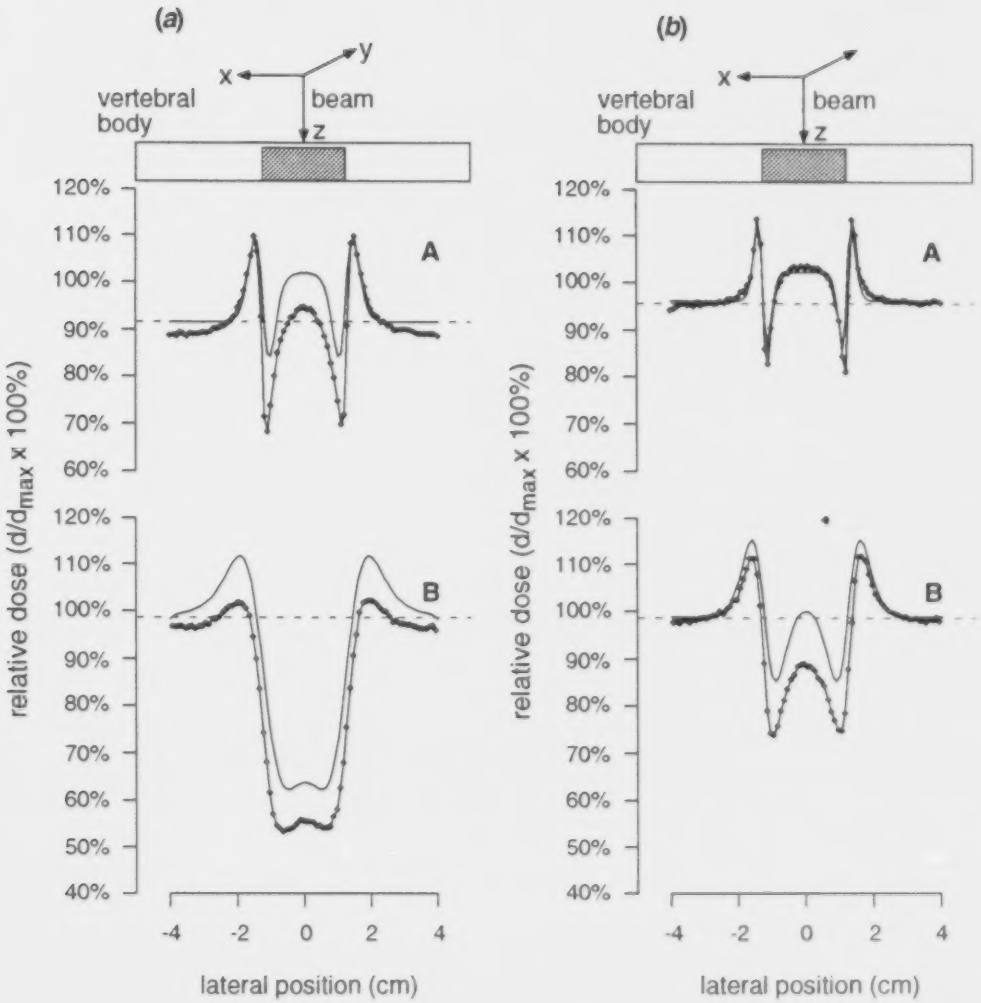

Figure III.7. Lateral dose profiles beyond a single 'vertebral body' irradiated with 10 MeV (a) and 18 MeV (b) electrons. The diamonds are experimental data; the solid line is calculated; the dashed line is the dose in a homogeneous water phantom at the same depth. The profiles were at depths of 0.1 cm (A) and 1.1 cm (B) beyond the phantom, or 1.25 cm and 2.25 cm from the surface.

the deeper depth, the electrons have scattered much further laterally, and a 2D description for the phantom is inadequate for both energies.

Figure III.8 shows the results for our 'spine' phantom, consisting of three of the coins from figure III.7, with a separation of 0.5 cm. Qualitatively, the results are almost identical to figure III.7. The measured and calculated profiles are again superpositions of the dose profiles from figure III.7, and the magnitudes of the dose overestimations is about the same.

Figure III.9 presents the data for the most complex phantom, simulating neck geometry. It consists of an air rod, 2.6 cm in diameter, simulating the trachea, which overlies the spine from figure III.8. The discrepancies between calculation and measurement are very large (40% for 10 MeV) and very graphically show the limitations of the 2D assumption in the MDAH algorithm. From the calculation's point of view, the phantom consists of a thin slab of wax, followed by a thick slab of air, followed by the spine phantom. In reality, there is wax at ± 1.3 cm in the y direction. This leads to preferential scattering of the electrons into the air space near $y=0.$, which is where the detector is located. Because of the extra fluence in the plane of the detector, the measured dose is much higher than the calculated dose between the vertebral bodies (coins).

The reason for the 2D assumption in the original implementation of the MDAH algorithm was computing time constraints. Since that time, computing speeds have increased by orders of magnitude. The calculation algorithm has been recently upgraded to get rid of the 2D assumption (Mah *et al* 1989, Starkschall *et al* 1991). Figure III.9 also shows the results of a 3D calculation for the trachea-spine geometry, and the agreement with measurement is much better than for the 2D calculation. The 3D calculation still fails to predict the magnitude of the difference between the measured hot and cold spots, but the general dose levels predicted are much closer to the measured values. As mentioned above,

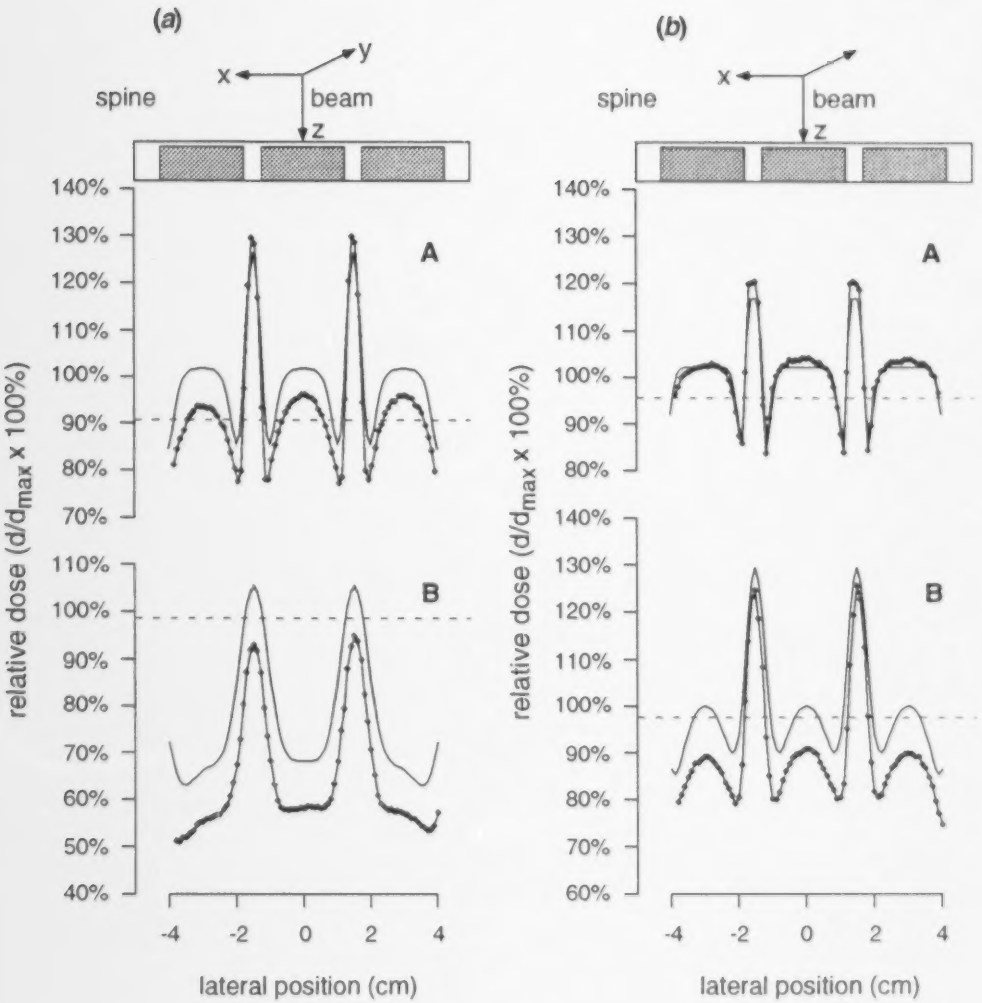

Figure III.8. Lateral dose profiles beyond the spine' irradiated with 10 MeV (a) and 18 MeV (b) electrons. The diamonds are experimental data; the solid line is calculated; the dashed line is the dose in a homogeneous water phantom at the same depth. The profiles were at depths of 0.1 cm (A) and 1.1 cm (B) beyond the phantom, or 1.24 cm and 2.24 cm from the surface.

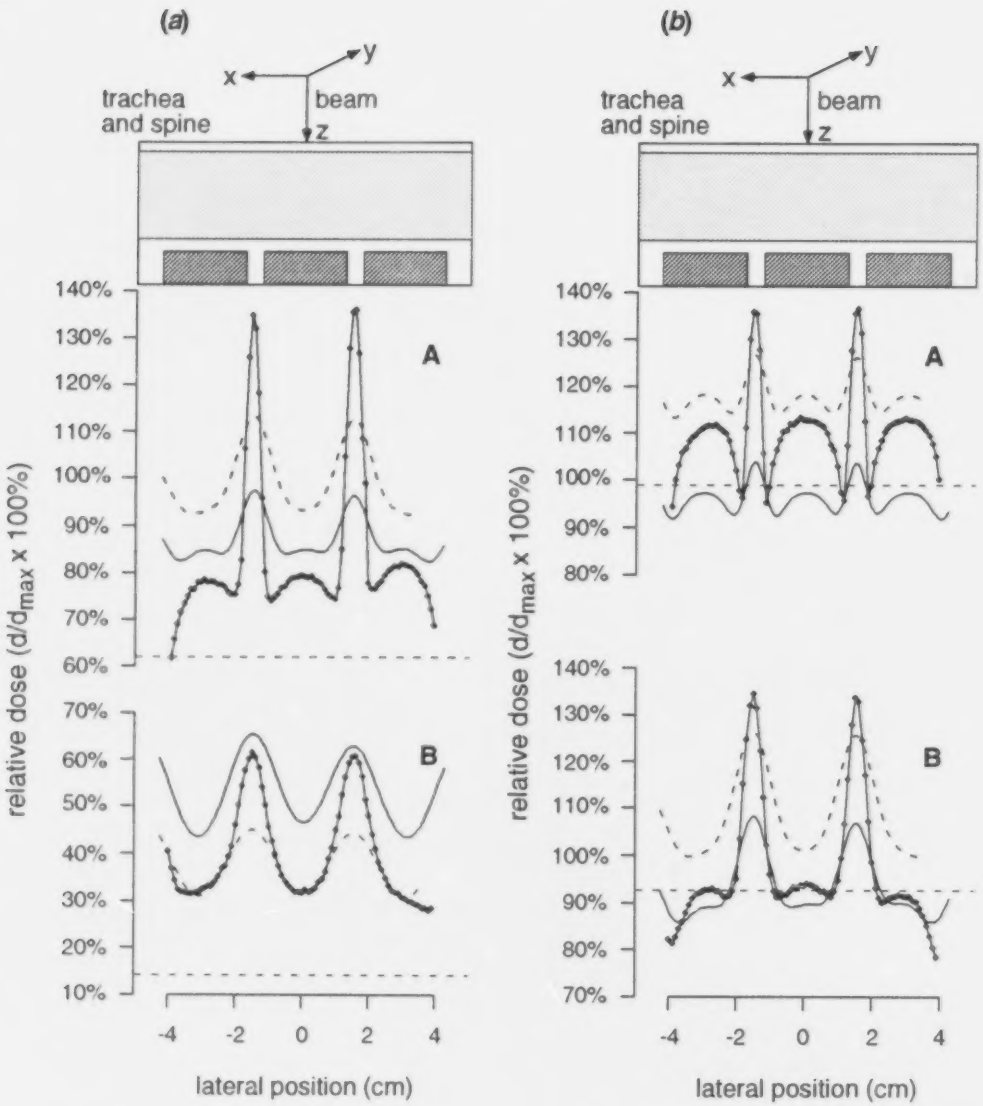

Figure III.9. Lateral dose profiles beyond the 'trachea' and 'spine' irradiated with 10 MeV (a) and 18 MeV (b) electrons. The diamonds are experimental data; the solid line is 2D calculated; the dashed curve is 3D calculated; the dashed straight line is the dose in a homogeneous water phantom at the same depth. The profiles were at depths of 0.1 cm (A) and 1.1 cm (B) beyond the phantom, or 4.36 cm and 5.36 cm from the surface.

the pencil beam width is not very narrow at depth, and qualitatively has the same effect on the dose profile 'waveform' as a low pass filter on the calculated profile.

B. Polystyrene Phantoms

1. Experimental method

Following the experiment above, it was felt that a more systematic evaluation of some parameters affecting the electron calculation was needed. To simplify the analysis, a single phantom configuration was chosen. The phantom consisted of a rectangular block of polystyrene ($12 \times 12 \times 1.3$ cm^3) into which a 1 cm diameter hole had been drilled. The hole was drilled off-center to more closely conform to standard geometry (Brahme 1983). Rods of 1 cm diameter were machined from three different materials, aluminum, hard bone analog, and soft bone analog, whose properties are listed in table III.2. The lengths of the rods varied from 1–10 cm. Using combinations of high density rods and polystyrene rods, a high density inclusion, from 1–10 cm long, could be positioned in the middle of the phantom.

The irradiation geometry, shown in figure III.10, was similar to the previous experimental setup, shown in figure III.2. However, instead of attaching the polystyrene phantom to the applicator, a combination of double sided tape and plastic angle brackets was used to position the phantom reproducibly with respect to the water phantom. The measurement technique was also improved (Antolak *et al* 1988) so that the radiation field could be completely mapped in a single plane. As before, the dose output was the ratio of the field and reference signals, and was normalized to the maximum signal in a homogeneous water phantom at 100 cm SSD.

The improvement is in the positional information available. A three-dimensional scanning dosimetry system (Therados RFA-3) was used to position the detector. The water tank is very similar to the LSC-2 system. One of the scanning modes of the RFA-3 system

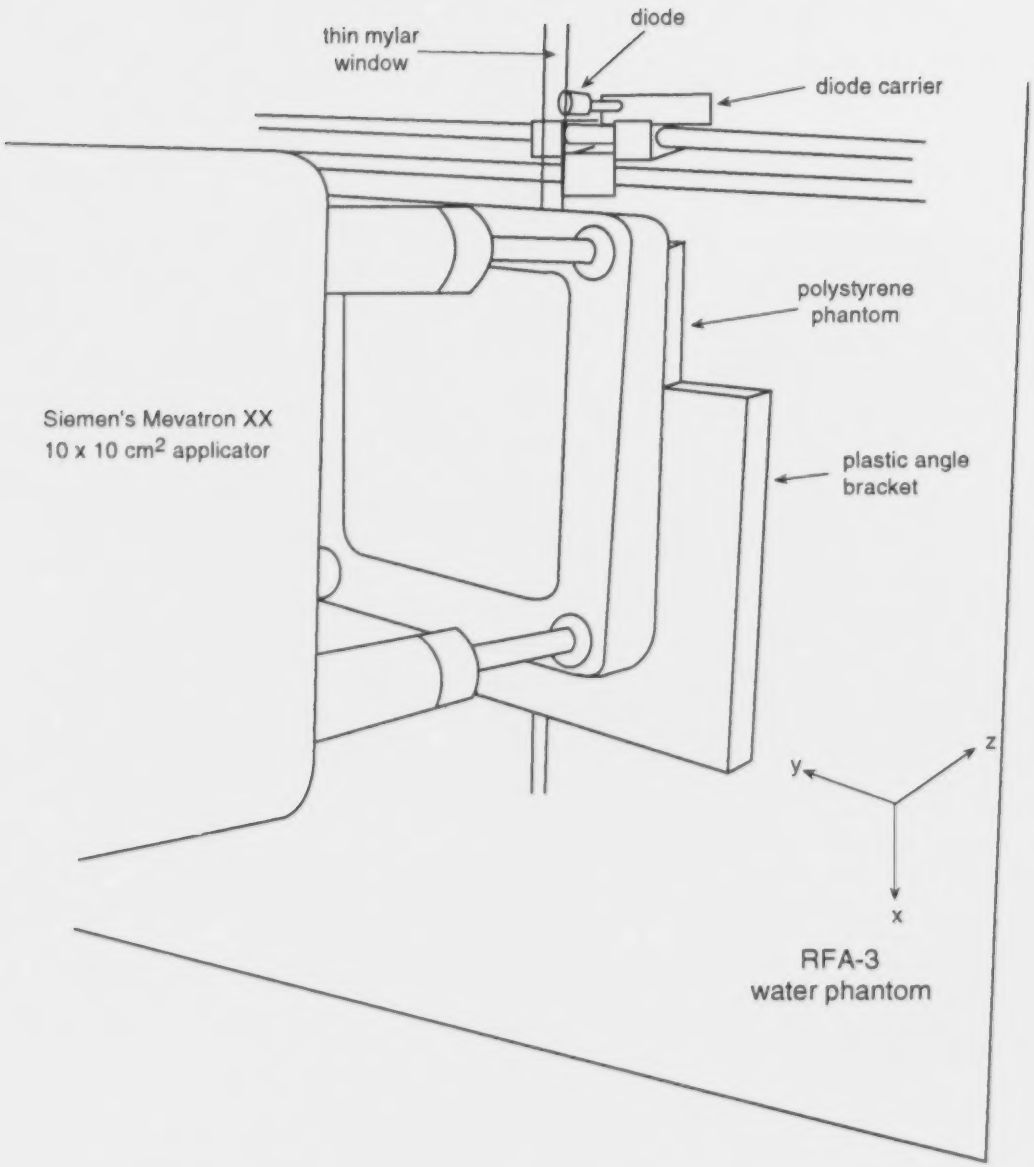

Figure III.10. Schematic diagram of the setup used for measuring dose distributions behind polystyrene phantoms with high density inclusions.

is a two-dimensional raster scanning mode. Referring to figure III.1, the diode is first scanned across the phantom in the x direction. At the end of the scan, the depth in the z direction is incremented and the diode scans across in the $-x$ direction. The width of the scan (in x), the scan increment (in z), and the number of scans are all adjustable from the RFA-3 controller. Analog voltages representing the x, y, z coordinates (calibrated to 50mV/cm) and dose were available from the controller.

The HP7090A digital X-Y recorder has three analog inputs available, so the scanning coordinate was input into channel 1, increment coordinate into channel 2, and dose output into channel 3. The HP7090A was interfaced to a microcomputer (PC/XT clone) using an IEEE-488 interface (National Instruments GPIB PC2A), and a schematic of the measurement setup is shown in figure III.11. A computer program was written in a high level language (Borland Turbo Pascal) which allowed the user to set various measurement parameters. Once the parameters were set, the measurement was initiated by starting the raster scanning from the RFA-3 controller. The computer gives the X-Y recorder instructions concerning the region of interest, and the recorder waits for the voltage on channel 1 (scanning coordinate) to fall within the region of interest, and starts filling its measurement buffers. the buffers are then downloaded to the microcomputer and the recorder given instructions for the next scan.

Using the known positional calibration (50mV/cm) and normalizing the dose output to the maximum dose output for a homogeneous water phantom, allowed us to recreate a series of dose profiles for a complete two-dimensional description of the radiation field. The data was interpolated onto a regular Cartesian grid for comparison with pencil beam calculations.

A further complication for these measurements was that a complete two-dimensional scan required 20–30 minutes. Over the period of time required for the complete series of measurements for a single energy (varying rod length and material), the

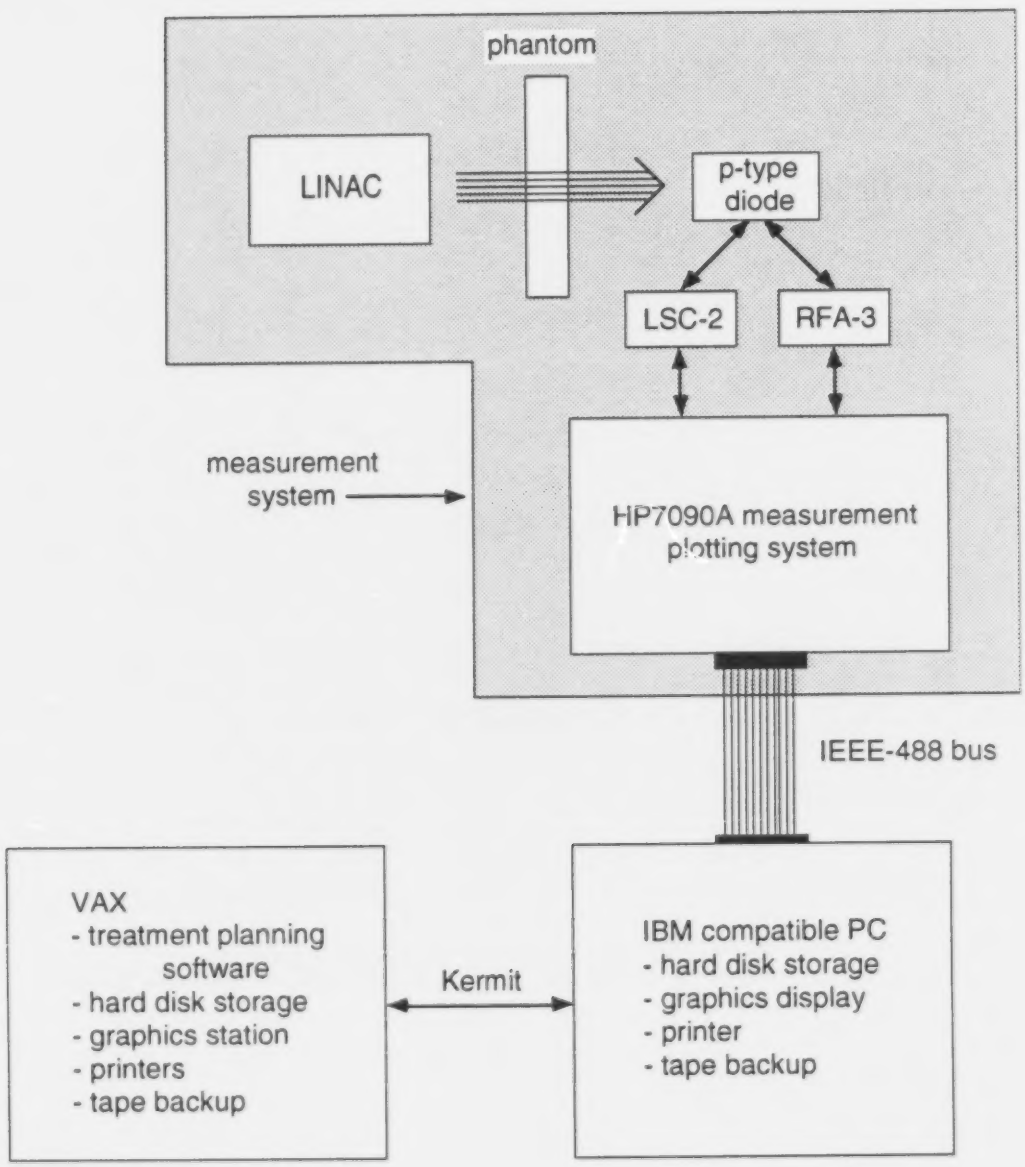

Figure III.11. The data acquisition and analysis system used for measuring dose distributions with the polystyrene phantoms. Most of the components can be substituted (e.g., treatment planning computer).

response of the diodes changed due to radiation damage from the large doses given to the diodes (Rikner and Grusell 1983). To compensate for this effect, a measurement was made at a fixed point (near the depth of maximum dose), without the polystyrene phantom present, after each two-dimensional scan was complete. The increase in relative response of the field-reference diode pair was approximately 12% over 31 measurements†, so the change from one measurement to the next was much less than 1%. Therefore, each two-dimensional scan was adjusted for diode response, but individual profiles in the two-dimensional scan were not adjusted relative to each other.

Once all normalizations and corrections had been performed, the data was transferred to the Alberta Treatment Planning system (Battista *et al* 1984) over a normal serial line using a file transfer program. A calculation module was written for the treatment planning system that allowed us to read the measured dose array from a text file and interpolate it onto the calculation grid. Pencil beam calculations were performed using the same grid, and the measured and calculated doses were subtracted from one another to give what we refer to as a dose difference map. A dose difference map consists of four dose maps, two of which are the dose arrays to be compared. The other two dose maps show where each dose matrix is greater than the other dose matrix.

2. Results and discussion

Some of the results are presented in figures III.12–III.23. All of these figures are presented in a similar format. The calculated and measured dose distributions, normalized to 100% at d_{max} in a 10×10 cm^2 field in a water phantom, are shown in the upper dose map. Since all of the phantoms in figures III.12–III.23 have mirror symmetry, only half of the dose distribution is shown, with the measured distribution on the left (*a*) and the calculated distribution on the right (*b*). The lower left map (*c*) shows where the measured

---

† Approximately 200,000 monitor units was given for the 31 measurements, corresponding to 2000 Gray maximum dose in a water phantom at 100 cm SSD.

dose is greater than the calculated dose, and the lower right map (*d*) shows where the calculated dose is greater. The values shown in (*c*) and (*d*) are obtained by subtracting the calculated and measured dose matrices.

Although measurements and calculations were performed for many different rod lengths, the main reason for this study was to highlight any differences between the 2D and 3D implementations of the MDAH algorithm. For this reason, it was decided to present the results of the calculations and measurements for 1 cm length rods, where the difference between the 2D and 3D implementations was greatest.

Figures III.12–III.17 show comparisons between calculated and measured distributions for a 10×10 cm^2, 10 MeV beam incident on the polystyrene phantom with a 1 cm long rod perpendicular to the page. Figures III.12 and III.13 show the comparison between measured and calculated dose distributions for an aluminum rod. The calculation was performed using the 2D and 3D implementations of the MDAH algorithm, respectively. Similarly, figures III.14–III.17 show the results for hard bone and soft bone analogs. The phantoms and some results are summarized in table III.2.

Figure III.12 compares the measured and calculated (2D) dose distributions for a 1 cm long aluminum rod. The 2D calculation cannot distinguish that the rod has a finite length (relative to the field), therefore the algorithm scatters electrons from a 10 cm aluminum rod. This leads to an excess of dose deposited in the immediate shadow of the rod, because of more scatter from the 'extra' aluminum in the calculation. Ignoring the penumbral region (see below), the maximum discrepancy is approximately 25%. The 3D calculation, whose results are shown in figure III.13, improves on the 2D algorithm because it is given off-axis information about the phantom composition. The maximum discrepancy is reduced by a factor of two to approximately 12%. This improvement in 3D versus 2D is maintained as the rod material changes to hard bone (figures III.14 and III.15) and soft bone (figures III.16 and III.17). The magnitude of the error also decreases as the

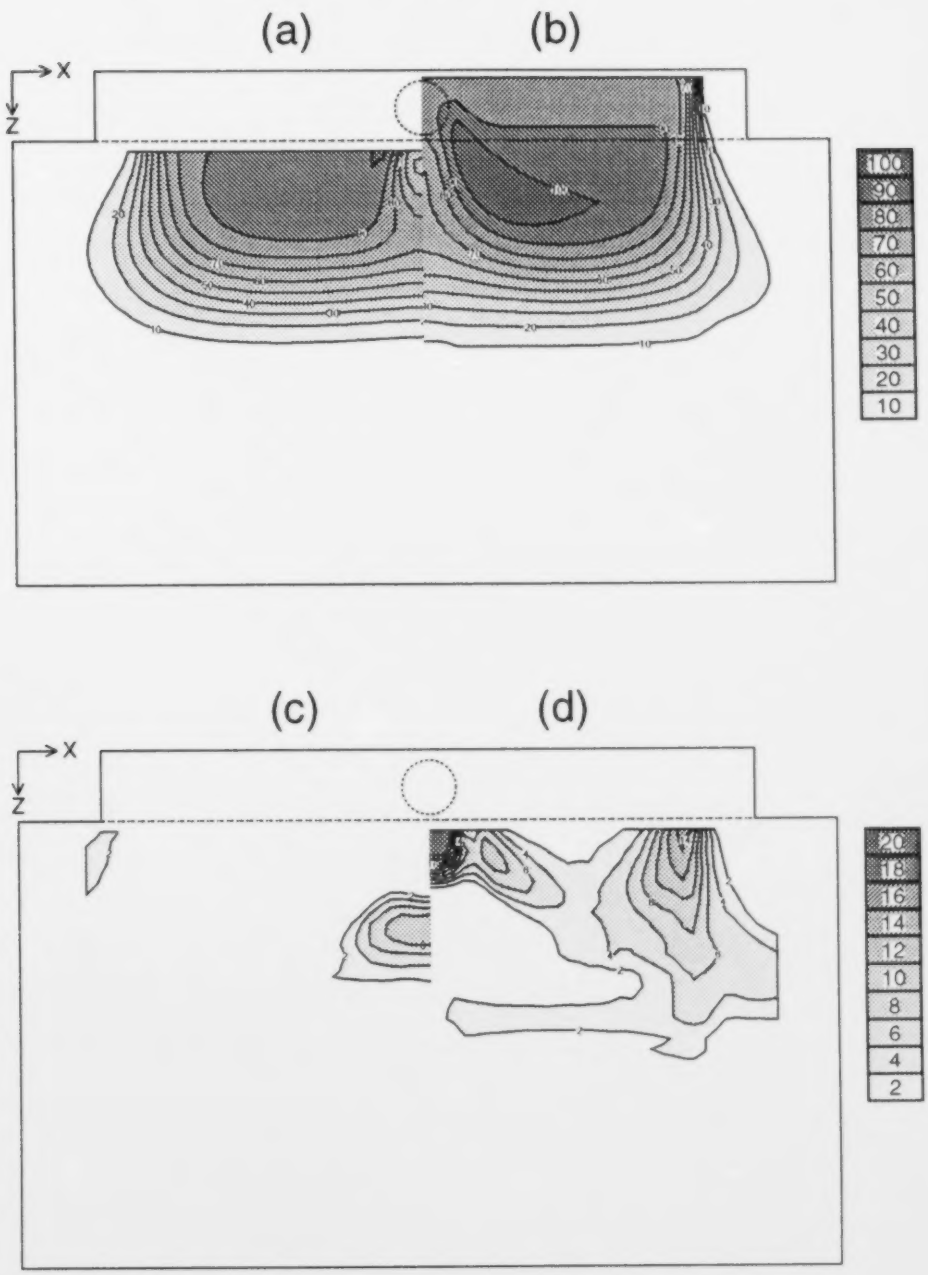

Figure III.12. Dose distribution behind a 1 cm long aluminum rod irradiated by a 10 cm square field of 10 MeV electrons. The rod is located 0.2 cm from the top surface of a 1.3 cm thick polystyrene slab. (a) Measured distribution; (b) calculated distribution (2D); (c) measured greater than calculated; (d) calculated greater than measured.

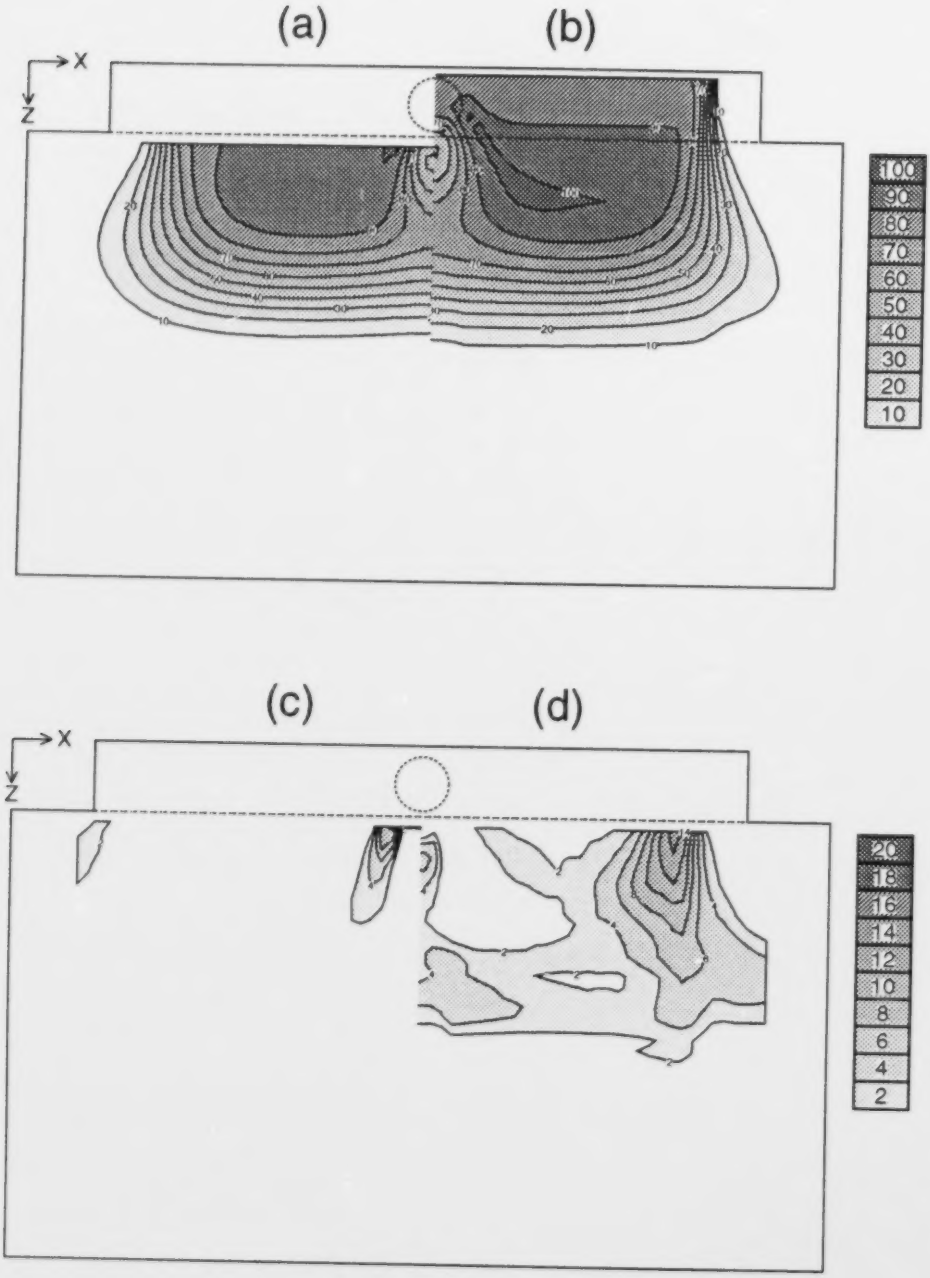

Figure III.13. Dose distribution behind a 1 cm long aluminum rod irradiated by a 10 cm square field of 10 MeV electrons. The rod is located 0.2 cm from the top surface of a 1.3 cm thick polystyrene slab. (a) Measured distribution; (b) calculated distribution (3D); (c) measured greater than calculated; (d) calculated greater than measured.

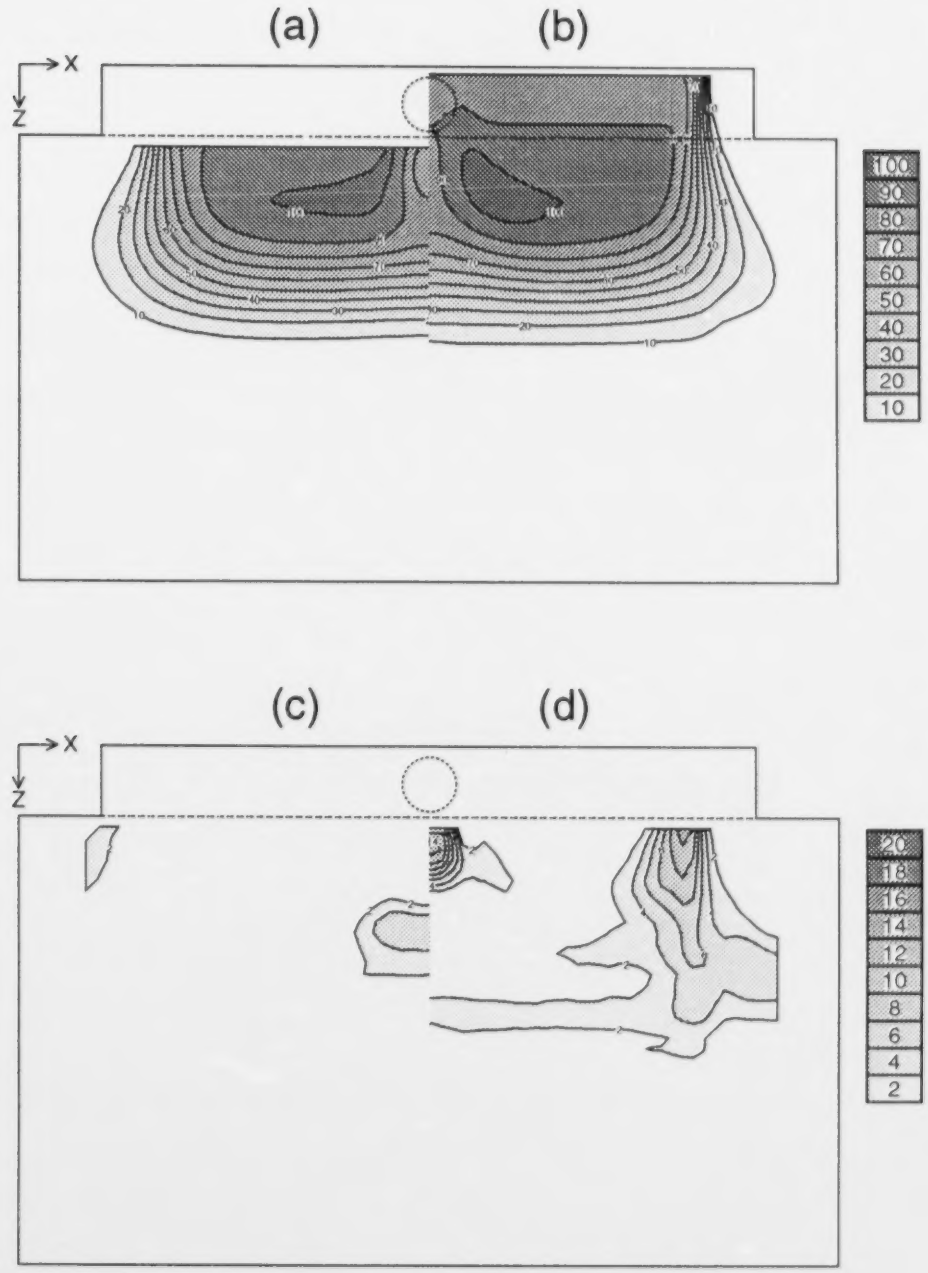

Figure III.14. Dose distribution behind a 1 cm long hard bone rod irradiated by a 10 cm square field of 10 MeV electrons. The rod is located 0.2 cm from the top surface of a 1.3 cm thick polystyrene slab. (a) Measured distribution; (b) calculated distribution (2D); (c) measured greater than calculated; (d) calculated greater than measured.

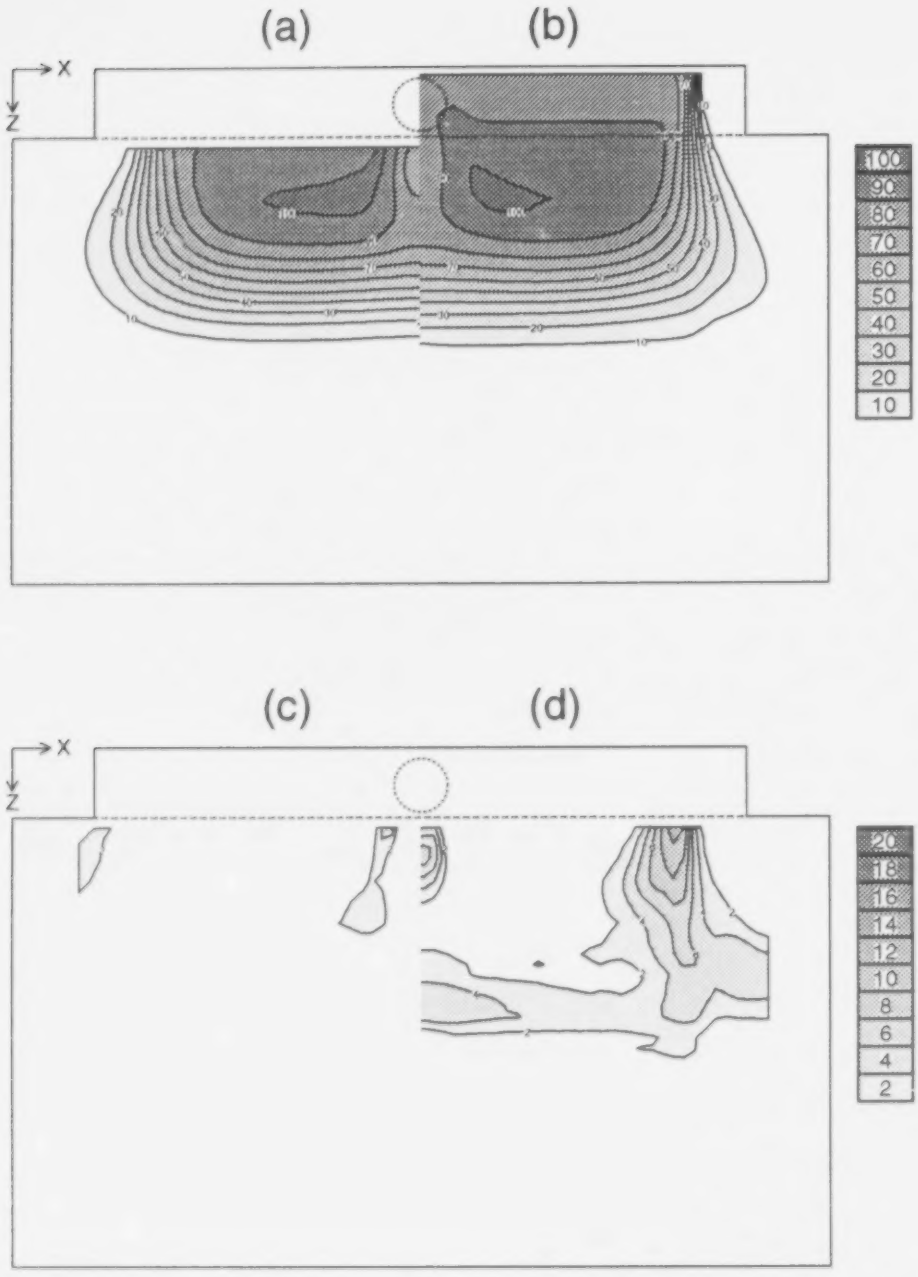

Figure III.15. Dose distribution behind a 1 cm long hard bone rod irradiated by a 10 cm square field of 10 MeV electrons. The rod is located 0.2 cm from the top surface of a 1.3 cm thick polystyrene slab. (a) Measured distribution; (b) calculated distribution (3D); (c) measured greater than calculated; (d) calculated greater than measured.

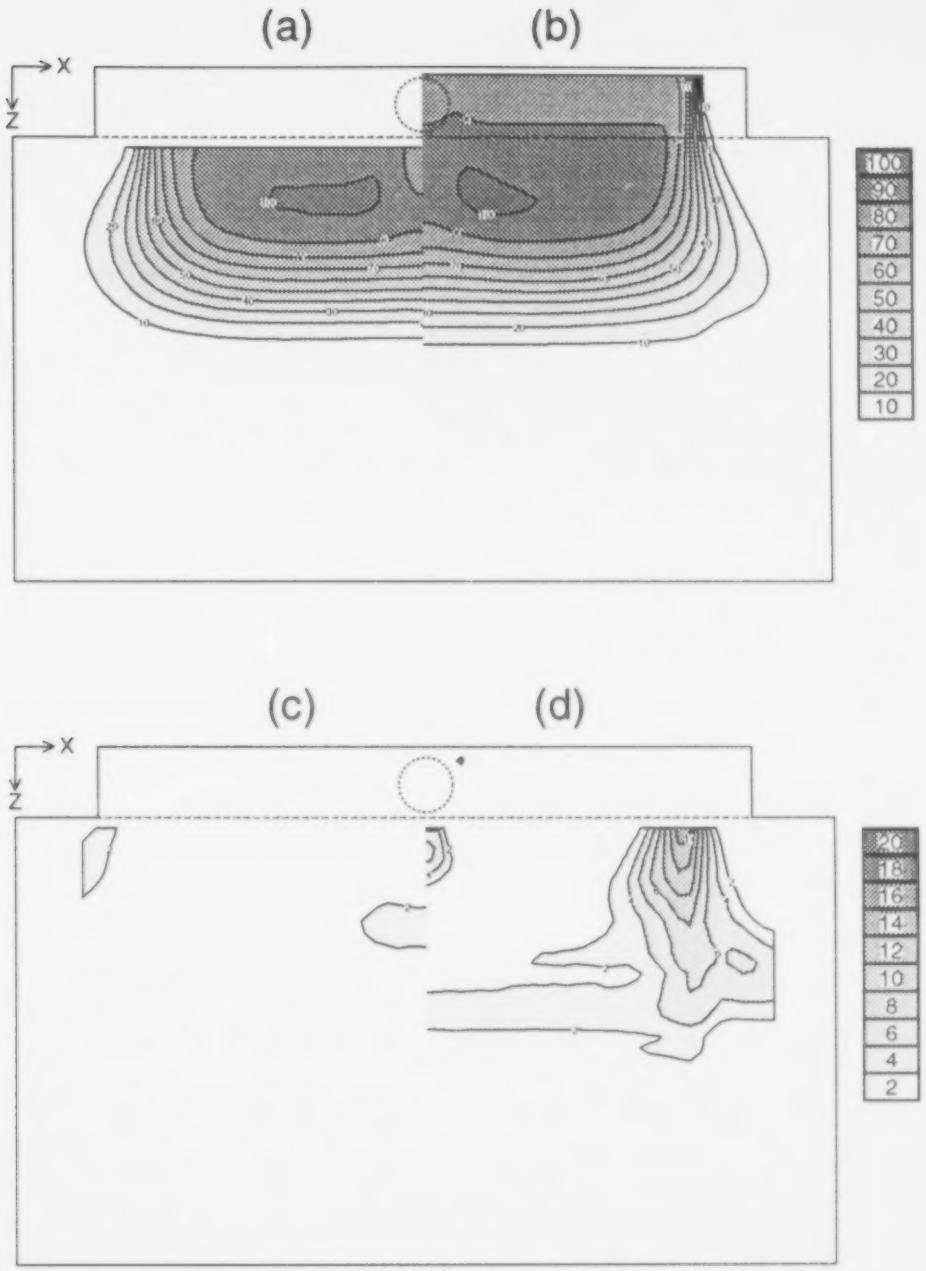

Figure III.16. Dose distribution behind a 1 cm long soft bone rod irradiated by a 10 cm square field of 10 MeV electrons. The rod is located 0.2 cm from the top surface of a 1.3 cm thick polystyrene slab. (a) Measured distribution; (b) calculated distribution (2D); (c) measured greater than calculated; (d) calculated greater than measured.

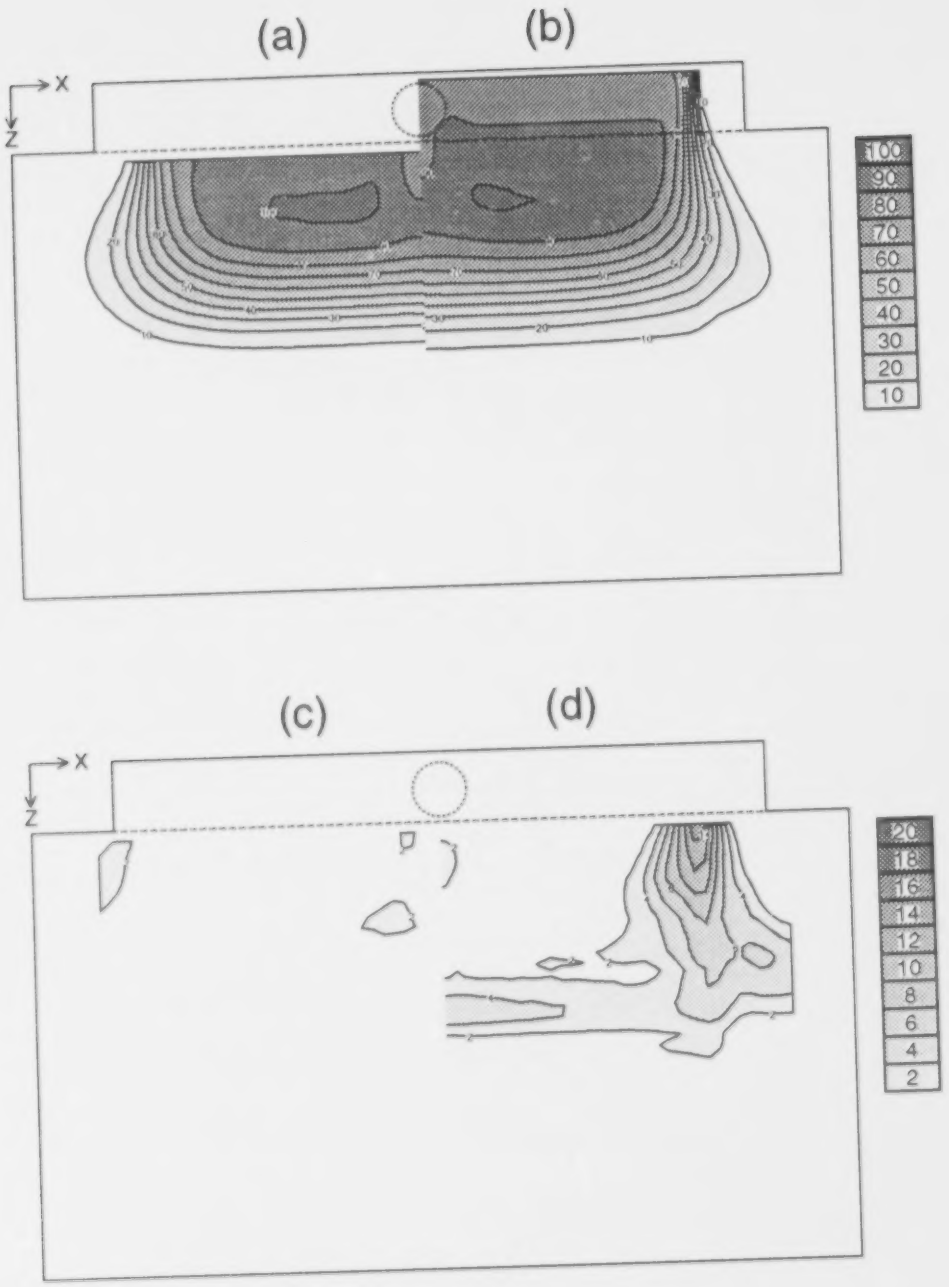

Figure III.17. Dose distribution behind a 1 cm long soft bone rod irradiated by a 10 cm square field of 10 MeV electrons. The rod is located 0.2 cm from the top surface of a 1.3 cm thick polystyrene slab. (a) Measured distribution; (b) calculated distribution (3D); (c) measured greater than calculated; (d) calculated greater than measured.

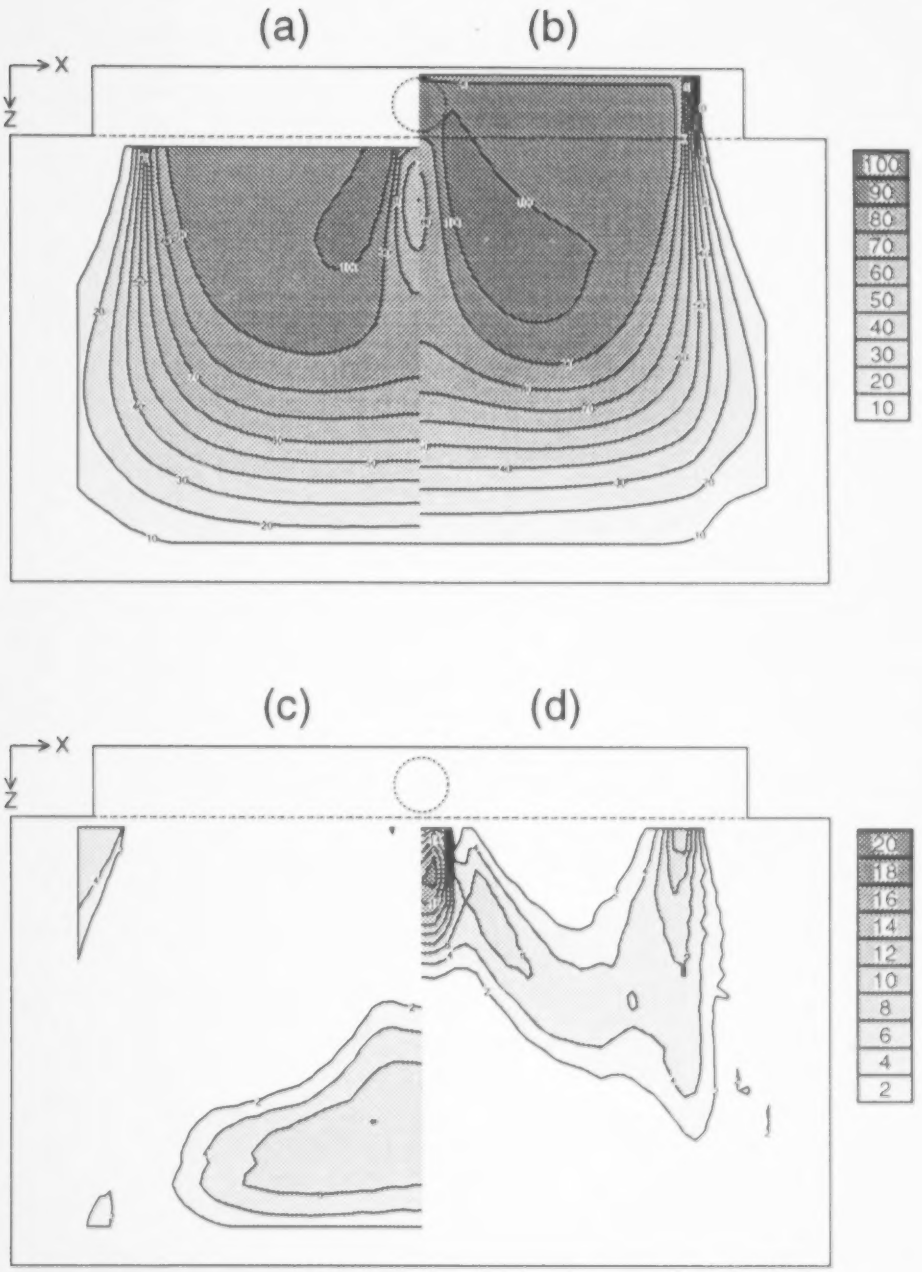

Figure III.18. Dose distribution behind a 1 cm long aluminum rod irradiated by a 10 cm square field of 18 MeV electrons. The rod is located 0.2 cm from the top surface of a 1.3 cm thick polystyrene slab. (a) Measured distribution; (b) calculated distribution (2D); (c) measured greater than calculated; (d) calculated greater than measured.

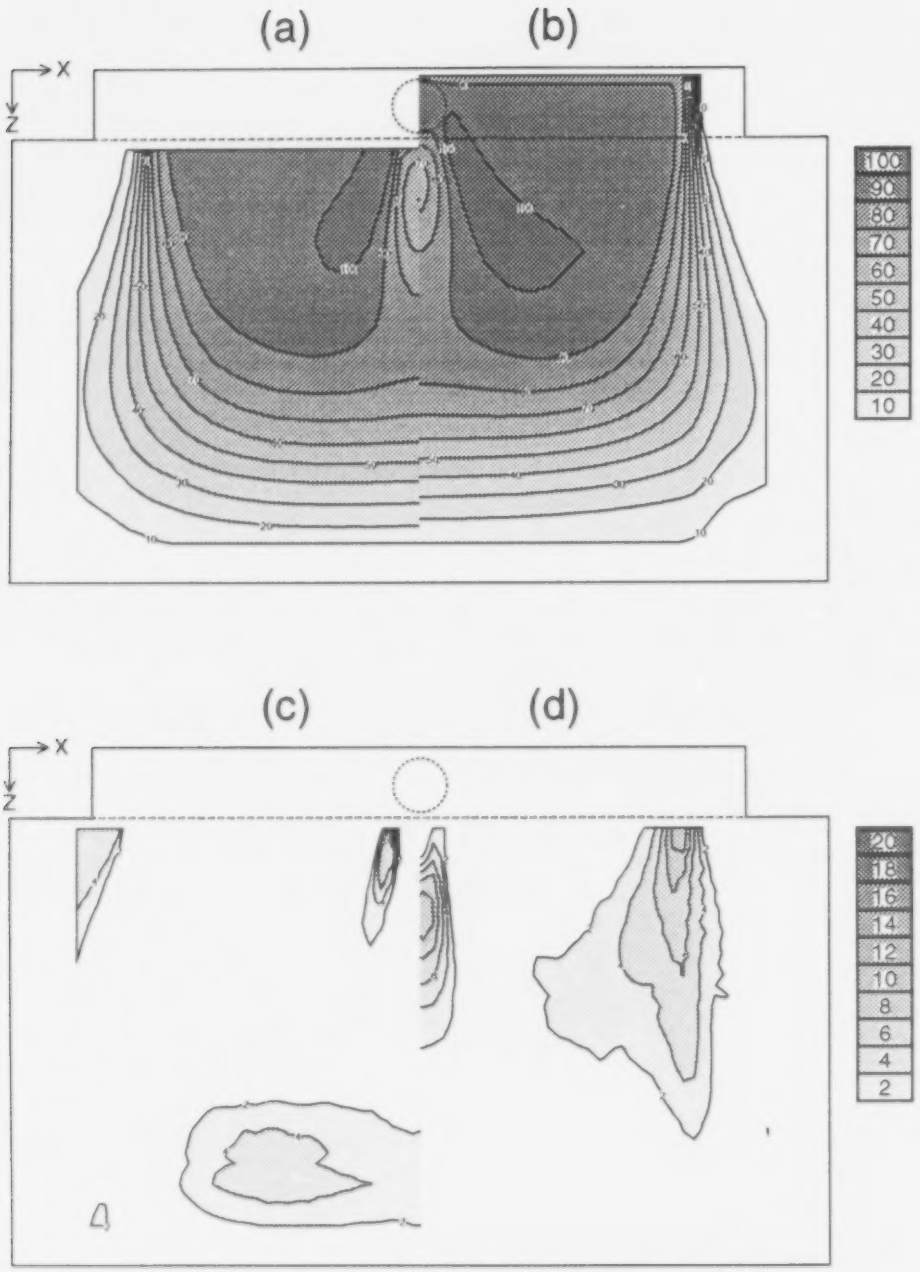

Figure III.19. Dose distribution behind a 1 cm long aluminum rod irradiated by a 10 cm square field of 18 MeV electrons. The rod is located 0.2 cm from the top surface of a 1.3 cm thick polystyrene slab. (a) Measured distribution; (b) calculated distribution (3D); (c) measured greater than calculated; (d) calculated greater than measured.

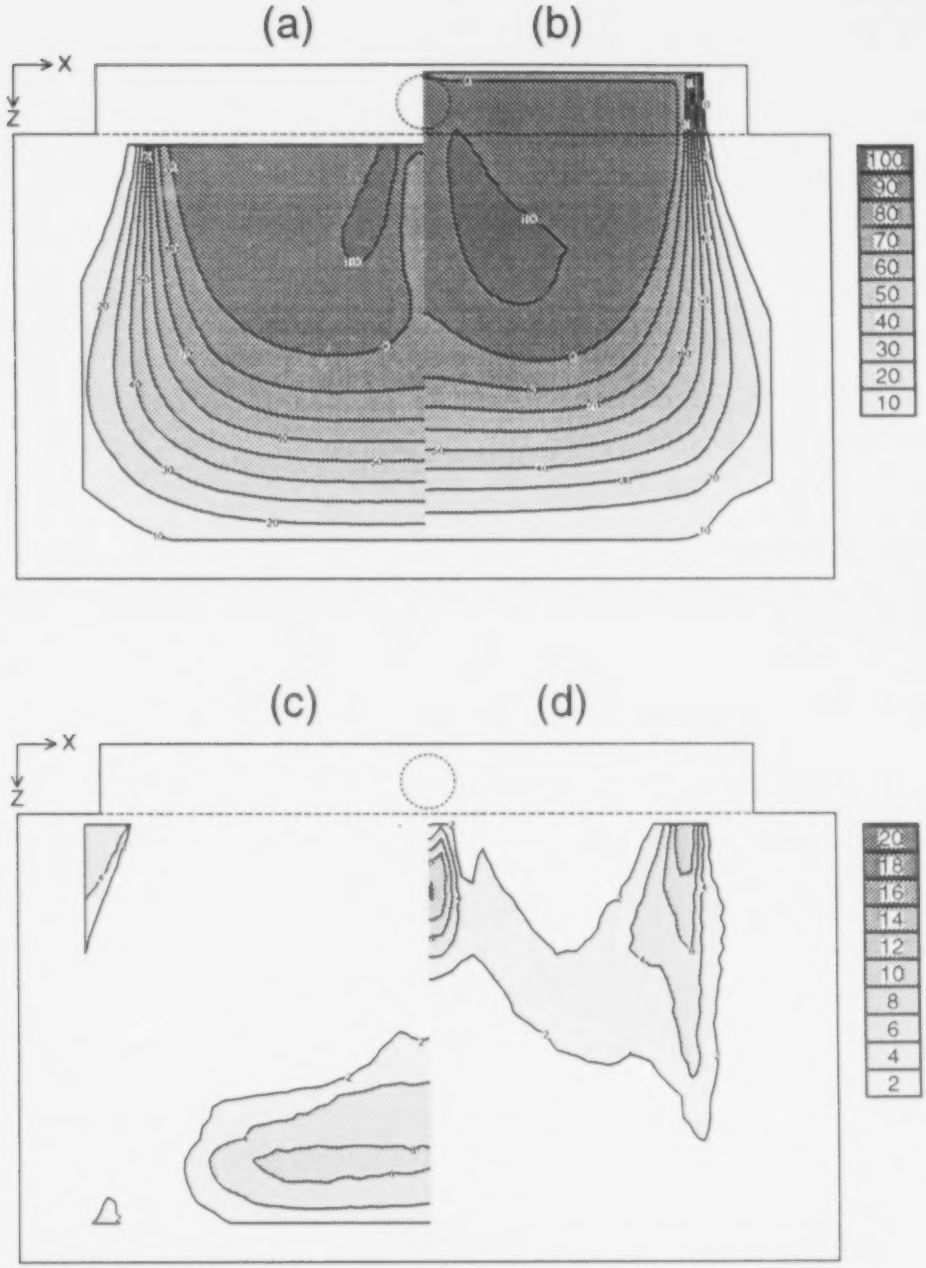

Figure III.20. Dose distribution behind a 1 cm long hard bone rod irradiated by a 10 cm square field of 18 MeV electrons. The rod is located 0.2 cm from the top surface of a 1.3 cm thick polystyrene slab. (a) Measured distribution; (b) calculated distribution (2D); (c) measured greater than calculated; (d) calculated greater than measured.

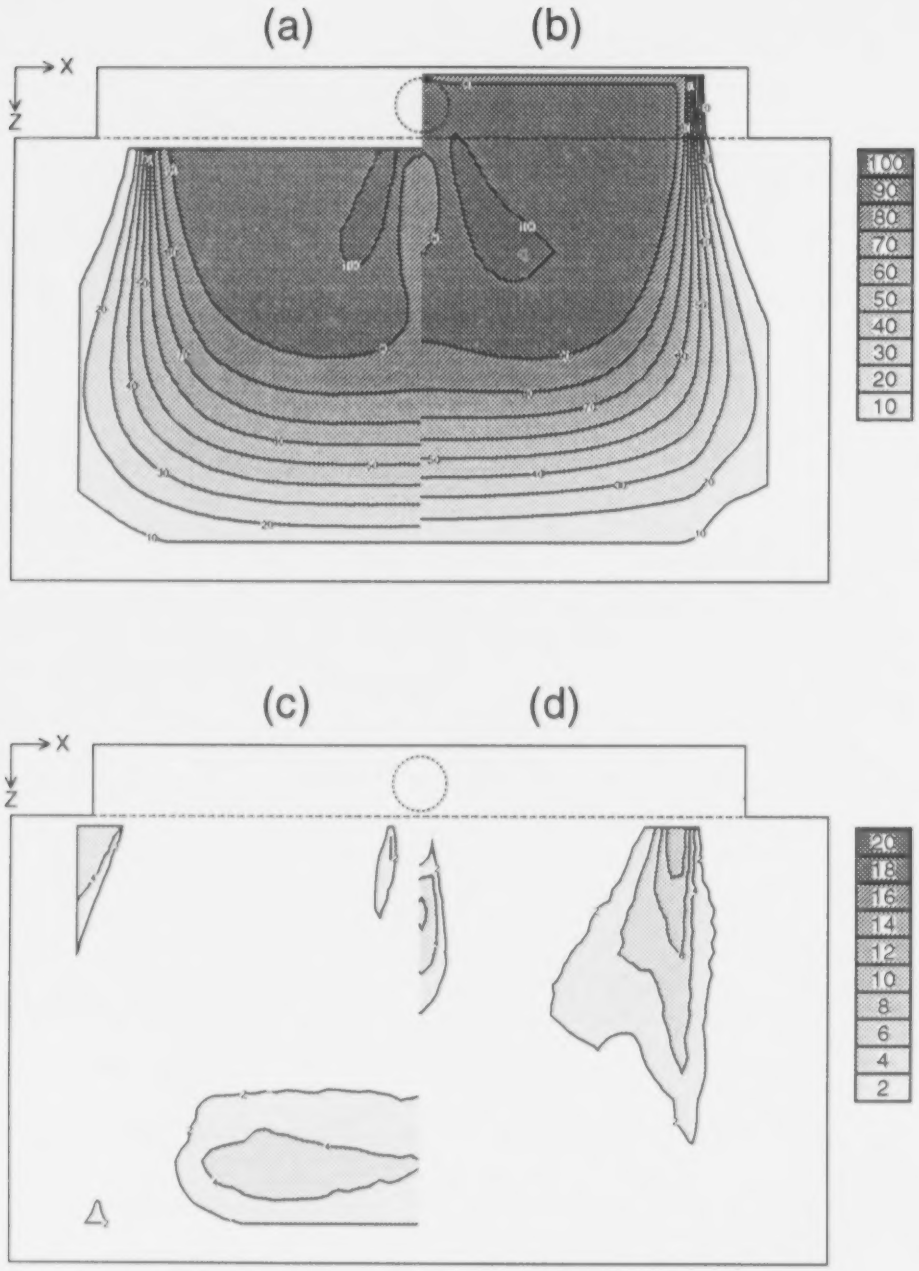

Figure III.21. Dose distribution behind a 1 cm long hard bone rod irradiated by a 10 cm square field of 18 MeV electrons. The rod is located 0.2 cm from the top surface of a 1.3 cm thick polystyrene slab. (a) Measured distribution; (b) calculated distribution (3D); (c) measured greater than calculated; (d) calculated greater than measured.

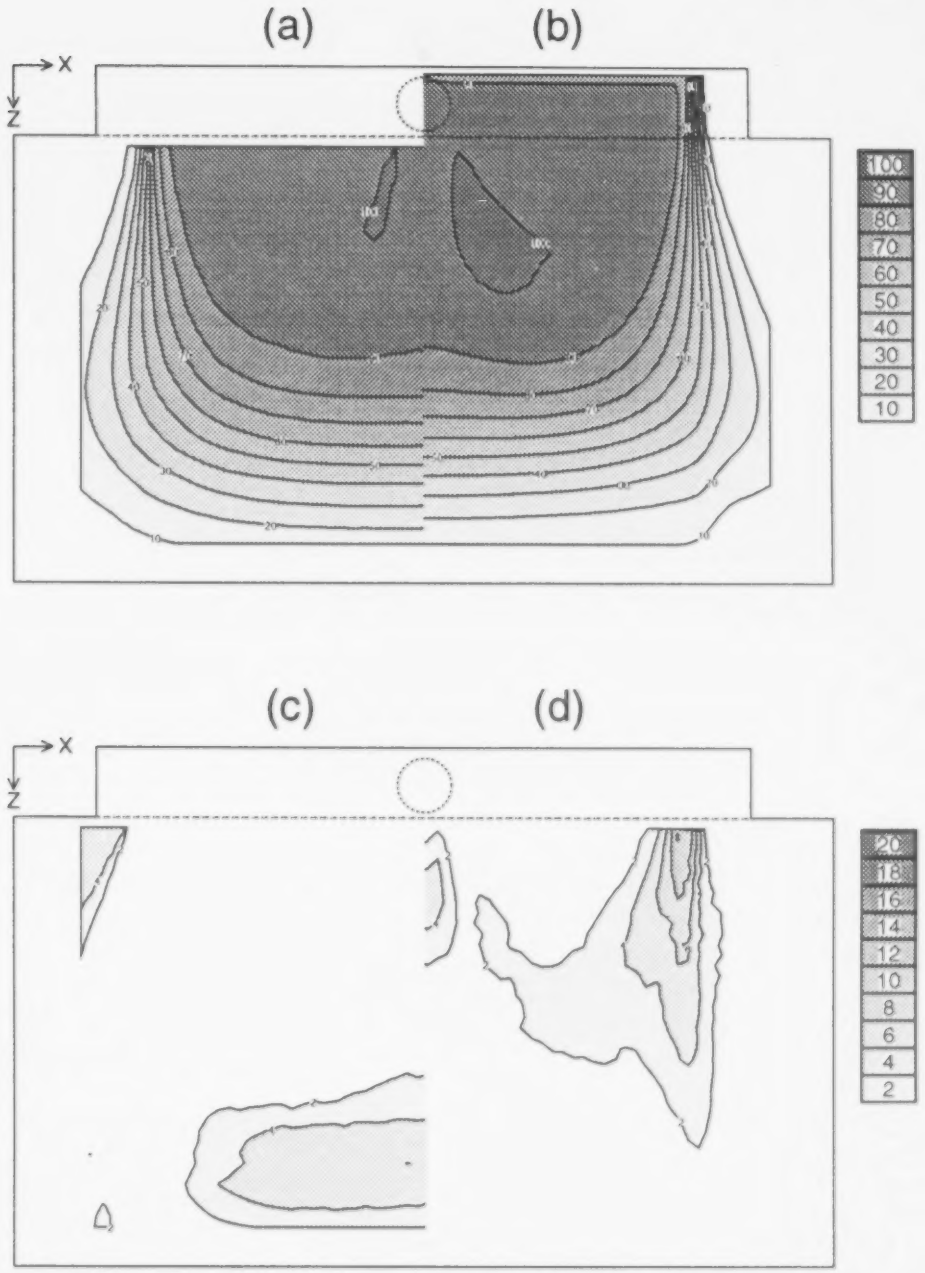

Figure III.22. Dose distribution behind a 1 cm long soft bone rod irradiated by a 10 cm square field of 18 MeV electrons. The rod is located 0.2 cm from the top surface of a 1.3 cm thick polystyrene slab. (a) Measured distribution; (b) calculated distribution (2D); (c) measured greater than calculated; (d) calculated greater than measured.

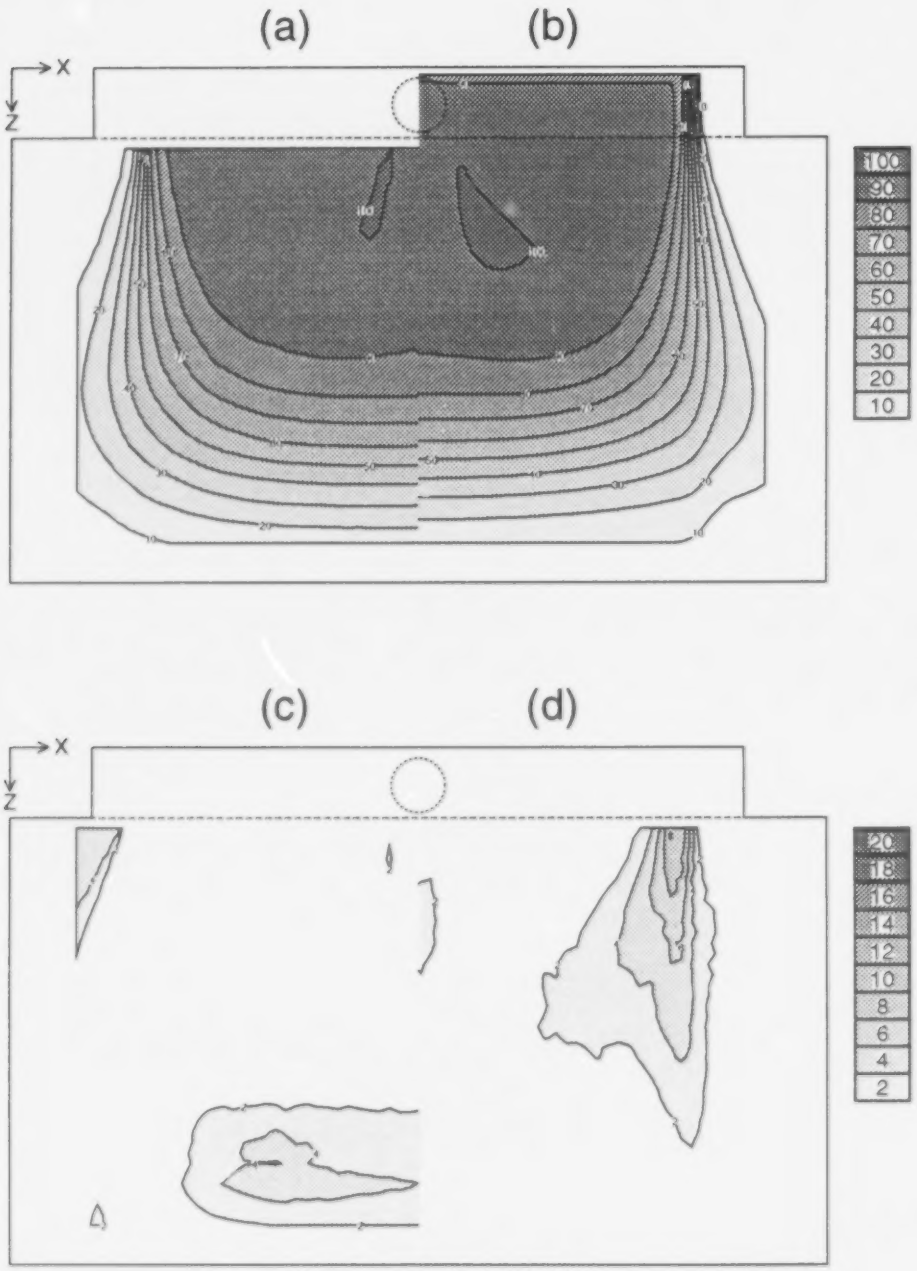

Figure III.23. Dose distribution behind a 1 cm long soft bone rod irradiated by a 10 cm square field of 18 MeV electrons. The rod is located 0.2 cm from the top surface of a 1.3 cm thick polystyrene slab. (a) Measured distribution; (b) calculated distribution (3D); (c) measured greater than calculated; (d) calculated greater than measured.

density of the heterogeneity approaches unit density, which is expected. The maximum difference between the measured distribution behind the soft bone rod and the 2D calculation (figure III.16) is approximately 6% and it could be argued that the 2D calculation is adequate in this case.

Figures III.18–III.23 show the results for the same phantoms as figures III.12–III.17, but for an 18 MeV beam of electrons. Qualitatively, the results are very similar to the 10 MeV beam in figures III.12–III.17, and again the 3D calculation improves upon the 2D calculation by approximately a factor of two. Table III.2 summarizes the maximum discrepancies found in figures III.12–III.23.

In all of the figures III.12–III.23, there appears to be a large discrepancy in the penumbral region at the beam edge, where the calculated dose is much greater, as seen in part (*d*) of the figures. This is because the algorithm (both 2D and 3D) has some difficulty

Table III.2. The maximum discrepancies between measurement and calculation for a 1 cm rod in polystyrene for 10 MeV and 18 MeV electrons, and some of the results from figures III.12–III.23, ignoring the penumbral region. The maximum error is given with two numbers—positive for calculation greater than measurement and negative for calculation less than measurement.

Figure	Rod material	CT†	Electron density‡	Energy (MeV)	Calculation Method	Maximum Error	
III.12	aluminum	2225	2.12	10	2D	+25%	-10%
III.13	aluminum	2225	2.12	10	3D	+12%	-3%
III.14	hard bone	1080	1.57	10	2D	+14%	-6%
III.15	hard bone	1080	1.57	10	3D	+7%	-5%
III.16	soft bone	495	1.29	10	2D	+6%	-3%
III.17	soft bone	495	1.29	10	3D	+3%	-3%
III.18	aluminum	2225	2.12	18	2D	+18%	-7%
III.19	aluminum	2225	2.12	18	3D	+10%	-6%
III.20	hard bone	1080	1.57	18	2D	+10%	-6%
III.21	hard bone	1080	1.57	18	3D	+6%	-3%
III.22	soft bone	495	1.29	18	2D	+4%	-5%
III.23	soft bone	495	1.29	18	3D	+2%	-2%

† CT number in Houndsfield units.
‡ Electron density relative to water.

modeling the penumbral region and the exact width of the beam. Since there is a high gradient in this dose region, small errors in position can lead to large errors in dose. However, the positional errors of the isodose lines are of primary importance and are actually quite small. For that reason, the penumbral region was ignored in the discussion above.

The measured and calculated data for the polystyrene phantoms was also used to illustrate the progression between 2D and 3D phantoms. To simplify the analysis, the mean of the squares of the differences between two given dose distributions was used as a numerical measure of the 'total' discrepancy between the dose distributions. If the dose matrices are represented by d_1 and d_2, then the mean square difference is given by

$$S = \frac{1}{N} \sum_i \sum_j \left\{ d_1(i,j) - d_2(i,j) \right\}^2 \qquad \text{(III.1)}$$

where i and j are row and column indices and N is the total number of points compared.

Figure III.24 plots the mean square difference between the measured dose distributions for different length rods in a 10 MeV beam, and the measured dose distribution for the 10 cm rod. The horizontal axis is the length of the rod, whose dose distribution is compared to the measured dose distribution for the 10 cm rod. For aluminum and hard bone, the mean square difference for the 1 cm measured dose distribution versus the 10 cm measured dose distribution is significantly higher than for the 8 cm measured dose distribution. The mean square difference is quite small and changes little as the rod gets longer than 3 cm. This means that for high density inclusions near the surface, the 3 cm (or longer) rod is a 2D heterogeneity, since there is little difference compared to the 10 cm rod, which extends the entire length of the electron field. For the soft bone analog, however, there is little difference between the dose distributions for any length rod.

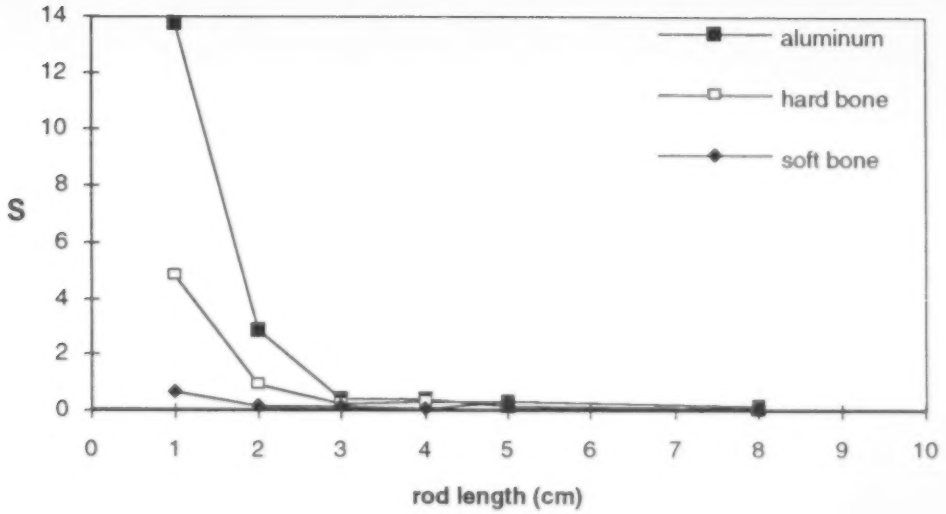

Figure III.24. Mean of the squares of the differences between the measured 10 cm rod dose distribution for 10 MeV, and the measured dose distributions for other lengths.

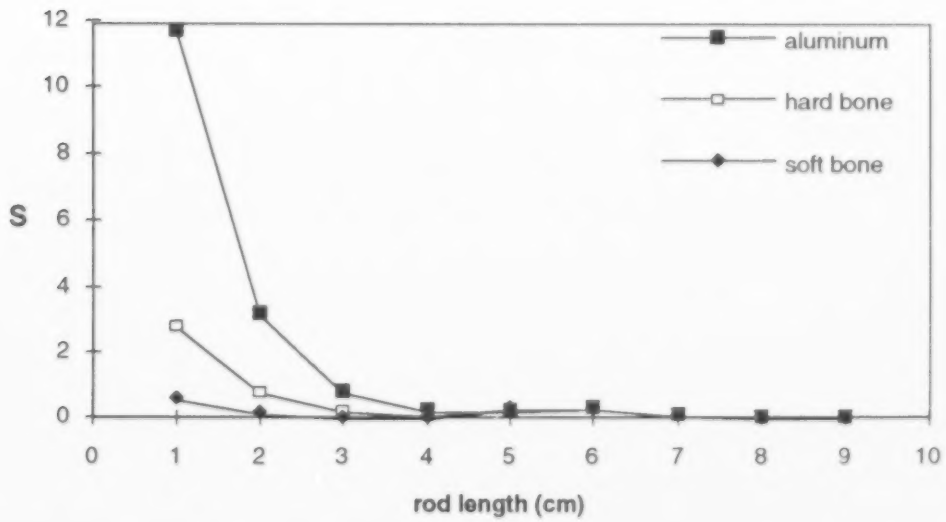

Figure III.25. Mean of the squares of the differences between the calculated 10 cm rod dose distribution for 10 MeV, and the calculated dose distributions for other lengths.

Figure III.25 is similar to figure III.24, except that calculated 3D dose distributions are being compared. Qualitatively, the results are similar to the previous figure, which means that the calculated dose distributions are behaving similarly to the measured dose distributions, in their progression from 2D to 3D phantoms. This implies that unless the rod length is 3 cm or less, there is very little to be gained with the 3D version of the MDAH pencil beam algorithm, compared to the 2D version.

C. Anthropomorphic Phantom[†]

1. Statement of problem

Electron beams have been in use at this institute for many years. The general practice has been to prescribe field size and shape based on the target volume and energy based on the penetration required. This is sufficient in simple cases, but is less than optimum for tumor sites involving irregular patient contours and heterogeneities. To complicate matters, bolus is often used, resulting in even more irregular patient contours. In the case of head and neck tumors, such as esophagus, larynx, thyroid, and tonsils, treatment can consist of a single anterior electron field, perhaps in combination with two or more photon beams, or other form of treatment. The photon fields are generally quite simple (e.g. parallel opposed (AP/PA) fields), and the dose distributions are fairly well understood. For the purpose of this study, we therefore concentrated on the electron fields and the problem of bolus design.

2. Method and results

A patient with thyroid cancer was chosen for this study. An immobilization shell was constructed and the patient was simulated to define the extent of the photon fields. The patient proceeded to treatment and a CT study in treatment position was obtained for electron treatment planning purposes. The patient contour and 80% target volume for the

---

† A version of this section has been accepted for publication (Antolak *et al* 1992).

electron field are shown in figure III.26. The spinal cord was specified as a critical region to receive no more than 60% of the given dose‡. The treatment plan in figure III.26 shows the dose distribution from an anterior electron field in which the spinal cord receives approximately 80% dose, so bolus was needed for shielding purposes.

Two methods were used to design the bolus†. The thickness of the wax for the first method was equal to the difference between the radiological depth of the anterior edge of the vertebral bodies and R_{80} for 16 MeV electrons. The width of the wax bolus was approximately the same as the width of the vertebral bodies since the target volume includes areas lateral to the spinal cord. The dose was calculated using a 3D implementation (Mah *et al* 1989) of the MDAH pencil beam algorithm (Hogstrom *et al* 1981), developed at this institute. Figure III.27 shows the bolus in place, and resulting dose distribution, normalized to the maximum dose in a water phantom at an SSD equal to the source to immobilization shell distance. Notice that a fairly large section of the target volume does not receive 80% dose as prescribed. Dose homogeneity is also poor because of the high dose regions lateral to the bolus.

A second bolus was designed by manually changing the bolus outline on the treatment plan and recalculating the dose distribution. After many iterations, we arrived at the bolus design shown in figure III.28. This bolus is much smaller and the sides have been flared out. The calculated isodoses show good coverage of the target volume by the 80% isodose line, and the spinal cord receives no more than 60%, as prescribed.

As mentioned above, a 3D pencil beam algorithm was used to perform the dose calculations. This required adjustment of the bolus in all of the CT slices before

---

‡ The given dose is the maximum dose in a flat water phantom at the same SSD as the central ray of the applied electron beam. This is also the default normalization used by the treatment planning system for electron beams.

† A summary of different techniques for electron bolus design is given by Low *et al* 1992.

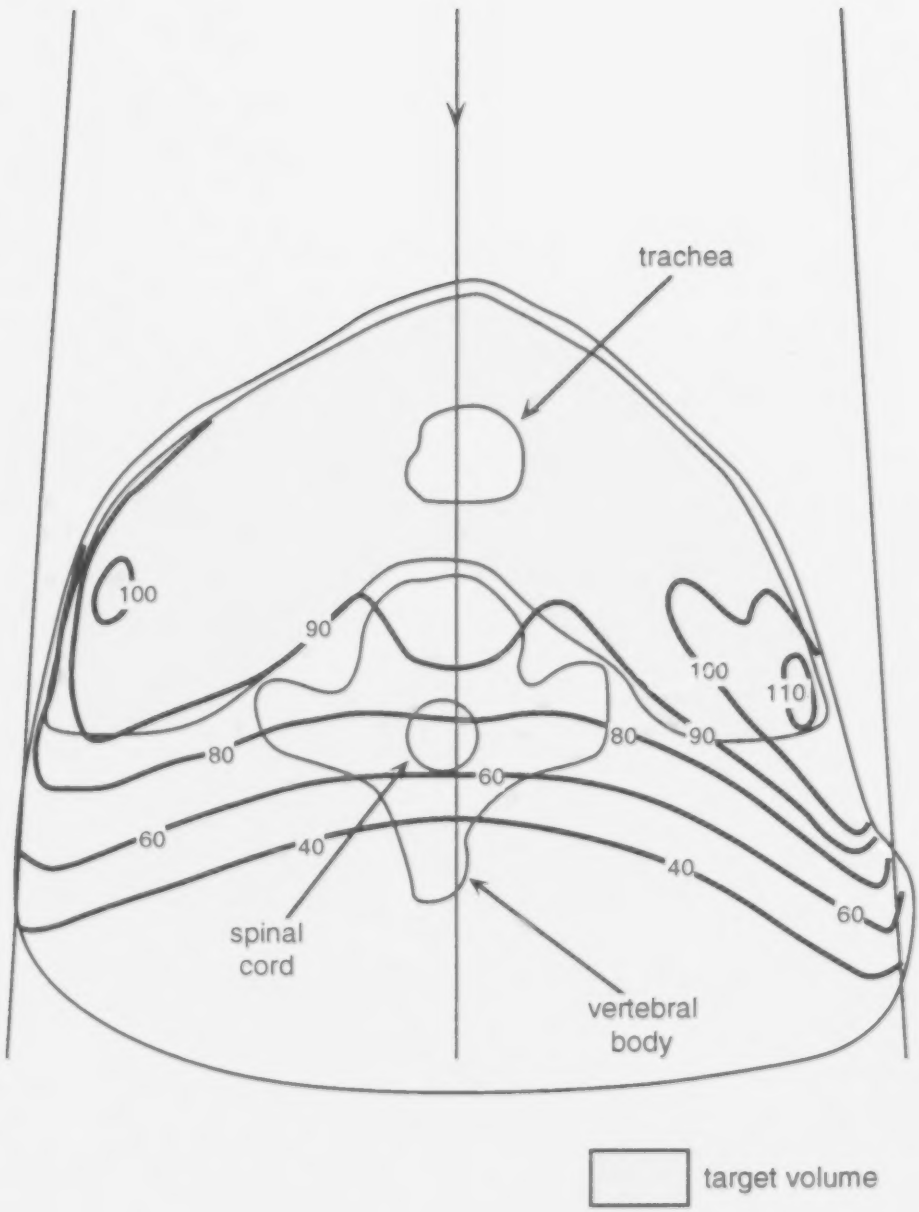

Figure III.26. Treatment plan for thyroid cancer, in the central plane with no bolus. Isodoses for an incident 16 MeV beam of electrons were calculated using the 3D MDAH pencil beam code.

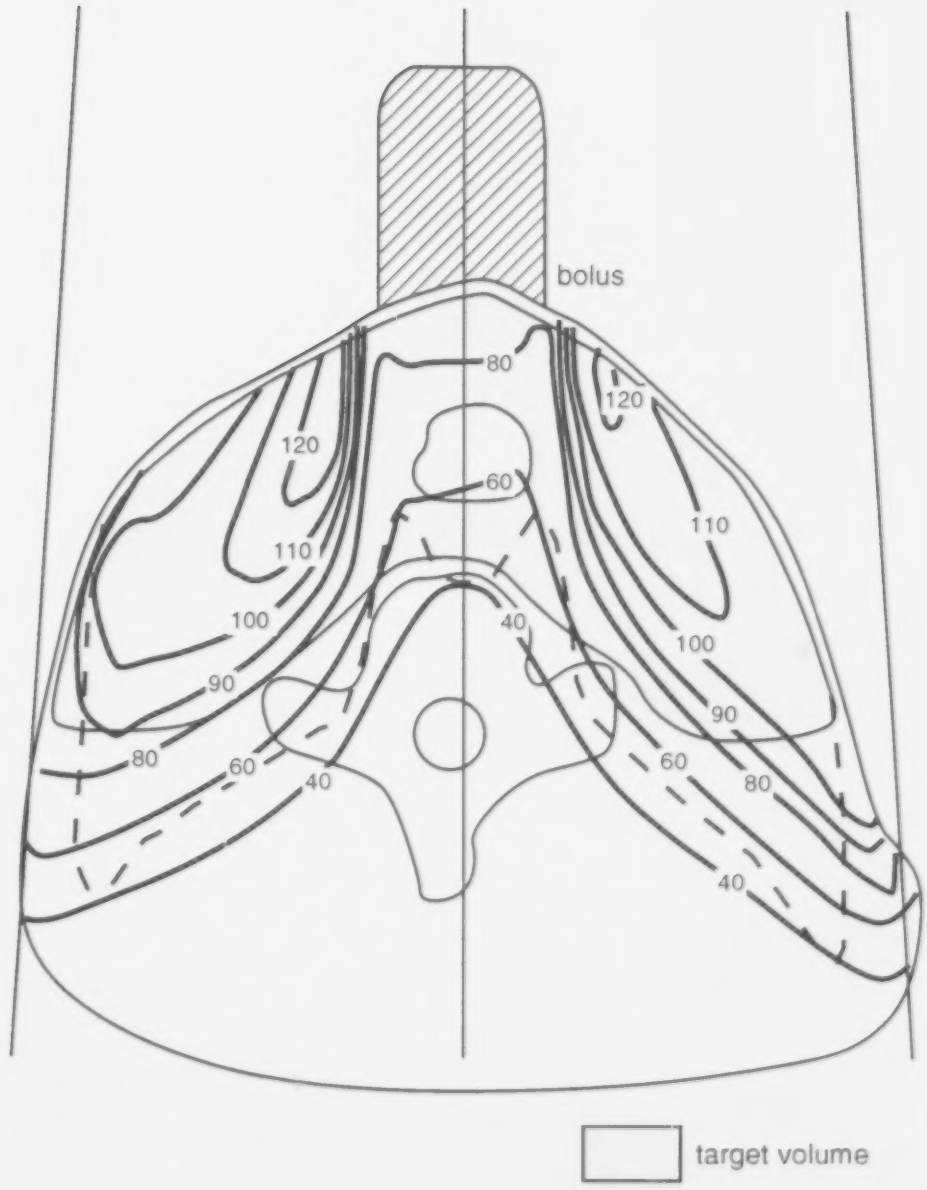

Figure III.27. Treatment plan for thyroid cancer, in the central plane with 'old' bolus. Isodoses for an incident 16 MeV beam of electrons were calculated using the 3D MDAH pencil beam code. The dashed line is the 80% isodose for a 2D calculation with no scatter correction (ray tracing model).

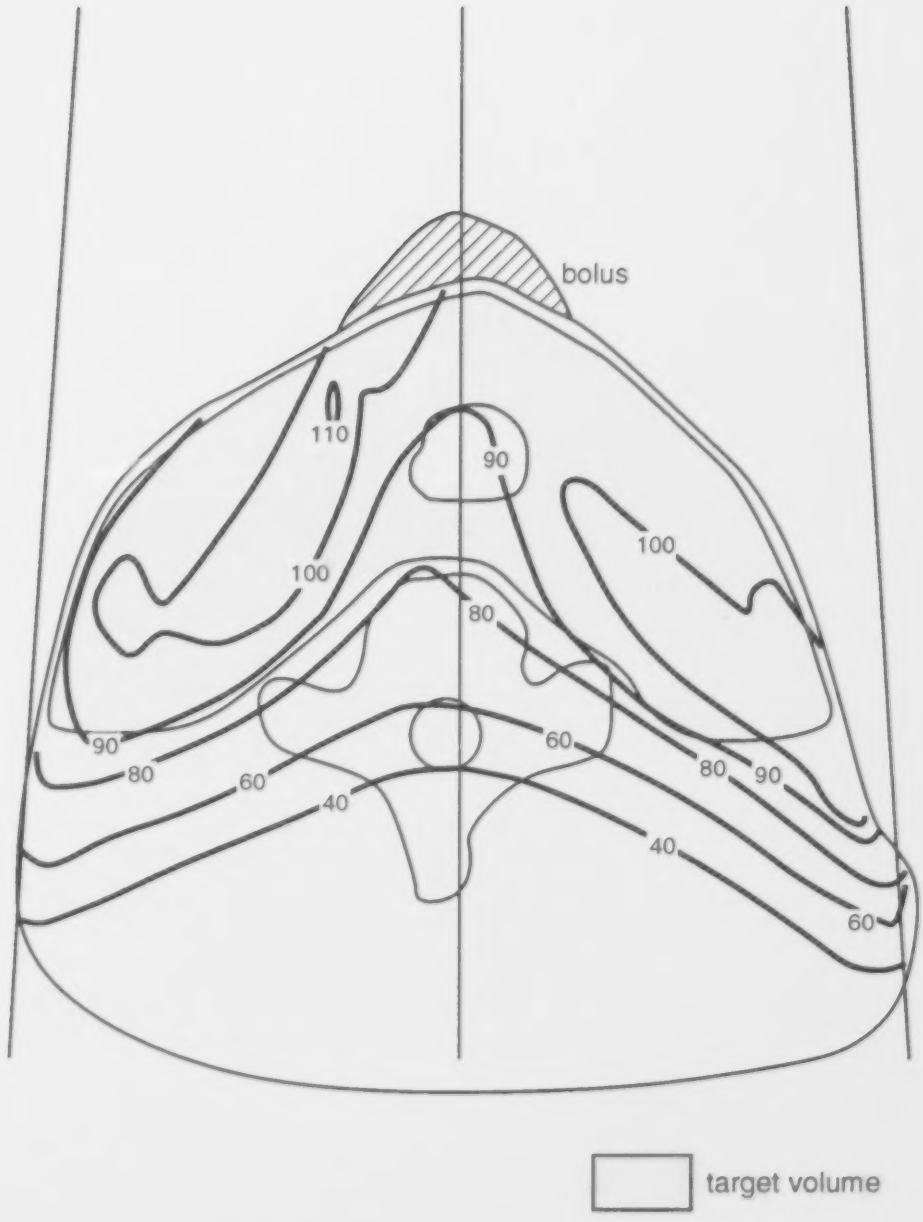

Figure III.28. Treatment plan for thyroid cancer, in the central plane with 'optimized' bolus. Isodoses for an incident 16 MeV beam of electrons were calculated using the 3D MDAH pencil beam code.

recalculating the beam. As a first step, the bolus was optimized in the central slice and two off-axis slices using a 2D implementation of the algorithm. The resulting bolus heights were plotted on a sagittal view of the patient. A good approximation of the final bolus could then be drawn on the sagittal view, and the bolus heights transferred to the corresponding CT slices. The 3-D calculation gave slightly different results, so small modifications of the bolus heights led to the final design shown in figure III.29. The height of the old bolus is shown for comparison.

To experimentally verify the new bolus design, a wax phantom was constructed using a duplicate of the patient immobilization shell. The trachea was modeled by a hollowed-out wax block, made according to trachea contours obtained from CT information of the patient. Thermoluminescent chips (LiF TLD-100) were placed at a depth of 5.7 cm below the bolus. Measurements were normalized to TLD measurements at d_{max} in a polystyrene phantom at the same SSD as the phantom without the bolus. Several CT slices of the wax phantom were obtained and calculations normalized to d_{max} in a water phantom at the same SSD as the phantom without the bolus. The results are shown in figure III.30. The measured data reveals a hot spot behind the trachea (on the central axis), which the calculation does not predict. In clinical situations where spinal cord tolerance is being approached, we should be aware that the current pencil beam algorithm may underpredict the dose to the spinal cord.

The failure of the calculation to predict the hot spot behind the trachea is due to the central axis approximation of the pencil beam algorithm, which assumes that each pencil beam is transported in a slab medium defined by the central axis of the pencil beam. At depth, the pencil beam has spread out appreciably, so the central axis approximation is not very good for the pencil beams near the lateral boundaries of the trachea. The dashed line in figure III.30 shows the effect on the calculated dose of filling in the trachea with wax, and we get essentially the same curve, except for the magnitude of the predicted dose along the

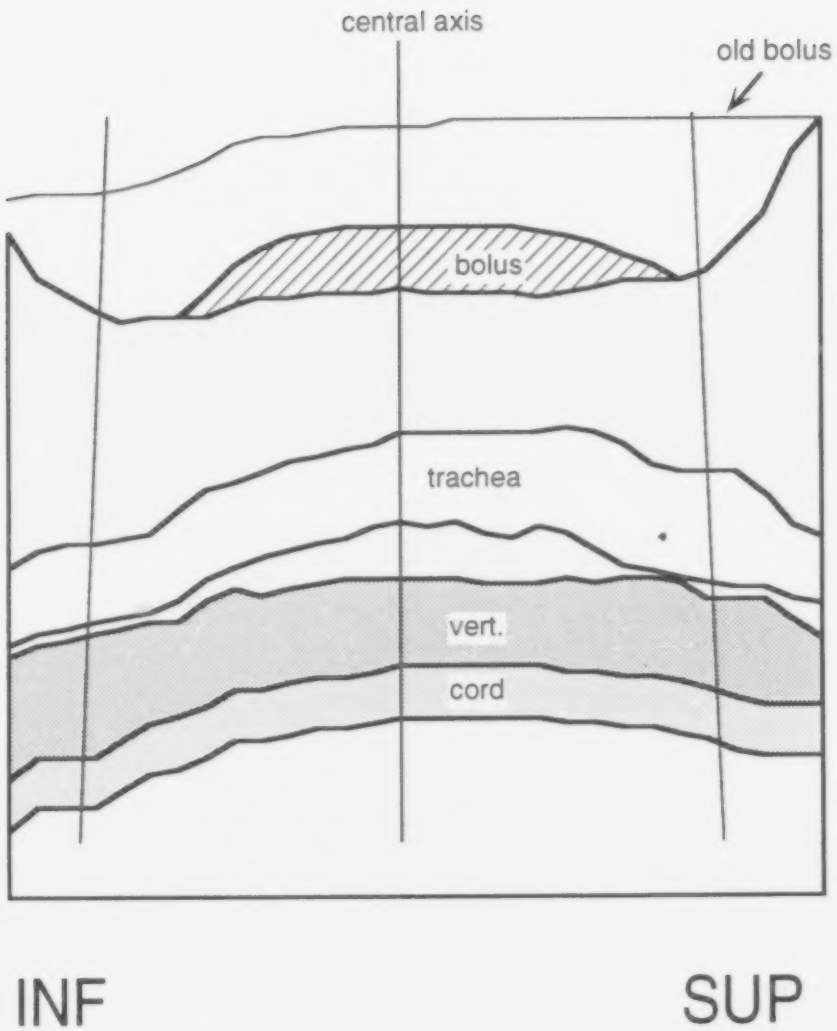

Figure III.29. Sagittal view of the optimized bolus contour. The old bolus contour is shown for comparison.

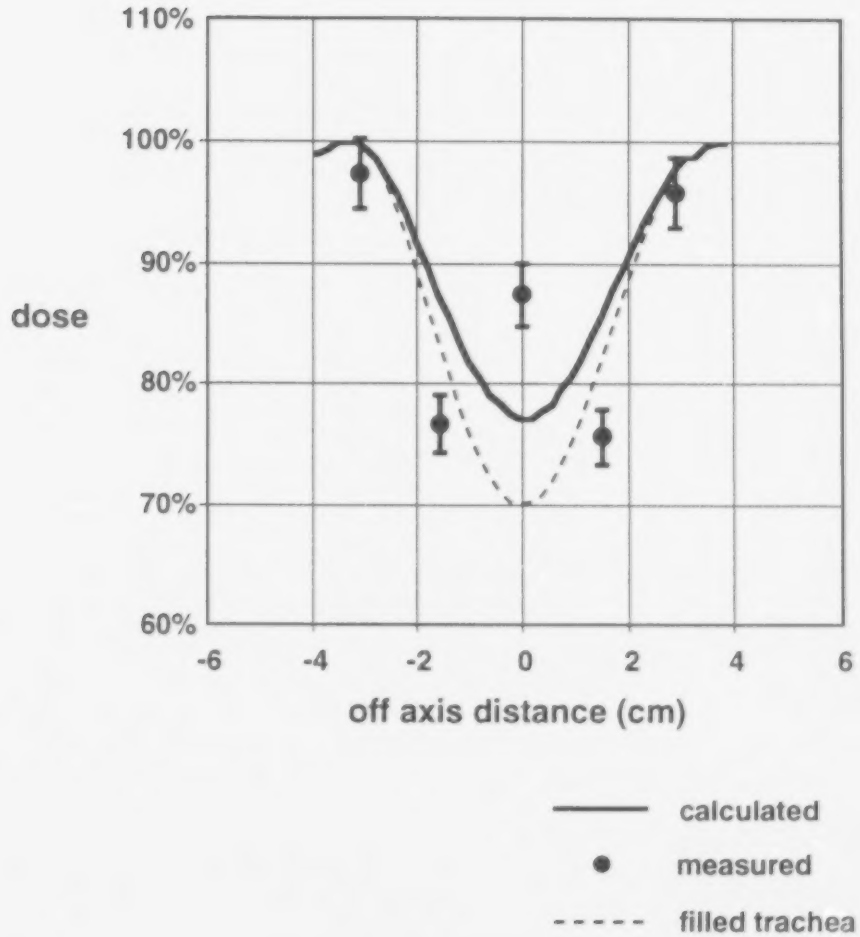

Figure III.30. Comparison of calculated dose profile at a depth of 5.7 cm under the bolus of figure III.28 (in a wax phantom), to point measurements (TLD-100 LiF chips) at the same depth. The dashed line is the calculated profile if the trachea is filled with wax.

central axis, which is reduced. The similarity in the two curves, indicate that at the depth of the calculation, the predicted dose profile is mainly a function of the patient contour.

3. Results and discussion

The main reason for the poor performance of the first bolus design is due to the ray model that was used to calculate the dose distribution, prior to the availability of the pencil beam algorithm. Since it is a ray model, the dose to a point depends only on what is directly between the source and the dose point. This completely ignores the fact that, at the depth of the vertebral body, most of the dose to that point actually comes from scattered electrons (Low *et al* 1992).

To illustrate this point, a Monte Carlo calculation was performed using the EGS4 code system (Nelson *et al* 1985) with the PRESTA step size algorithm (Bielajew and Rogers 1986) enabled. The standard DOSRZ user code† was used to simulate a semi-infinite water phantom. Dose was scored in cylindrical regions of 0.2 cm thickness and 0.1 cm radius, which is approximately the same volume as a dose voxel in the MDAH pencil beam algorithm. The water phantom was irradiated with a 5 cm radius beam of monodirectional, monenergetic 16 MeV electrons. The 'total dose' in figure III.31 is similar to the percentage depth dose for a clinical broad beam. The phantom was also irradiated with a 0.1 cm radius pencil beam, and this is the 'primary' dose in figure III.31*. As the depth increases, the dose due to electrons in the 'pencil beam' 'drops very rapidly compared to the 'total dose'. At the broad beam d_{max}, most of the dose is due to electrons scattered from outside the 0.1 cm radius 'pencil beam' entry point. This explains why the first bolus design technique performs so poorly. A one dimensional

---

† A cylindrical geometry allows the user to take advantage of symmetry and reciprocity to greatly reduce the CPU time needed for a given statistical accuracy.

* Reciprocity was used to do both simulations at once, to save CPU time.

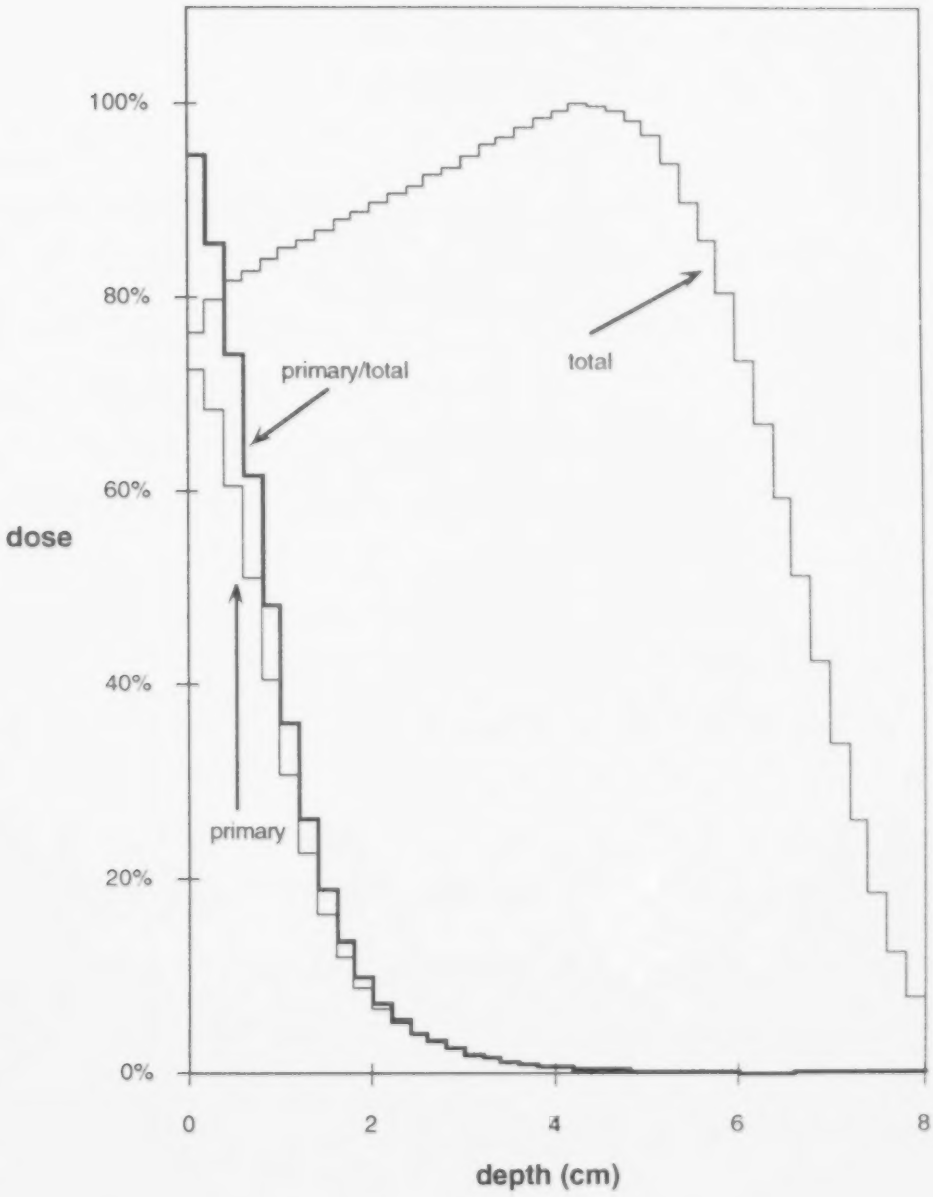

Figure III.31. Monte Carlo simulation of a central axis percentage depth dose for 16 MeV electrons, incident on a water phantom. The 'total' dose is from a 5 cm radius beam. The 'primary' dose is for a 0.1 cm radius beam. The ratio of primary to total dose is also shown.

heterogeneity correction does not consider scattered radiation and therefore predicts 100% primary dose.

The second approach to bolus design provides improvement since the calculation algorithm takes into account the scattered dose contribution to the dose voxel. However, designing the bolus is not so straightforward in this case. Iteratively reshaping the bolus and recalculating the dose distribution can be very time consuming. The most important thing to remember is that since almost all of the energy is deposited in the patient or bolus for electron treatments, the dose distribution must approximately conserve integral dose. This means that any change in the surface contour meant to increase dose in one area will decrease dose in an adjacent area (and vice-versa).

When designing bolus, it is also important to avoid vertical boundaries, such as in figure III.27, as they tend to produce small, very high dose regions. Notice that the hot spot below the edge of the bolus is reduced from 120% to 110%, from figure III.27 to figure III.28. This is a result of the lateral scatter non-equilibrium introduced by the vertical boundary. Fermi-Eyges based algorithms tend to underestimate the magnitude of these hot spots (Hogstrom and Almond 1983, Mah *et al* 1989).

In conclusion, bolus design based on rather limited assumptions about the nature of electron transport is not always reliable. The dose distributions that result from these assumptions may not fulfill the goals of treatment. Because of the large amount of scattered radiation in electron beams, it is very important that bolus design techniques take advantage of available pencil beam based algorithms.

D. Conclusion

This chapter has experimentally examined many aspects of electron pencil-beam dose calculation accuracy. Under many circumstances, the MDAH algorithm performs reasonably well. In some cases, the apparent discrepancy between calculation and

measurement may seem large, but the area (or volume) of the region affected is usually quite small. For clinical purposes, the algorithm is very useful, and is a good tool to use when planning electron beam treatments. In most cases, a simple ray tracing algorithm (no scatter correction) is inadequate for calculating the dose distribution. Since the MDAH and other pencil-beam algorithms calculate quickly using modern computer hardware, there is really no excuse for not regularly using a pencil-beam calculation algorithm for electron beam treatment planning.

With the ever increasing speed and reduced cost of computer hardware, the 3D version of the algorithm is also quite suitable in many clinical situations. There is a definite gain in calculational accuracy in some cases, which comes with only a slight speed penalty. The experiments presented above, show that the 3D algorithm is appropriate if the lateral extent of the heterogeneities is less than about 3-4 cm near the surface of the patient (or phantom). This also implies that to get the full benefit of the 3D pencil beam calculation, the anatomical information must be finer than 3-4 cm, so that the 3D algorithm gives different results than the 2D algorithm. A more practical upper limit would be perhaps 2 cm for the maximum CT slice separation, so that the 3D algorithm would give different results than the 2D version of the algorithm. Of course, to do 'true' 3D treatment planning, the slice separation should be approximately the same as the anatomical resolution in the plane of the CT slice, so that the anatomical resolution is the similar in all directions.

One shortfall of the MDAH algorithms is that they cannot accurately calculate small heterogeneities at large depths (compared to the practical range). This is because the pencil beams have spread out appreciably at depth. The redefinition algorithm (Shiu and Hogstrom 1987, 1991) overcomes this limitation, but with a large increase in computing time. For cases such as the thyroid treatment presented in this chapter, a 2D algorithm is probably quite sufficient. This implies that a 2D version of the redefinition algorithm could

be very clinically useful, if the 2D implementation had a large speed advantage over the 3D version of the code.

IV. Arc Electron Beams

A. Introduction

Because of increased capabilities in modern medical linear accelerators, there has been a renewed interest in the use of moving, or arced, electron beams, particularly for treating large lesions in the chest wall. The dosimetry of electron arcs is not as straightforward as for stationary electron beams. Some empirical methods of calculating the dose have been proposed (Leavitt *et al* 1985, Pla *et al* 1988, Pla *et al* 1989), but until recently, there has been no satisfactory method to incorporate heterogeneity corrections into the dose calculation. The pencil beam arc electron algorithm developed at M.D. Anderson Hospital (Hogstrom *et al* 1989) uses CT information for heterogeneity corrections in the same manner as the MDAH stationary beam algorithm (Hogstrom *et al* 1981), which performs reasonably well (Hogstrom *et al* 1984, Cygler *et al* 1987, Mah *et al* 1989). The pencil beam arc electron algorithm was therefore implemented into the Alberta Treatment Planning (ATP) system (Battista *et al* 1984).

B. Experimental Method

The pencil beam arc electron algorithm requires a relatively small amount of input data. This data was measured using a water tank scanning dosimetry system (Therados RFA-7) and transferred to the treatment planning system. A p-type diode was used as the dosimeter because of its good spatial resolution and the equivalence of ionization to dose (Rikner 1985). The reference field size was nominally 5×15 cm^2 at isocenter and the beam was produced by a computer controlled linear accelerator (Varian 2100C). The source to collimator distance (SCD) was approximately 45 cm and the source to isocenter distance (for electrons) was 90 cm. The water tank was placed at a source to surface distance (SSD) of 72.5 cm for the reference data measurements. The reference setup is shown schematically in figure IV.1. Accurate data entry was verified by calculating the dose

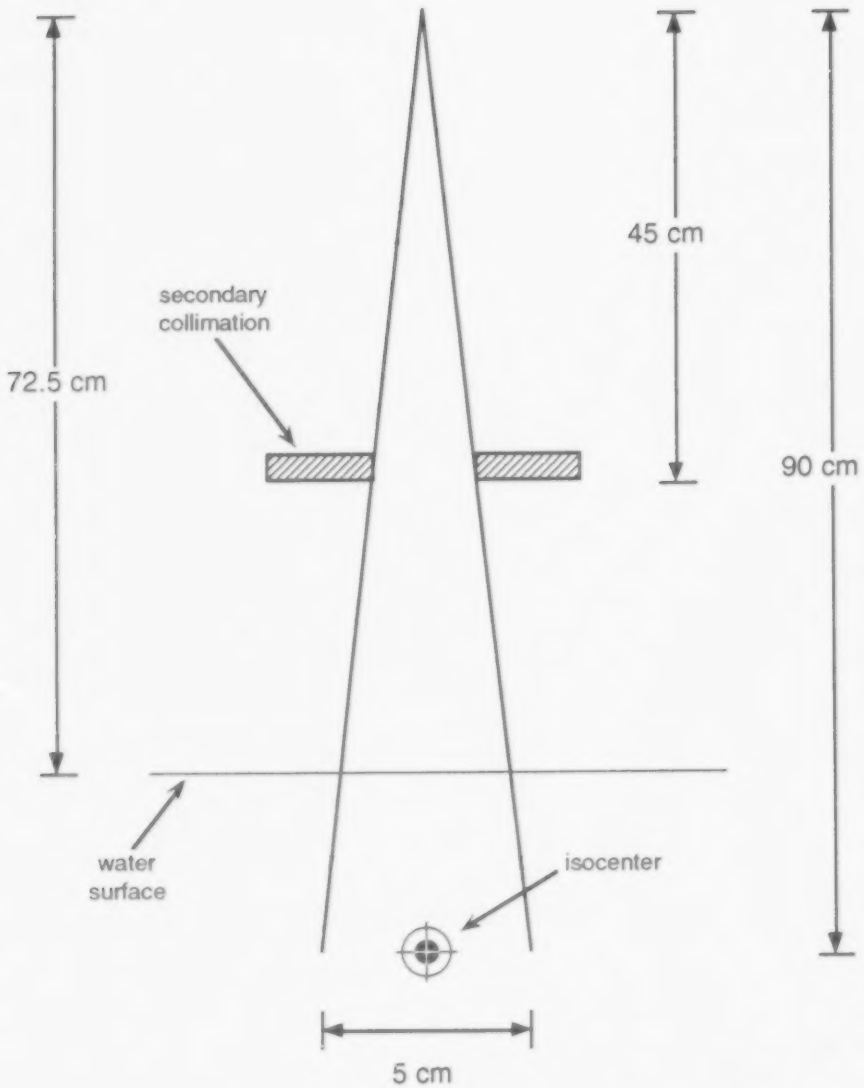

Figure IV.1. Schematic diagram of the reference beam setup for arc electron beams. Note that the horizontal and vertical scales are not identical.

distribution for a 0° arc (stationary beam with arc electron collimator) on a flat water phantom under reference conditions.

Two types of phantom were used for the arc measurements. The first phantom, shown in figure IV.2, consisted of cylindrical polystyrene slabs, with a radius of 17.5 cm. Bare Kodak XV film was sandwiched between the slabs and electrical tape was used to protect the film from ambient light. The phantom was placed in the beam with the phantom axis along the axis of gantry rotation. Data was obtained for arcs of 0°, 90°, and 145° for nominal beam energies of 12 and 20 MeV. For the purposes of this study the field size was not varied, and was the same as the reference field size. The films were scanned using an automated film densitometer system (Therados RFA-7). The data was converted to dose using a measured optical density to dose conversion curve.

Measurements were also performed in a water phantom, figure IV.3, for the same arc angles as for the film measurements. The phantom was constructed by vacuum forming 0.3 cm thermoplastic sheet (Vivak™) over a semicircular mould, so that the outside radius of the phantom was 17.5 cm as for the polystyrene phantom. The final wall thickness was 0.15 cm. This was bolted to a plexiglass water phantom with a large opening at the top for filling with water and dosimeter access. A diode was mounted on a one dimensional scanner (Therados LSC-2) which in turn was mounted onto the water tank. An integrating electrometer (Therados DPD-5) was used to measure the arc electron dose. The measurement procedure consisted of positioning the diode at the point of interest, resetting the electrometer, and initiating the arced electron beam. Reproducibility of the electrometer measurement was excellent (< 0.5%) partly because of the stability of the linear accelerator. There is also a small uncertainty in position, which can be converted to an uncertainty in dose using the gradient of the dose distribution at that point.

For both film and diode measurements, the data was normalized to the maximum dose along the central axis for the reference field (0° arc) on a flat water or polystyrene

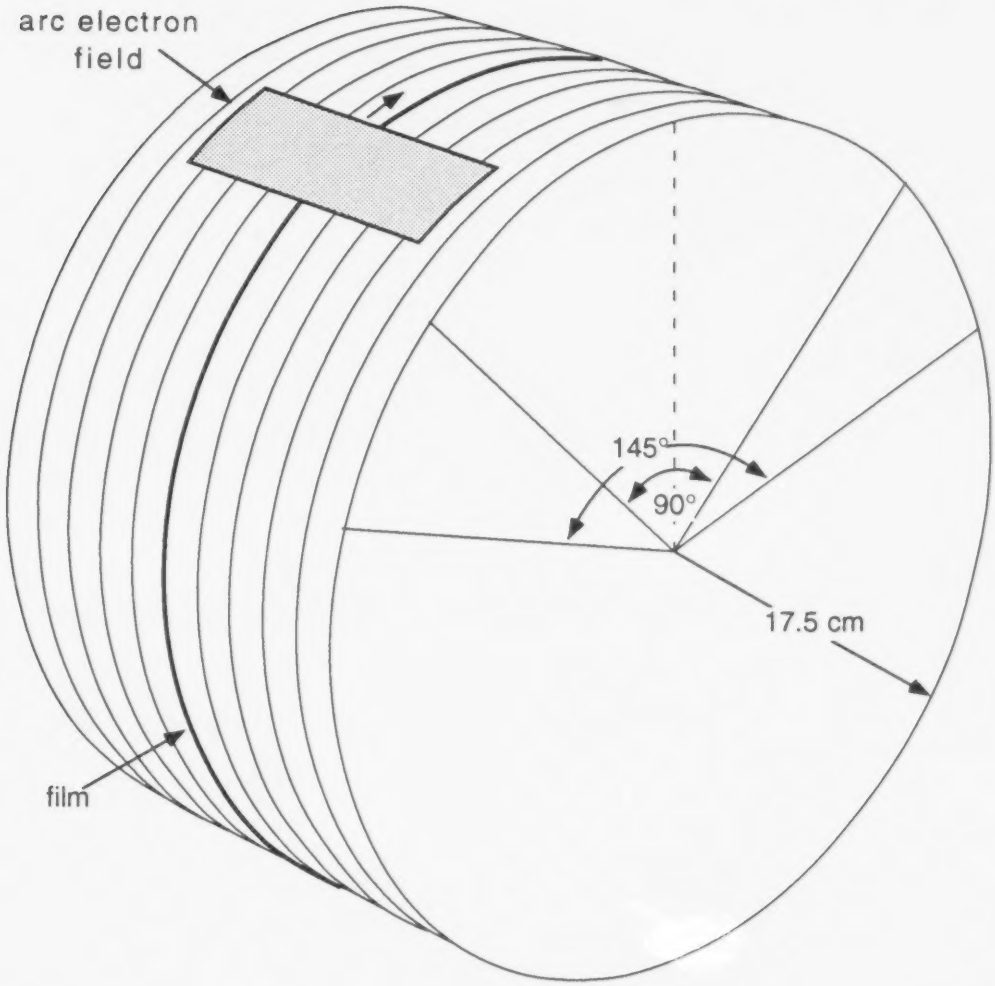

Figure IV.2. Schematic diagram of the polystyrene phantom used for film measurements in arc electron beams. The slabs are approximately 2 cm thick.

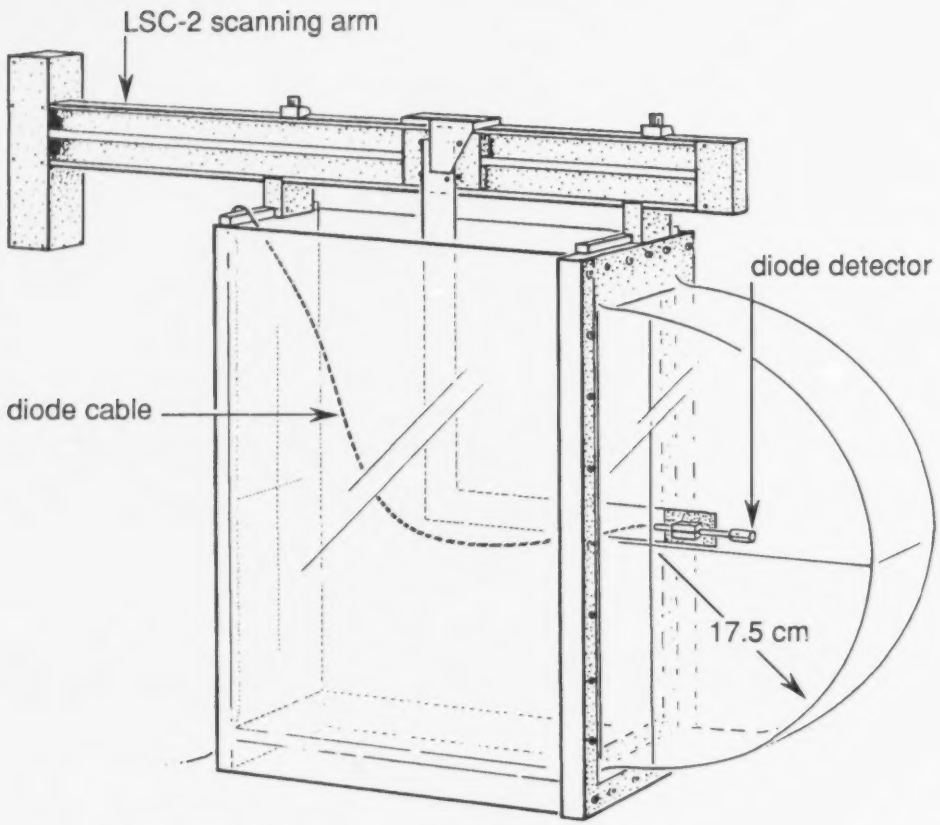

Figure IV.3. Schematic diagram of the water phantom used for measurements in arc electron beams.

phantom at a source to surface distance of 72.5 cm, taking into account any difference in the number of monitor units (MU) needed to obtain sufficient dosimeter response. This gives the dose per monitor unit as a percentage of the dose per monitor unit for the reference field. This is consistent with the normalization used by the arc electron calculation algorithm, so the data can be compared directly.

C. Homogeneous Phantom

Figure IV.4 shows calculated and measured depth doses for 0° arcs on the cylindrical phantoms of figures IV.2 and IV.3. Because the radius of curvature of the phantoms is large and the source to surface distance (SSD) was the same as the reference setup in figure IV.1, we expect that the calculation and measurement should more or less reproduce the reference data measured with the flat water phantom. Therefore, the calculated and measured maximum depth doses should all be close to 100%, which is seen in figure IV.4. The only general observation is that the calculated range is slightly greater than the measured range, but the difference is small enough to be clinically insignificant.

The percent depth dose for a 6 MeV, 90° arc is shown in figure IV.5. The depth dose was measured along the symmetry axis of the arc, as in all subsequent depth dose figures. The depth doses match reasonably well, with the calculated maximum dose approximately 1% lower than the measured dose†. We feel that this is a result of the relative coarseness of the calculational grid compared to the sharpness of the dose peak in the measured depth dose data.

Figures IV.6 and IV.7 show the depth dose for 12 MeV beams with arcs of 90° and 145° respectively. In both figures, the calculated and measured maxima match quite

---

† All differences are given as a percentage of the dose per machine unit for the reference field. This is simply the arithmetic difference of the dose values with the default normalization used by the MDAH algorithm.

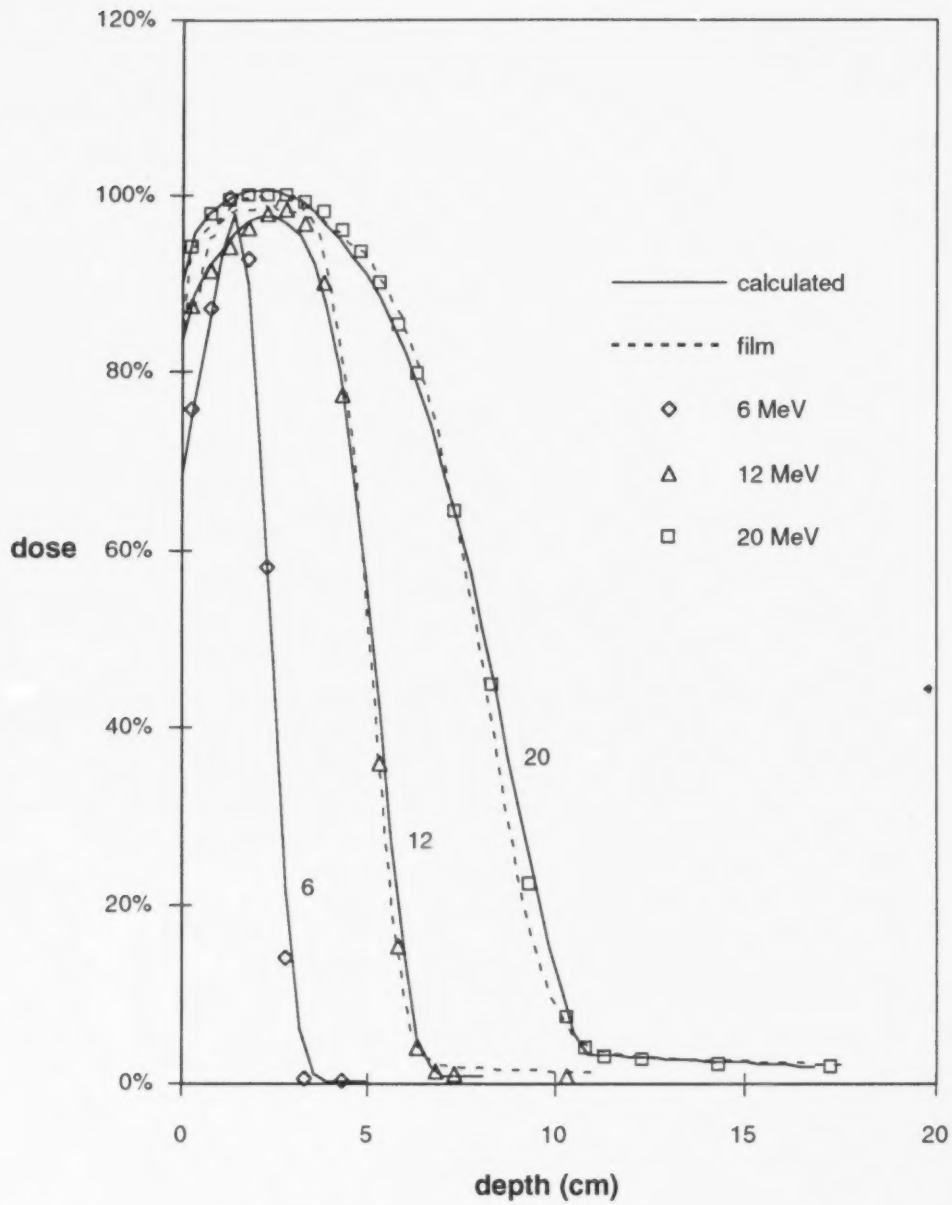

Figure IV.4. Percentage depth doses for 0° arcs on a 17.5 cm radius water (or polystyrene) phantom, for nominal energies of 6, 12, and 20 MeV. The source to surface distance was 72.5 cm, the same as for the reference field. The solid lines are calculated data; the dashed lines are measured with film in polystyrene; the discrete points are diode measurements in a water phantom.

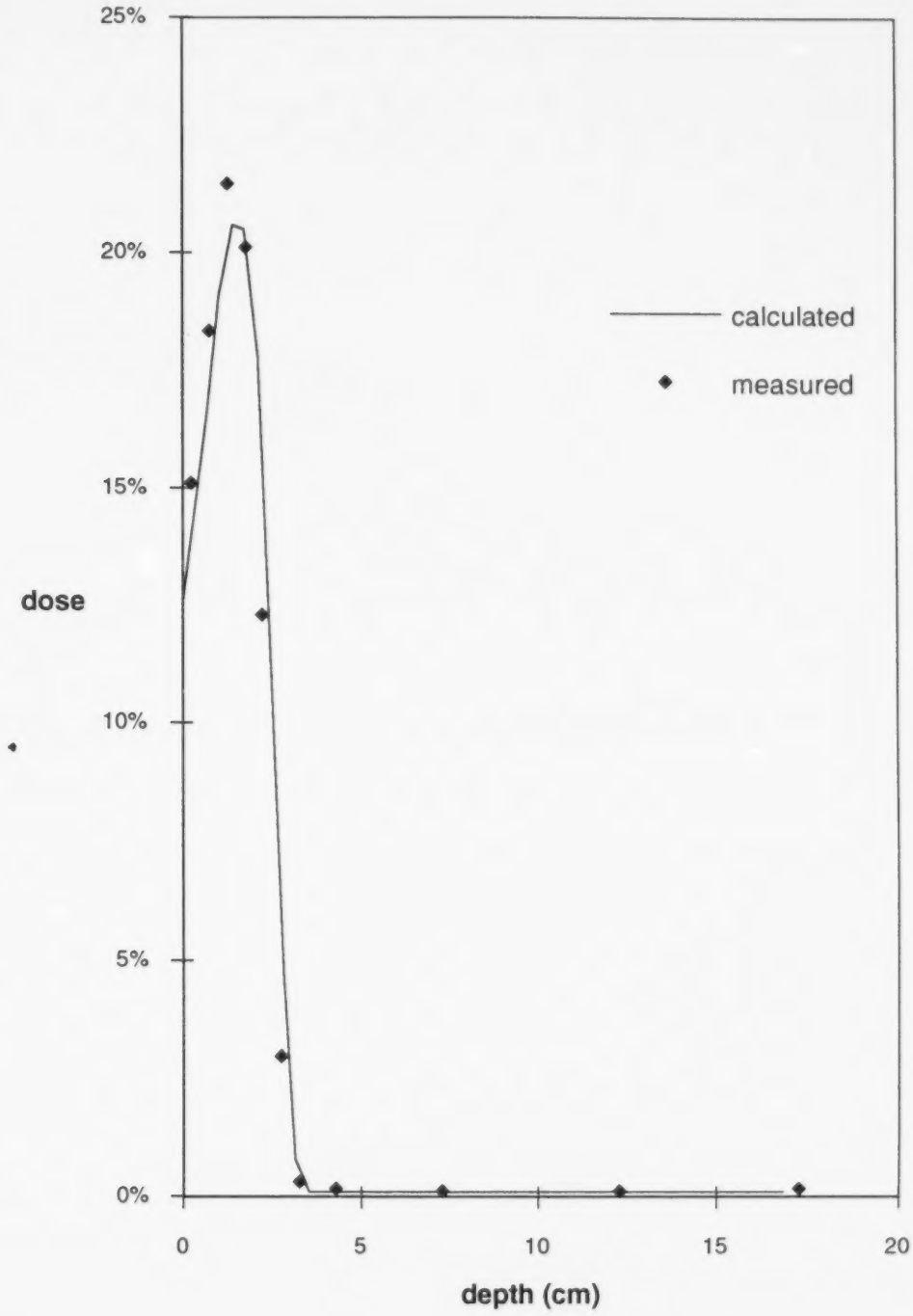

Figure IV.5. Mid-arc percentage depth dose for a 6 MeV 90° arc on a 17.5 cm radius phantom. The solid line is calculated using the MDAH arc electron pencil beam algorithm and the discrete points are measured with a diode in a water phantom.

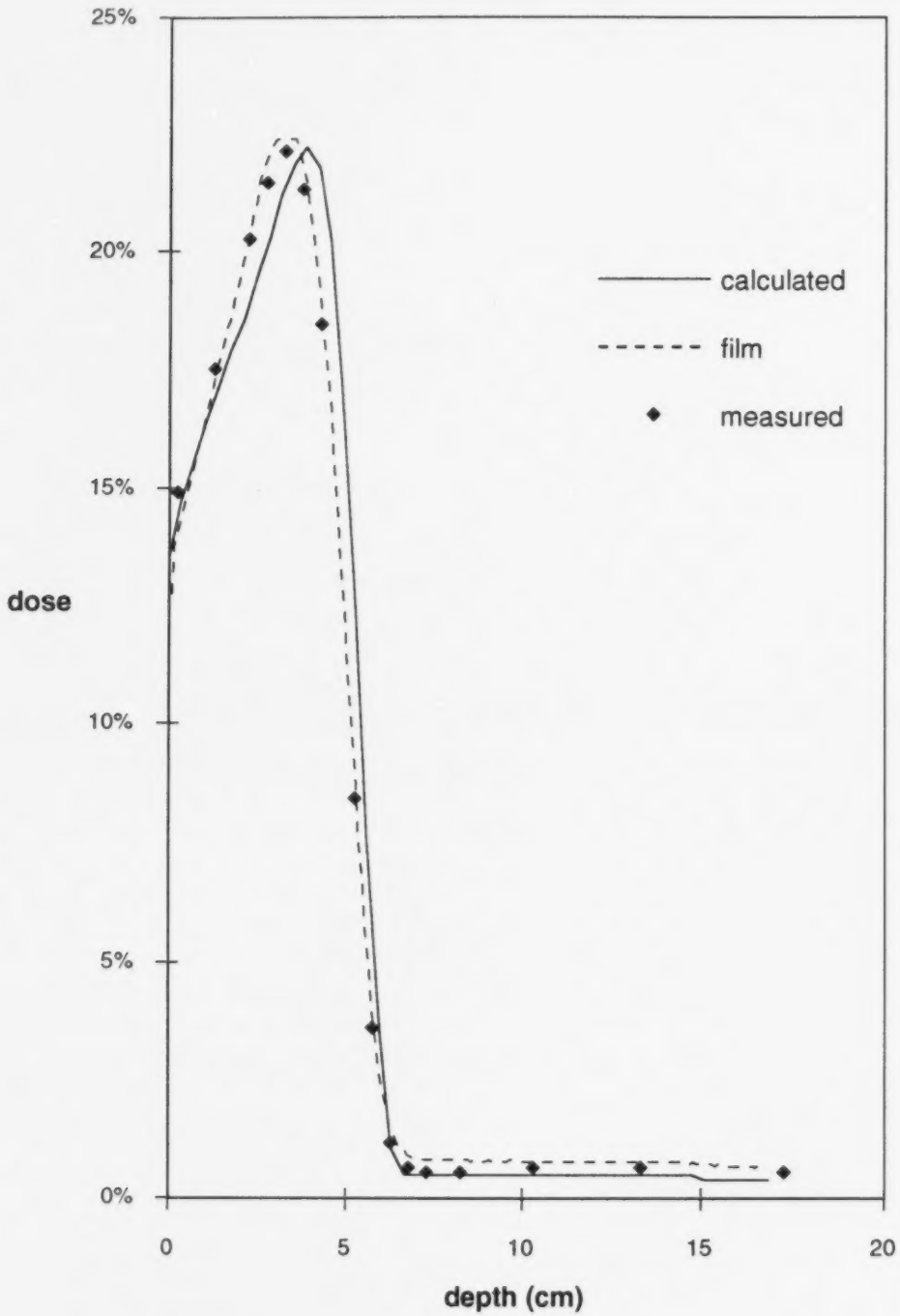

Figure IV.6. Mid-arc percentage depth dose for a 12 MeV 90° arc on a 17.5 cm radius phantom. The solid line is calculated using the MDAH arc electron pencil beam algorithm, the dashed line is measured with film in a polystyrene phantom, and the discrete points are measured with a diode in a water phantom.

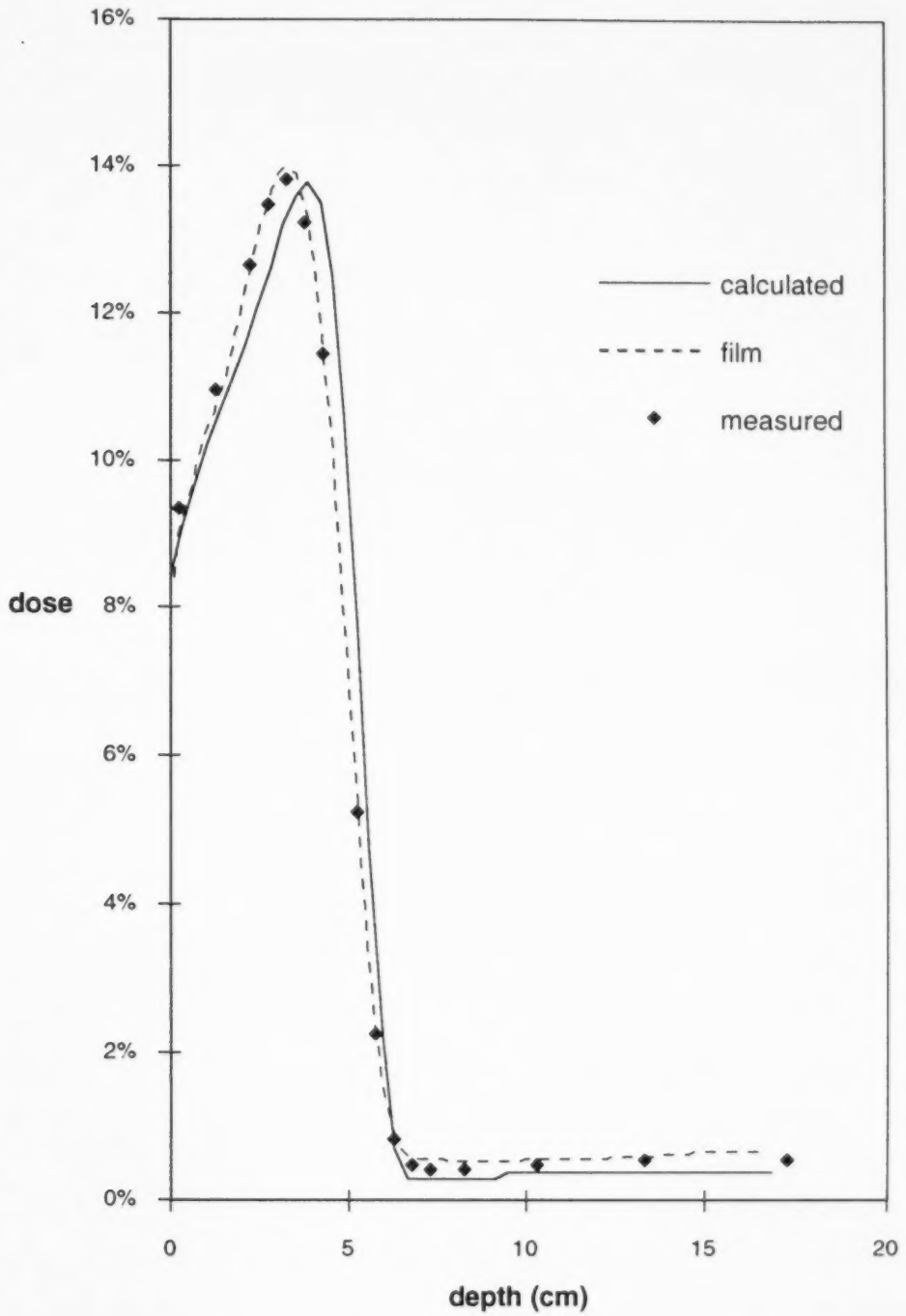

Figure IV.7. Mid-arc percentage depth dose for a 12 MeV 145° arc on a 17.5 cm radius phantom. The solid line is calculated using the MDAH arc electron pencil beam algorithm, the dashed line is measured with film in a polystyrene phantom, and the discrete points are measured with a diode in a water phantom.

well, with the calculated depth of maximum dose being about 0.5 cm deeper than the measured depth of maximum dose. The ranges, however, are almost identical. Another thing to notice about the two figures is that shape of the curves is almost identical. This is because the extra 55° of electron arc from figure IV.6 to figure IV.7 contributes negligible dose along the symmetry axis. The only result is to lower the dose maximum relative to the total number of monitor units given. At a greater depth, the situation is slightly different, because the isocenter is in the electron beam at all times. Therefore the dose at isocenter is the same regardless of the angle of the arc and in this case, the isocenter dose is 0.5%.

The other feature to notice about figure IV.6 and IV.7 is that the film measurements follow the diode measurements very closely. In order for this to occur, many precautions had to be taken. Because the data is normalized to a flat phantom, the data in figure requires three films. An unirradiated film is processed to give a 0% level, and another film is irradiated under reference conditions to establish a 100% level. We can then measure the arc dose data, accounting for film non-linearity and the difference in monitor units required for adequate film blackening. The individual film measurements can be quite tricky themselves, because misalignment of the film and air gaps can easily affect the results (Dutreix and Dutreix 1969). In order to normalize the film data in the same manner as the MDAH arc electron algorithm, two film measurements were needed. Obtaining good results was therefore even more difficult, because small differences in processing conditions can also affect the measured optical density (ICRU 1984a). There was some hesitation in using the absolute dose given by the film measurements, so the water phantom was constructed to ensure confidence in the measured data.

Figures IV.8 and IV.9 show the results for 90° arcs of 16 MeV and 20 MeV electrons. The observations to be made are very similar to those at 12 MeV, with the calculated depth of maximum dose slightly greater than the measured depth of maximum dose. The ranges and bremsstrahlung components match very well. Overall, the agreement

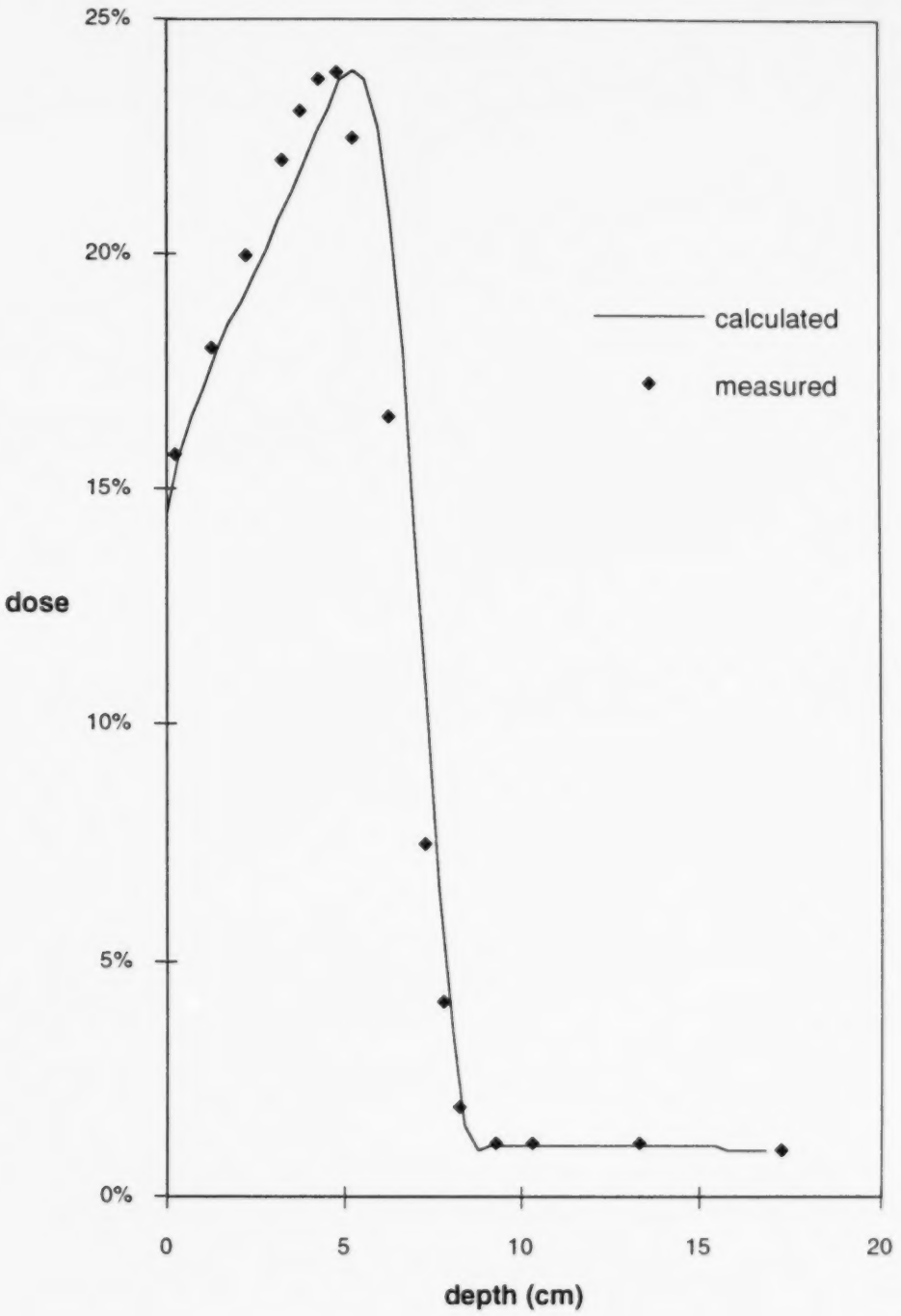

Figure IV.8. Mid-arc percentage depth dose for a 16 MeV 90° arc on a 17.5 cm radius phantom. The solid line is calculated using the MDAH arc electron pencil beam algorithm and the discrete points are measured with a diode in a water phantom.

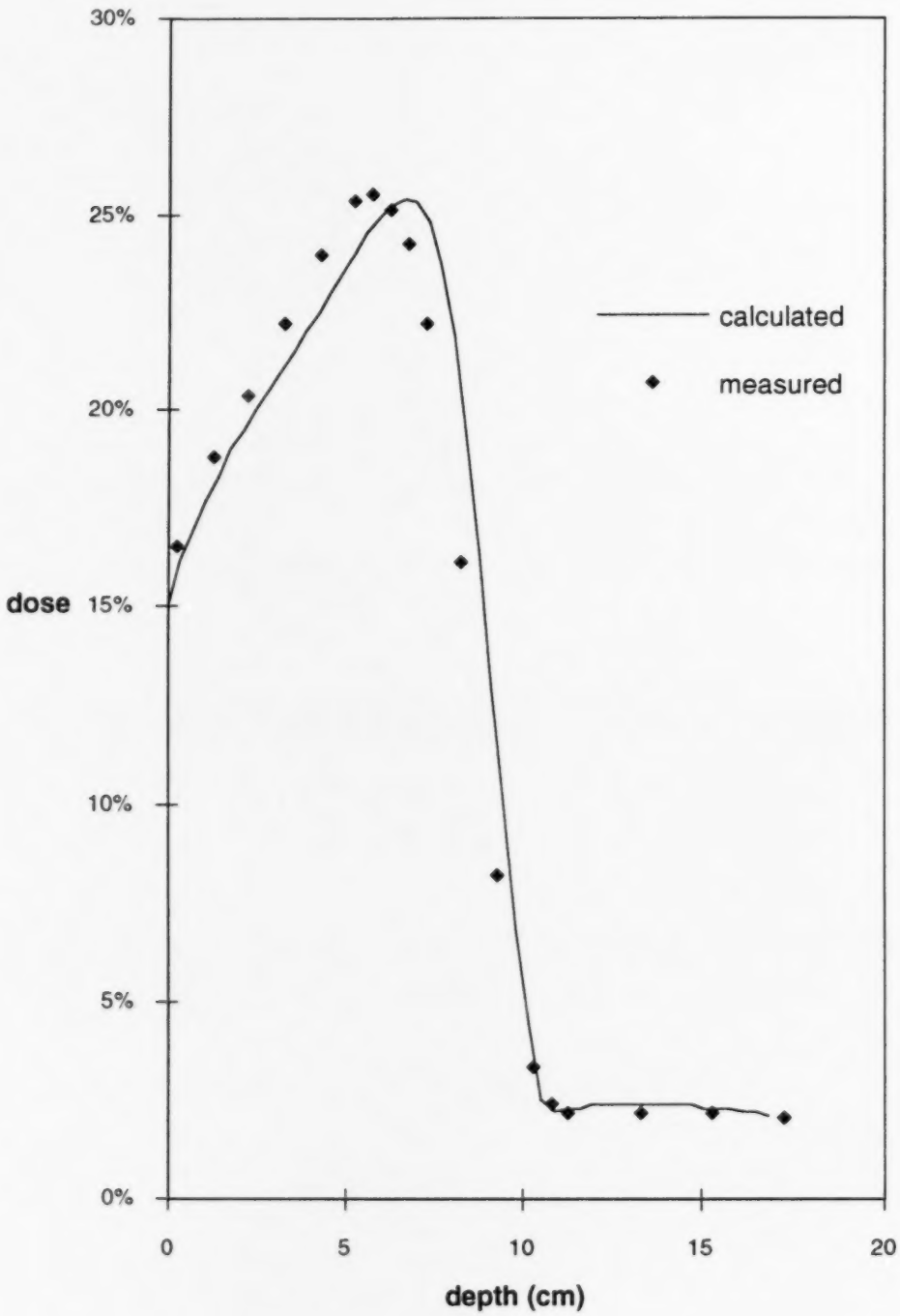

Figure IV.9. Mid-arc percentage depth dose for a 20 MeV 90° arc on a 17.5 cm radius phantom. The solid line is calculated using the MDAH arc electron pencil beam algorithm and the discrete points are measured with a diode in a water phantom.

between measurement and calculation for all of the energies is quite good. Figure IV.10 shows measured and calculated isodoses for the 12 MeV, 90° arc, at the edge of the arc. All of the above data confirms that the algorithm is working as it should, and is similar to data measured elsewhere (Kurup *et al* 1992).

D. Lung Phantom

Electron arc therapy is frequently used for chest wall irradiation, so that a large area of the chest wall can be treated uniformly. For any chest wall treatment, the lung is a major critical organ, and is particularly sensitive to radiation damage (Hall 1988). To test the accuracy of algorithm for chest wall treatments, the lung phantom, shown in figure IV.11, was constructed. The 'lungs' were constructed from semicircular segments of cork, approximately 15 cm thick, and bolted into the water phantom. The cork was wrapped in thin plastic 'cling' wrap, to ensure that the cork did not soak up water and therefore change density, during the experiments. The vertical distance from the axis of symmetry, or isocenter, to the cork was 5.5 cm, and the 'chest wall' thickness was 2 cm. The phantom was filled with water, and a diode was used to measure the dose, as before. The dose was measured along along lines 5 cm above isocenter, and 2.5 cm above isocenter, for energies of 12, 16, and 20 MeV. The beam was arced over an angle of 80° from a horizontal position to 10° from vertical, as shown in figure IV.11.

Figure IV.12 show the results for a 12 MeV arc. The continuous lines show the calculated dose along the scan lines and the discrete points are measured values. The position coordinate is measured from isocenter in this case. For the scan nearest the cork (y=5), the calculation overpredicts the dose in the central part of the curve by approximately 3%, or 10% of the maximum dose for the treatment plan, which was approximately 34% of the stationary beam reference output. This overprediction is consistent with the generally deeper penetration of the depth dose for the homogeneous water phantom. For the deeper scan line (y=2.5), the main discrepancy is between 7–10 cm from isocenter, where the

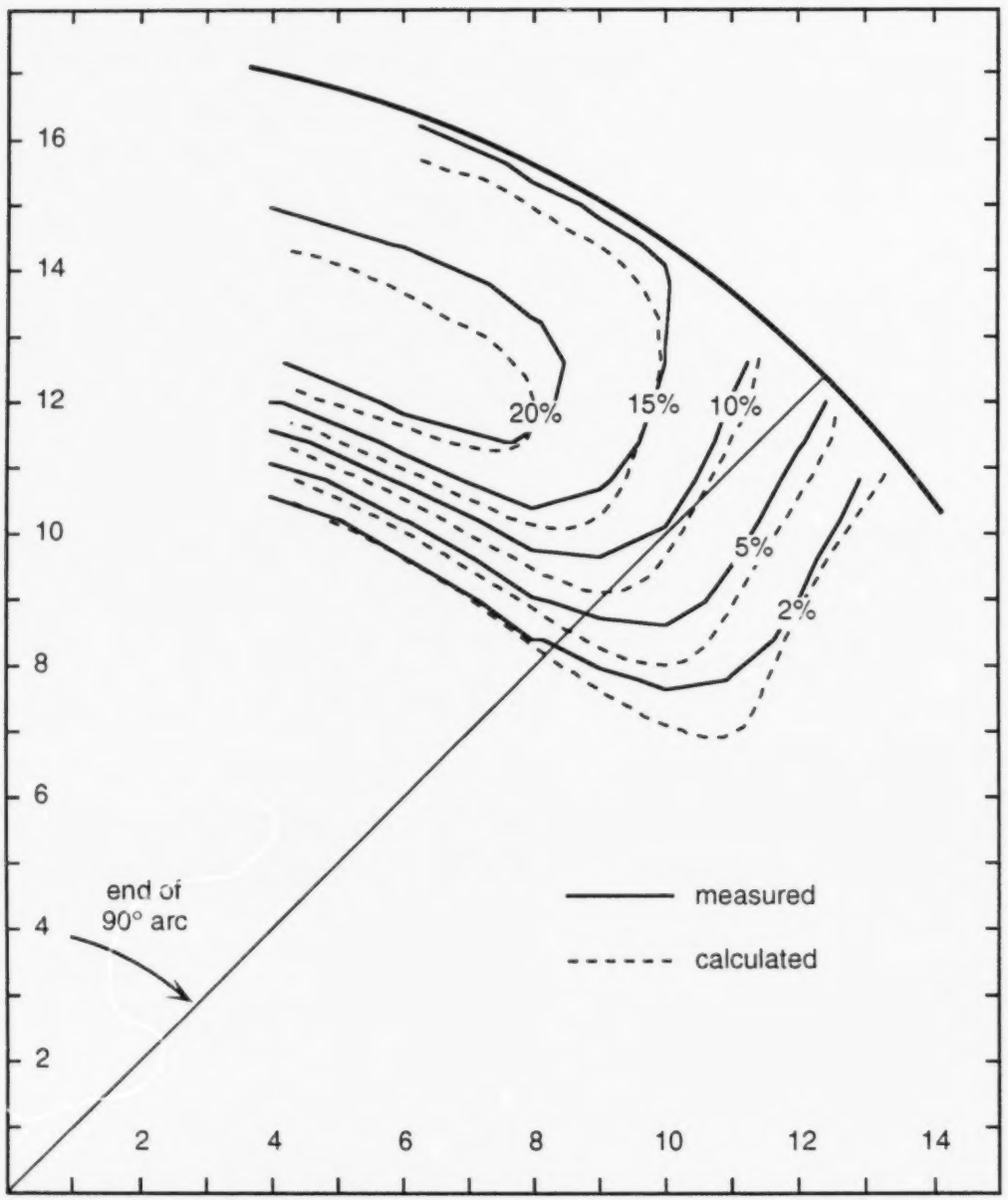

Figure IV.10. Calculated and measured (film) isodose lines for a 90° arc of 12 MeV electrons incident on a 17.5 cm radius polystyrene phantom.

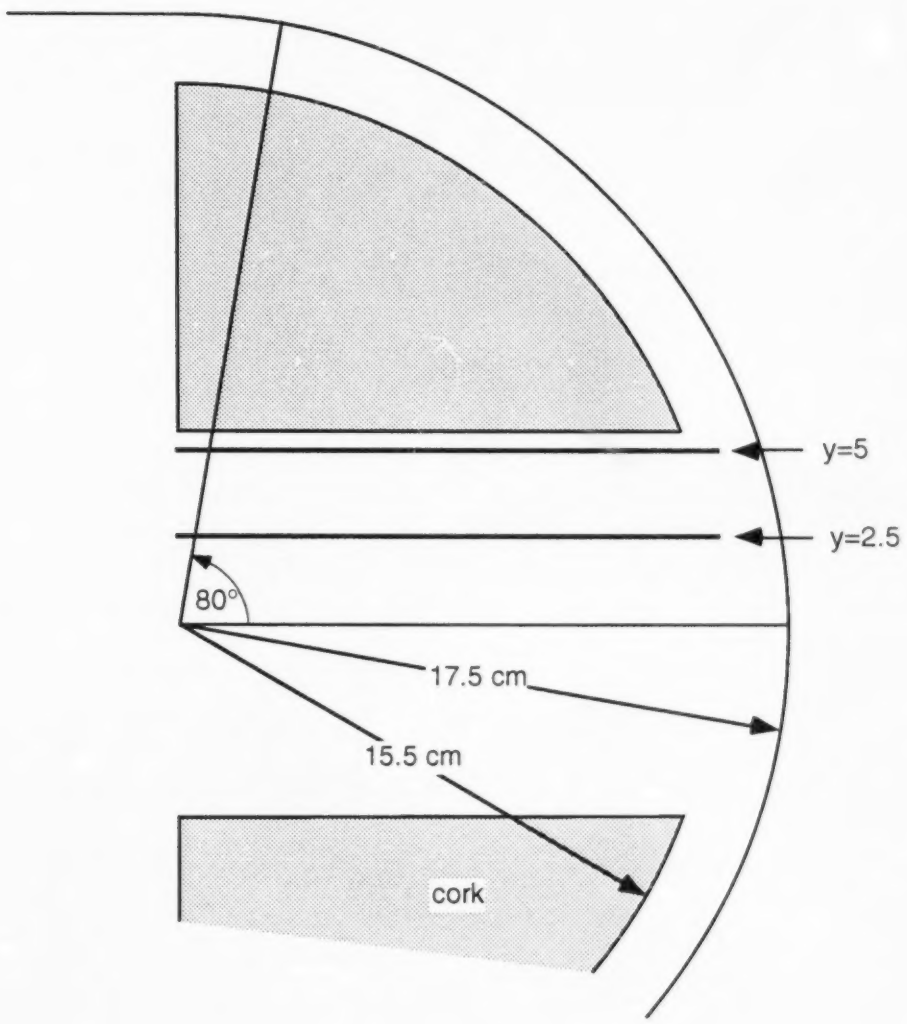

Figure IV.11. Schematic representation of the lung phantom geometry. The pieces of cork were fastened into the water phantom in figure IV.3.

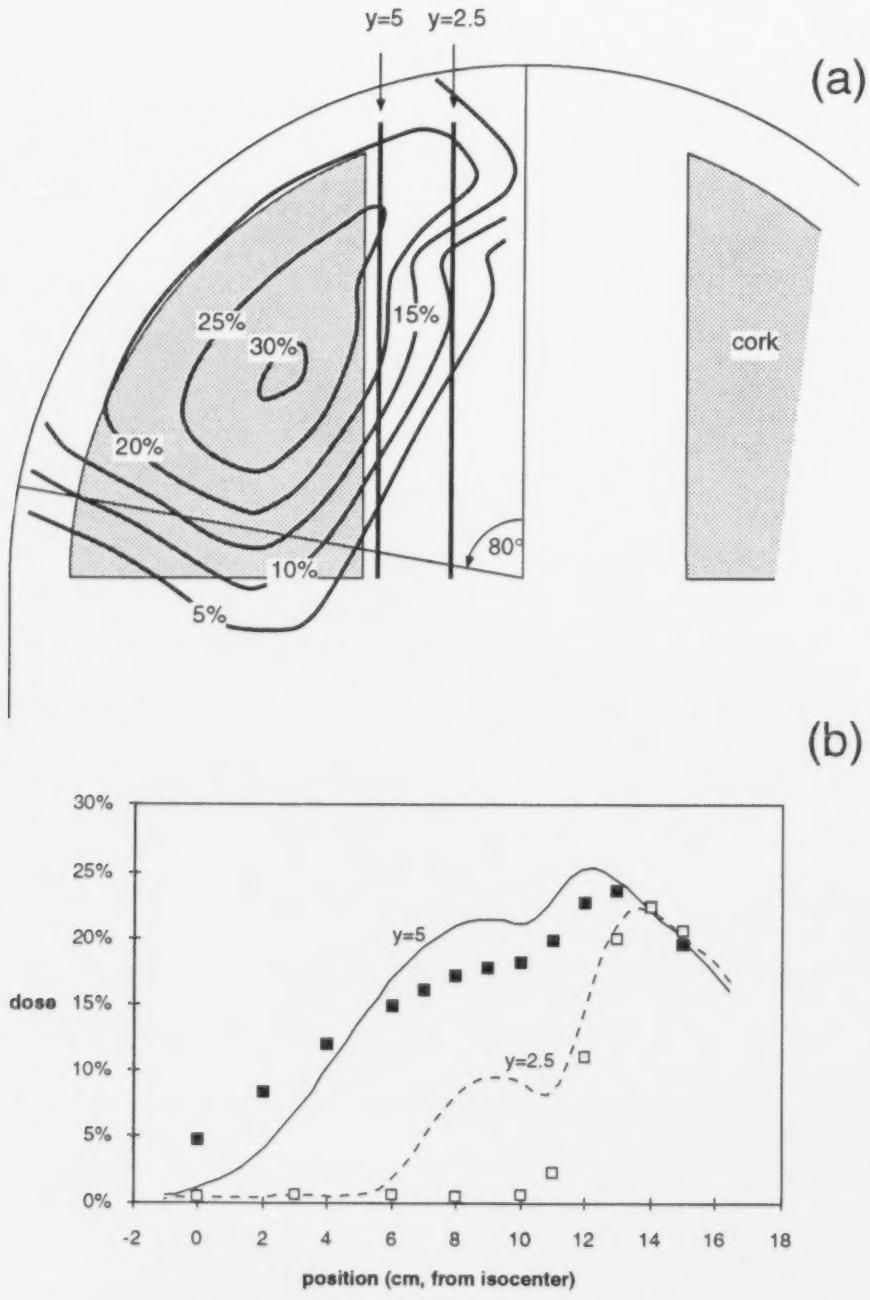

Figure IV.12. Calculated and measured doses profiles for a 12 MeV, 80° arc incident on the lung phantom in figure IV.11. Calculated isodoses are shown in (a). The solid and dashed lines (b) are calculated profiles at y=5 and y=2.5, respectively. The solid and open points are measured doses along the same profiles.

calculated dose is approximately 9%, but the measured dose is already in the bremsstrahlung region, less than 1%. This is greater than the experimental error, but should not be clinically significant since the algorithm is overpredicting the dose. Of more clinical significance is the dose to the chest wall, but from our water phantom measurements, we can be confident that the given dose is accurate.

Figure IV.13 show the data for the same phantom as figure IV.12, but with an energy of 16 MeV. Qualitatively, the results are very similar, with slightly better accuracy (≈2%) for the scan line nearer the cork. Figure IV.14 show the results for the 20 MeV beam, and again the calculated dose is fairly close to the measured dose.

Overall, figures IV.12 through IV.14 show that the MDAH arc electron pencil beam algorithm works reasonably well for our lung phantom. We can be confident that the lung dose predicted by the algorithm will be close to (or greater than) that actually delivered. Calculation of the dose to heterogeneities is a major advantage of this algorithm over other algorithms (Leavitt *et al* 1985, Pla *et al* 1988) and should prove clinically useful.

E. Discussion

Even though the agreement between measurement and calculation is quite good, there are a few precautions that must be taken in order to assure good calculational results. If we consider, for the moment, a cylindrically symmetric irradiation geometry, as in figures IV.2 and IV.3, then the dose distribution within the phantom can be written as

$$D(r,\theta) = \int_0^{2\pi} S(\alpha)\, d(r,\theta-\alpha)\, d\alpha \qquad \text{(IV.1)}$$

where $D(r,\theta)$ is the dose distribution in polar coordinates, $S(\alpha)$ is a source function describing the output of the linear accelerator as a function of angle, and $d(r,\theta)$ is the dose distribution for a stationary beam on the same phantom at α=0. Equation (IV.1) gives the total dose distribution as an integral of dose distributions from a moving beam. Conversely, we can get the same result if we consider the beam as being stationary and the

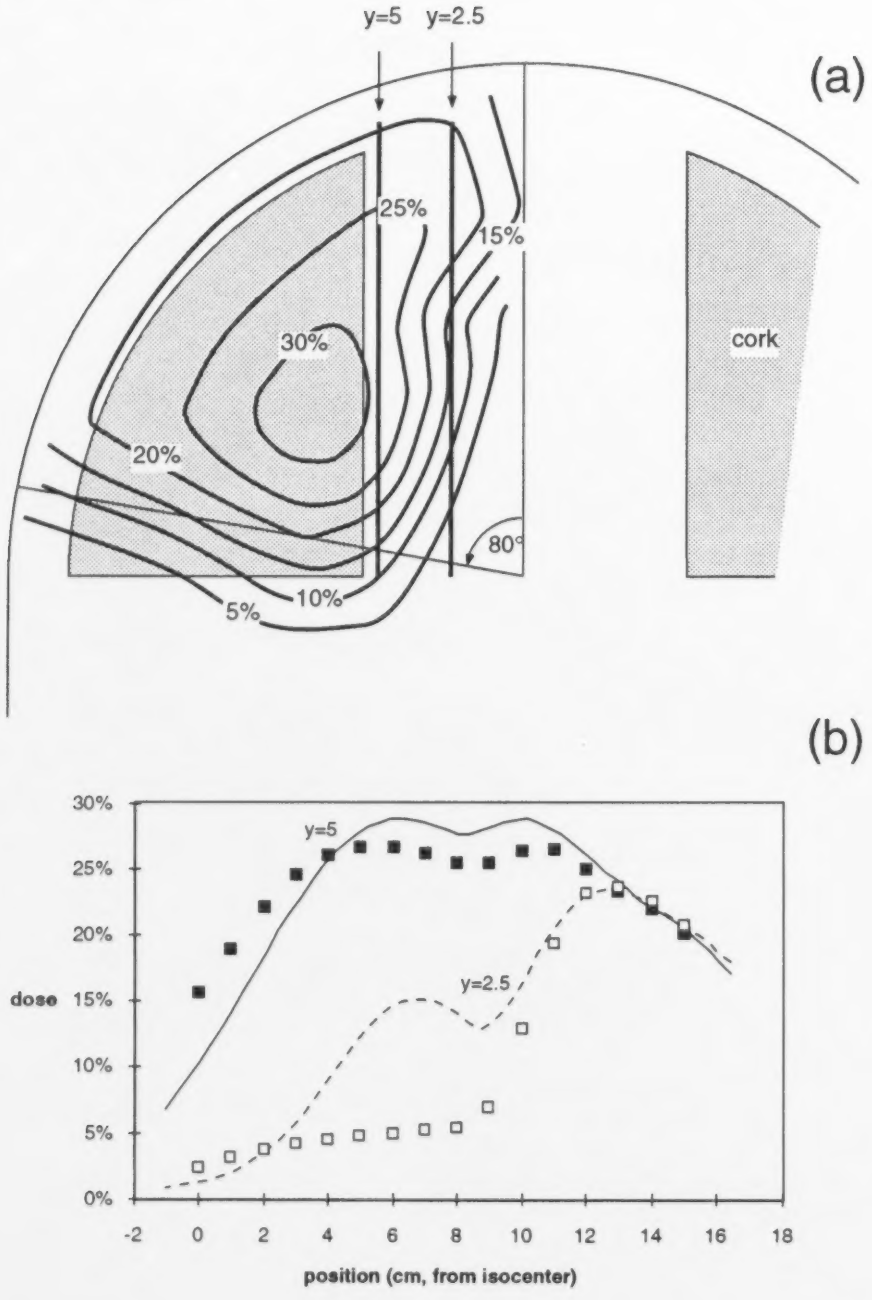

Figure IV.13. Calculated and measured doses profiles for a 16 MeV, 80° arc incident on the lung phantom in figure IV.11. Calculated isodoses are shown in (a). The solid and dashed lines (b) are calculated profiles at y=5 and y=2.5, respectively. The solid and open points are measured doses along the same profiles.

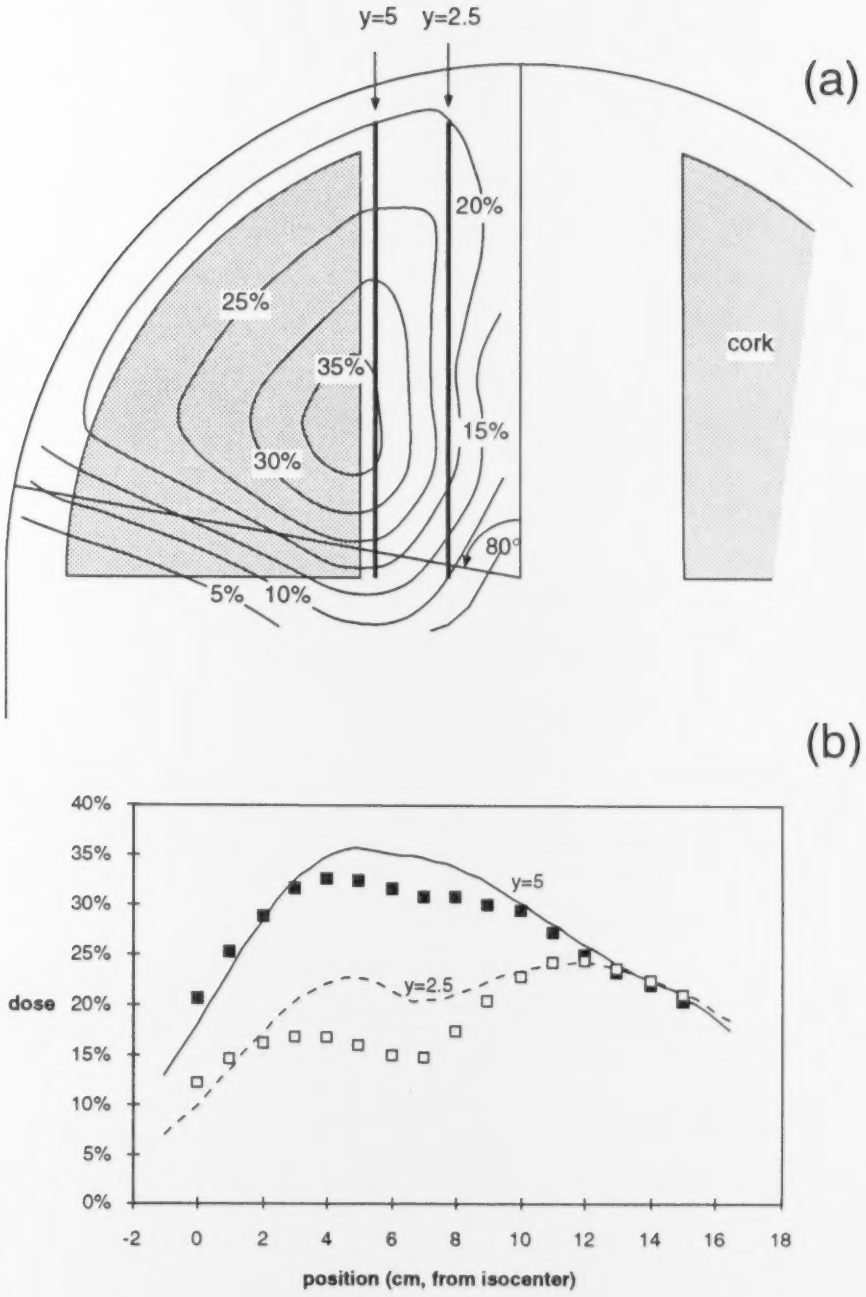

Figure IV.14. Calculated and measured doses profiles for a 20 MeV, 80° arc incident on the lung phantom in figure IV.11. Calculated isodoses are shown in (a). The solid and dashed lines (b) are calculated profiles at y=5 and y=2.5, respectively. The solid and open points are measured doses along the same profiles.

phantom being rotated under the beam. For given radius in the phantom, the arc dose is then equal to the integral under a radial profile of the stationary beam.

We can obtain some insight into the arc algorithm if we deform the cylindrical phantom into a flat, semi-infinite phantom, with the arced beam replaced by a translating beam. The dose distribution is then given by

$$D(x,y,z) = \int_{-\infty}^{\infty} S(x')\, d(x-x',y,z)dx' \qquad \text{(IV.2)}$$

where the beam is directed along the z axis and translated along the x axis. We will consider the beam to have unit intensity from $-\infty$ to $+\infty$ in the x direction and the y extent of the beam will also be infinite. Setting x=y=0 in equation (IV.2) gives the depth dose

$$D(0,0,z) = \int_{-\infty}^{\infty} d(-x',0,z)dx' \qquad \text{(IV.3)}$$

where $d(-x',0,z)$ is the dose distribution due to a stationary beam (not a pencil beam) at the coordinate x'.

It is easy to show that equation (IV.3) is equivalent to the depth dose for a stationary beam with infinite extent in x and y. However, the MDAH algorithm defines the fluence to dose conversion factor $g(z)$ as the infinite field percentage depth dose. Therefore, $D(0,0,z) = g(z)$ in equation (IV.3), and if we extend the analogy back to our cylindrical phantom, the arc depth dose is then very dependent on the way we calculate the fluence to dose conversion factor. From chapter II,

$$g(z) = \frac{D_{ref}(0,0,z)}{\operatorname{erf}\left(\frac{A}{\sqrt{2}\,\sigma_{MCS}}\right) \times \operatorname{erf}\left(\frac{B}{\sqrt{2}\,\sigma_{MCS}}\right)} \qquad \text{(IV.4)}$$

for a rectangular field of dimension $2A \times 2B$. For a given depth z, $g(z)$ increases if σ_{MCS} is increased. The MDAH algorithm includes a multiple Coulomb scattering factor, *FMCS*, which is a multiplicative factor for σ^2_{MCS}. For normal stationary beam treatment planning, this parameter is not very important. Even if it is not adjusted to give the best agreement in the penumbral region, the depth dose predicted by the algorithm is essentially unchanged.

However, for the arc algorithm, the choice of *FMCS* affects the $g(z)$ fluence to dose conversion factor through equation (IV.4), and therefore the predicted depth dose for the arced beam.

To show the effect of the choice of *FMCS* on the arc electron pencil beam algorithm output, figure IV.15 shows the depth dose for a 16 MeV 90° arc, as in figure IV.8. In this case, the input data to the algorithm has remained unchanged except for *FMCS*. Note the large effect that changing the *FMCS* parameter has on the predicted maximum dose. The predicted output ranges from 23.9% to 25.4% for a change in *FMCS* from 1.0 to 1.4. In our case, rather than matching penumbra for the stationary beam, we chose to adjust *FMCS* such that the arc output was predicted correctly.

Another feature common to all of the calculated arc depth doses is that the predicted depth of maximum dose is greater than the measured depth of maximum dose. In this case, it is the algorithm's lack of a mechanism to account for range straggling of the electrons. As noted above, the Fermi-Eyges theory predicts that the width of a pencil beam increases monotonically to the end of the range. However, electrons that have been laterally displaced from the axis of the pencil beam, have travelled a larger distance and have therefore lost more energy. This causes the pencil beam width to reach a maximum and then decrease toward the end of the range†.

The MDAH arc algorithm recognizes that in order to predict the correct arc output, the integral under the profiles of the measured and calculated profiles must be equal. To that end, the width of the calculated beam is corrected by a small amount such that the integral under a calculated profile matches the integral under a reference profile, at the depth of maximum dose for a stationary reference beam. However, as observed previously (El Khatib *et al* 1992, Kurup *et al* 1992), the depth of maximum dose for the arc is greater

---

† More details will be given in the following chapter.

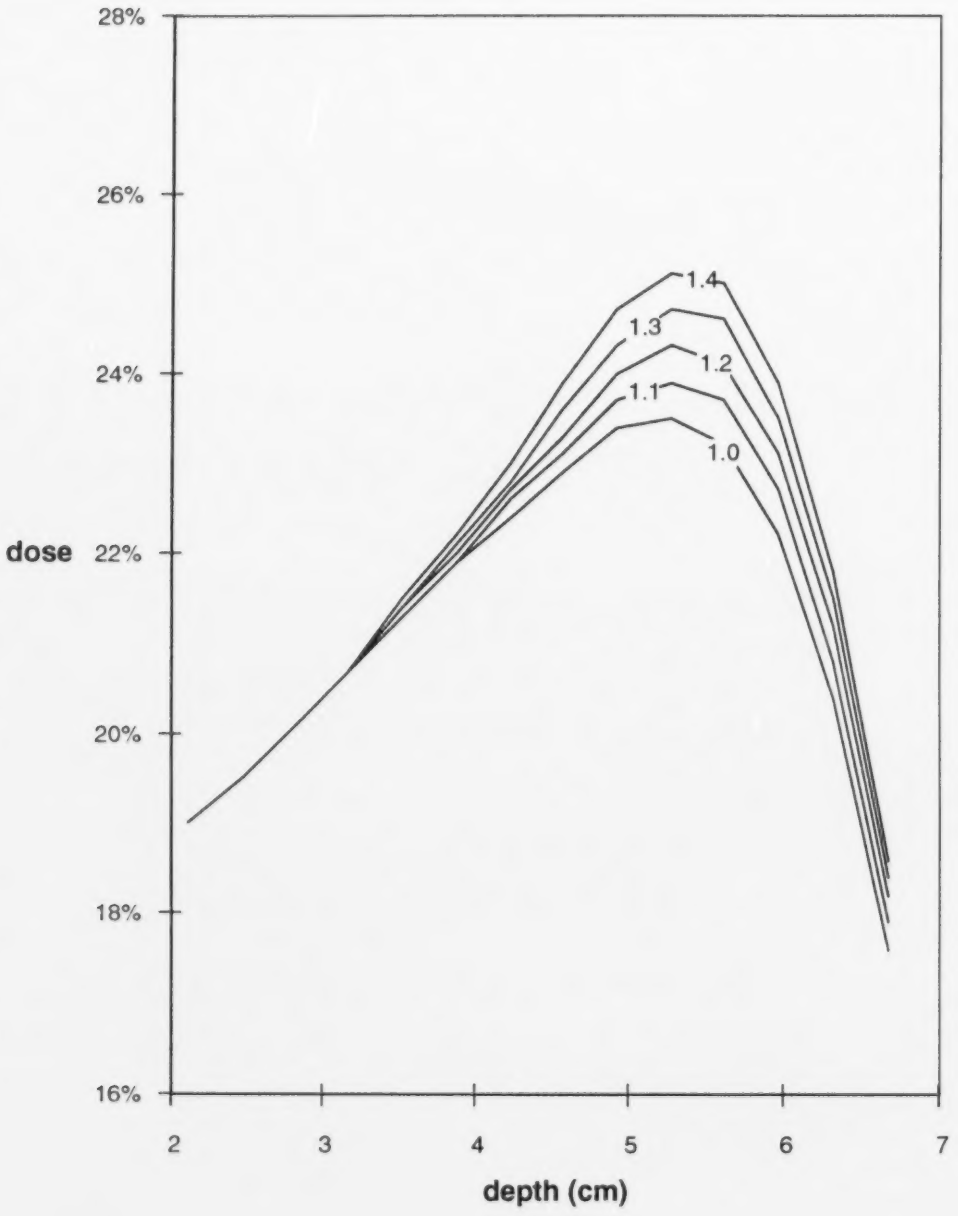

Figure IV.15. The percentage depth dose for a 90° arc of 16 MeV electrons incident on a 17.5 cm radius water phantom, as the multiple Coulomb scattering factor, *FMCS*, varies from 1.0 to 1.4.

than the depth of maximum dose for the stationary beam. At this greater depth, the integrals under the profiles may not necessarily match. In fact, because Fermi-Eyges theory has a monotonically increasing pencil beam width, the fluence to dose conversion factor, $g(z)$, and hence the arc output, is enhanced at depth. This is the reason why the calculated depth of maximum dose is greater than the measured depth of maximum dose.

There are two ways to improve this situation. The first is to estimate (or measure) the depth of maximum dose for the arced beam, and then match integrals under calculated and measured profiles at this depth. This would ensure that the dose output at the measured depth of maximum dose would match, but the dose at slightly greater depths may be even greater, because of the fluence to dose conversion factor enhancement mentioned above. The other method would be to incorporate range straggling effects on the pencil beam width into the algorithm. The next chapter investigates some methods for doing this, and shows the effect on the calculated arc output.

V. Range Straggling Modification

A. *Introduction*

Even with the success of Fermi-Eyges based pencil beam algorithms for electron transport, there remain some significant shortcomings to this approach. The main problem is the lack of a mechanism in the Fermi-Eyges formalism to model range straggling of the electrons as they penetrate the medium. The present theory assumes that all of the electrons in the pencil beam lose the same amount of energy per unit depth, regardless of the lateral displacement occurring as a result of multiple Coulomb scattering (MCS). Electrons that have been scattered away from the central axis of the pencil beam have travelled a longer distance, and therefore have lost more energy than electrons along the central axis. The laterally displaced electrons would therefore not penetrate as far as the central axis electrons.

As the pencil beam nears the end of its range, the laterally displaced electrons run out of energy. This implies that the spread of the pencil beam will not increase as quickly as simple Fermi-Eyges theory would imply. The width of the pencil beam is given by

$$\sigma^2_{MCS}(z) = \frac{1}{2}\int_0^z (z-u)^2\, T(u)\, du \qquad \text{(V.1)}$$

as we have seen above. Equation (V.1) implies that the pencil beam width increases monotonically with depth. In reality, measurements and Monte Carlo calculations show that the pencil beam width reaches a maximum and then decreases as the practical range is approached (Werner *et al* 1982, Lax *et al* 1983, Sandison *et al* 1989). Figure V.1 illustrates this phenomenon for a 12 MeV pencil beam in a semi-infinite water phantom. The solid line shows the pencil beam width as calculated using equation (V.1), using accepted scattering powers (ICRU 1984a) adjusted for electron–electron scattering. The discrete points show the pencil beam spread as calculated by the EGS4 (Nelson *et al* 1985) user code DOSRZ, with the PRESTA (Bielajew and Rogers 1986) algorithm enabled. A

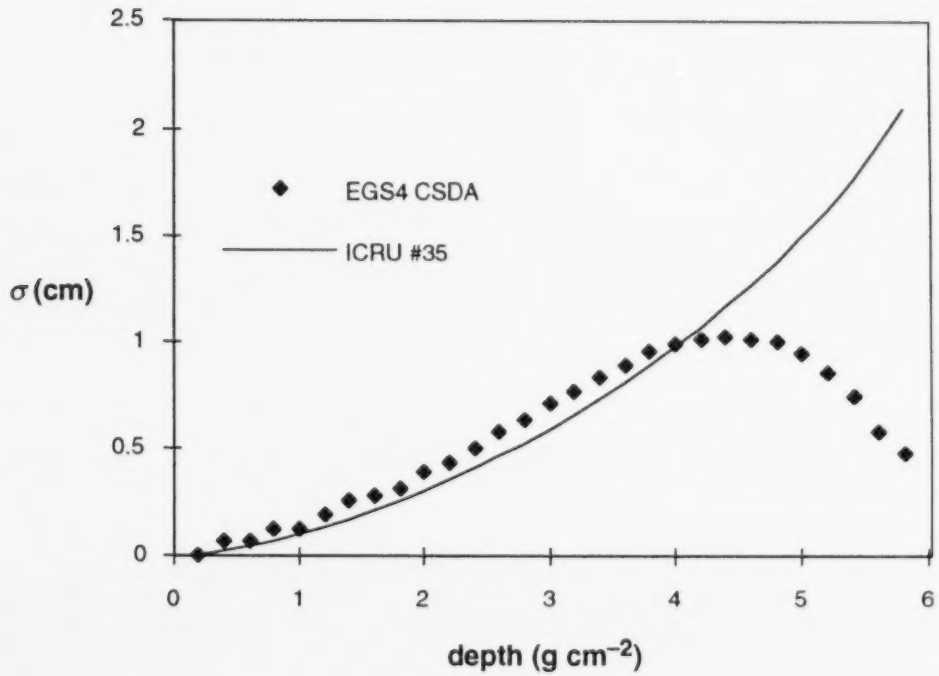

Figure V.1. Pencil beam width for 12 MeV electrons incident on a water phantom. The discrete points were calculated using a Monte Carlo code (see text for details), and the solid line is calculated using Fermi-Eyges theory and ICRU scattering powers (ICRU 1984a).

Continuous Slowing Down Approximation (CSDA) was used so that secondary electrons and bremsstrahlung were not produced. The user code was modified to calculate the variance of the lateral displacement of the electrons as they penetrated the semi-infinite water phantom in the simulation. Figure V.1 clearly shows that the pencil beam width does reach a maximum and then decrease.

In the first half of the range, equation (V.1) underestimates the amount of scattering. This is because Fermi-Eyges theory assumes only small angle scattering. The Monte Carlo calculation is based on Moliere's more accurate description of the scattering process (Nelson *et al* 1985). This, along with the polyenergetic nature of 'real' electron beams, is the reason that the multiple Coulomb scattering factor, *FMCS*, is needed in the MDAH algorithm. The MDAH algorithm calculates the pencil beam width using

$$\sigma^2_{MDAH} = FMCS \times \sigma^2_{MCS} \qquad \text{(V.2)}$$

where σ^2_{MCS} is given by equation (V.1) and *FMCS* is a constant which is usually in the range 1.0–1.4 (Hogstrom 1987). The parameter *FMCS* is adjusted to give better agreement between measured and calculated isodoses in the penumbral region of a reference beam, usually 10×10 cm^2.

Both the stationary beam and arc electron pencil beam algorithms would benefit from a more accurate prediction of the pencil beam width. In the stationary beam algorithm, the benefit would be more accurate dose predictions in the penumbral region. For treatment techniques involving multiple electron and/or photon fields, this would give better beam matching and thus more accurate results.

The benefit of more accurate pencil beam widths for the arc electron pencil beam algorithm would be twofold. The first would be more precise dose predictions in the penumbra, as for the stationary beam algorithm. The second, more important, is better predictions of arc electron beam output. As seen above, the output of a moving electron beam can be calculated as the integral under a profile of a stationary beam, given certain

symmetry constraints. The profile of the stationary beam is characterized by two parameters; its amplitude and penumbral width. In the MDAH algorithm, the amplitude is given by a measured depth dose value and is therefore fixed. The penumbral width is proportional to the pencil beam width σ_{MCS}, and is therefore affected by *FMCS*. In the previous chapter, the *FMCS* parameter was adjusted to predict the beam output more accurately, or to give the correct width of the stationary beam at the depth of maximum dose of the arced beam.

B. Empirical Modification of the Pencil Beam Width

1. FMCS modification

Examining equations (V.1) and (V.2) suggests two simple methods of improving the prediction of the pencil beam width in the MDAH algorithms. The simplest method is to allow the multiple Coulomb scattering factor, *FMCS*, to be a function of the effective depth in the phantom (patient). Equation (V.1) can be rewritten as

$$\sigma^2_{\mathrm{MCS}}(z) = \xi^2(z) \times \frac{1}{2} \int_0^z (z-u)^2 \, T(u) \, du \qquad \text{(V.3)}$$

where $\xi^2(z)$ is the depth dependent *FMCS* parameter. The parameter $\xi(z)$ can be derived from measured data and is the ratio of the measured pencil beam width to the pencil beam width given by equation (V.1), using ICRU #35 (ICRU 1984a) scattering powers, corrected for electron-electron scattering.

It will be useful to change variables in equation (V.3) so that

$$\sigma^2_{\mathrm{MCS}}(z') = \xi^2(z') \times \frac{1}{2} \int_0^{z'} \frac{1}{\rho^2} (z'-u')^2 \, \frac{T(u')}{\rho} \, du' \quad , \qquad \text{(V.4)}$$

where the primed variables have been density scaled, expressed in g cm^{-2}. If we assume that

$$E(u') = E_0 \left(1 - \frac{u'}{R_p} \right) \qquad \text{(V.5)}$$

where R_p is the practical range in g cm^{-2}, then the mass scattering power in equation (V.4) is independent of density. If we further assume that the medium is homogeneous, then

$$(\sigma')^2_{MCS}(z') = \xi^2(z') \times \frac{1}{2} \int_0^{z'} (z'-u')^2 \frac{T(u')}{\rho} du' \qquad (V.6)$$

where σ' is also density scaled. If $\xi^2(z')=1$, or at least independent of density, then $\sigma'(z)$ is also independent of density.

Figures V.2 and V.3 show that the above assumptions are reasonable. Figure V.2 shows the Monte Carlo (EGS4) calculated percentage depth dose for a broad beam of 12 MeV electrons incident on a semi-infinite water phantom, where the density of the phantom has been specified to be 0.625, 1.0, and 2.0 g cm^{-3}. The depth axis has been density scaled and the three depth doses agree well within the statistical uncertainty of the calculation, implying that equations (V.4) and (V.5) are reasonable approximations. Figure V.3 shows a histogram of the lateral dose deposition at a depth of 3 g cm^{-2} for a pencil beam of 12 MeV electrons. This graph implies that $\sigma'(z)$ is independent of density, so $\xi^2(z')$ must be independent of density in order for equation (V.6) to be valid.

Some authors have previously attempted to modify Fermi-Eyges theory to include the effects of range straggling. A simple solution has been found (Werner *et al* 1982) that, similarly to $\xi^2(z')$, multiplies the pencil beam width by a depth dependent function to account for range straggling. If we let

$$\sigma(z') = \sigma(z')_{FE} \times \xi(z') \qquad (V.7)$$

then Werner's solution for $\xi(z')$ gives

$$\xi(z')_{werner} = \text{erf}\left[\frac{\pi}{4\sqrt{2}\sigma_{\theta_x}(z')}\right] \qquad (V.8)$$

where

$$\sigma^2_{\theta_x}(z') = \frac{1}{2} \int_0^{z'} \frac{T(u')}{\rho} du' \qquad (V.9)$$

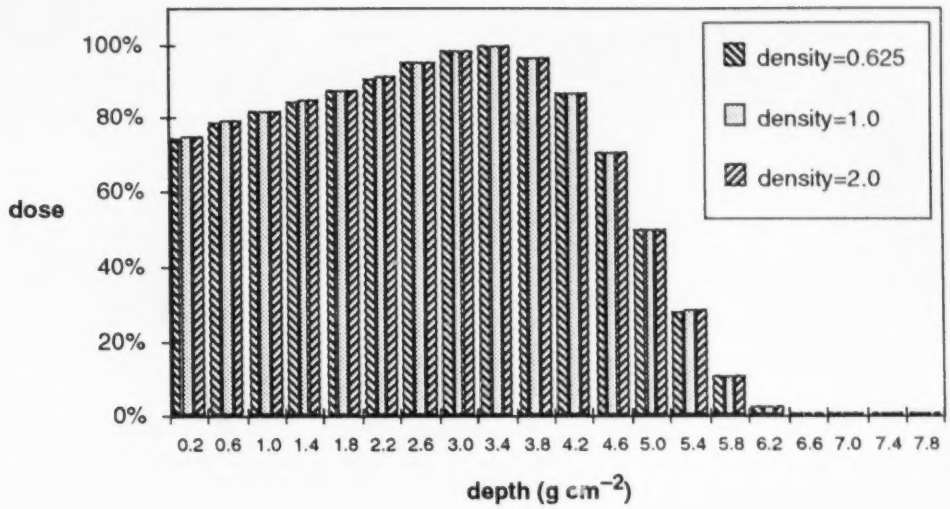

Figure V.2. Percentage depth dose for 12 MeV electrons incident on a water phantom, for various densities of water. The horizontal axis labels indicate the midpoints of the Monte Carlo dose scoring regions.

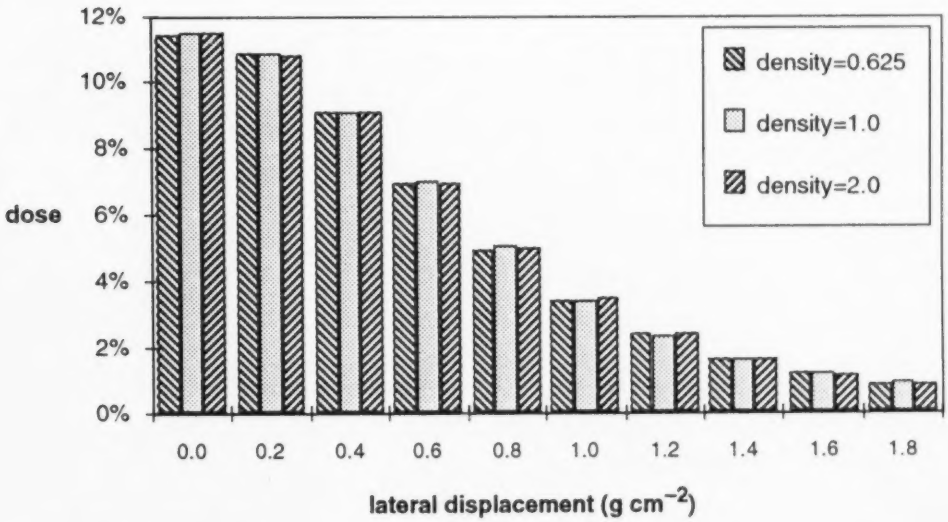

Figure V.3. Lateral dose distribution for 12 MeV electrons incident on a homogeneous water phantom of varying density, at a depth of 3.0 g cm^{-2}. The horizontal axis labels indicate the midpoints of the dose scoring regions.

is the zero scattering moment from standard Fermi-Eyges theory. Equation (V.8) is obtained by considering all electrons scattered to angles greater than $\pi/4$ to be lost from the pencil beam. Lax *et al* (1983) also give a functional form obtained by fitting to Monte Carlo generated pencil beam width data. Their multiplicative factor is given by

$$\xi(z')_{\text{lax}} = \exp\left[-S^{12(1.5-S)}\right] \tag{V.10}$$

where

$$S = 0.95\left(z'/R_p\right) \tag{V.11}$$

and R_p is the practical range of the incident electrons. The functions $\xi(z')_{\text{werner}}$ and $\xi(z')_{\text{lax}}$ have been investigated for homogeneous phantoms using measured data and pencil beams (Sandison *et al* 1989), but the agreement for the non-water materials is not very good. In order to have better agreement, the authors generalized equation (V.10), using three parameters, which were then fitted for each phantom. The resultant parameters show no apparent systematic variation with the density of the phantom and it is doubtful whether this approach will work for heterogeneous phantoms.

2. *Scattering power modification*

Another possible method for more accurately calculating pencil beam widths is to derive a functional form of the scattering power, $T_M(z)$, such that evaluating equation (V.1), using the derived scattering power, returns measured values of the pencil beam width in a water phantom. The scattering power for non-water materials would be calculated in the same manner as the current MDAH algorithm, except that $T_M(z)$ would be used instead of tabulated ICRU scattering powers (ICRU 1984a). The scattering power method for correcting the pencil beam width is then

$$\sigma^2_{\text{MCS}}(z') = \frac{1}{2}\int_0^{z'} \frac{1}{\rho^2}(z'-u')^2\left(\frac{T(u')}{\rho}\right)_M du' \tag{V.12}$$

where the primed variables are density scaled, or 'effective' depths, and the mass scattering power, $\left(\frac{T(u')}{\rho}\right)_M$, is equal to $T_M(u)$, which is derived from water phantom data.

Deriving $T_M(z)$ from pencil beam width data is reasonably simple. If we assume some parameterized functional form for $T_M(z)$, then equation (V.1) or (V.12) can be integrated, giving a parameterized functional form for the pencil beam variance. The parameters can then be adjusted, using some form of least squares fitting procedure, to give a good fit to the pencil beam width data. The parameters can then be used to calculate $T_M(z)$.

It is also possible to derive $T_M(z)$ from the pencil beam width data by solving equation (V.1) for $T_M(z)$. The third derivative of equation (V.1) is

$$\frac{d^3}{dz^3}\sigma^2(z) = T(z) \quad , \tag{V.13}$$

which implies that $T_M(z)$ can be obtained from the third derivative of measured (or calculated) pencil beam width data.

In order to use equation (V.12) to calculate the pencil beam width, we need to derive $\left(\frac{T(u')}{\rho}\right)_M$ using equation (V.13). There are several ways of obtaining pencil beam width information from broad beams (Sandison *et al* 1989), but the resulting data is usually quite noisy. Differentiating the data three times only serves to amplify the noise. To overcome this difficulty, we can use a smooth curve of known functional form to approximate the measured data, and then differentiate the function. Having a smooth function to represent the measured data will actually help with both the scattering power modification and the *FMCS* modification. Because there is no simple functional form for the pencil beam spread, we chose to fit the data to a polynomial spline curve.

If we define the function $f(z)$ on the interval $z=0$ to $z=z_n$ as

$$f(z) = \begin{cases} f_1(z) & z_0<z<z_1 \\ f_2(z) & z_1<z<z_2 \\ \cdot & \cdot \\ \cdot & \cdot \\ f_n(z) & z_{n-1}<z<z_n \end{cases} \qquad \text{(V.14)}$$

then $f(z)$ is a spline curve (Späth 1974). The functions $f_i(z)$ can be polynomials, and therefore the coefficients of the polynomials and the coordinates $z_1 \ldots z_{n-1}$ are parameters of the spline. The parameters are defined by the constraints on the spline, such as the values of the function at certain points, and the degree of continuity of the function at the boundaries of the intervals. Because the scattering power is the third derivative of σ^2, we need to use at least a third order polynomial spline to get a non-zero scattering power. A fifth order polynomial spline with continuous fourth derivative would give a scattering power with a continuous first derivative, so that the scattering power would be a 'smooth' function.

For an n interval fifth order polynomial spline fit, we have $6n$ parameters for the individual polynomials.Continuity conditions at $n-1$ interval boundaries eliminate $5(n-1)$ of these parameters. If we allow the interval boundaries to be variable then we can add $n-1$ more parameters $z_1 \ldots z_{n-1}$. The z coordinates of the endpoints of the curve are fixed. This leaves $(2n+4)$ parameters. In some cases, it may also be useful to specify the value of the slope at the endpoints of the spline curve. The fifth order polynomial spline curve for the pencil beam width is therefore

$$\sigma_i^2(z) = a_i + b_i(z-z_{i-1}) + c_i(z-z_{i-1})^2 + d_i(z-z_{i-1})^3 + e_i(z-z_{i-1})^4 + f_i(z-z_{i-1})^5 \qquad \text{(V.15)}$$

where

$$a_i = a_{i-1} + b_{i-1}(z_{i-1}-z_{i-2}) + c_{i-1}(z_{i-1}-z_{i-2})^2 + d_{i-1}(z_{i-1}-z_{i-2})^3 + e_{i-1}(z_{i-1}-z_{i-2})^4 + f_{i-1}(z_{i-1}-z_{i-2})^5 \quad , \qquad \text{(V.16)}$$

$$b_i = b_{i-1} + 2c_{i-1}(z_{i-1}-z_{i-2}) + 3d_{i-1}(z_{i-1}-z_{i-2}))^2 + 4e_{i-1}(z_{i-1}-z_{i-2}))^3 + 5f_{i-1}(z_{i-1}-z_{i-2}))^4 \quad , \tag{V.17}$$

$$c_i = c_{i-1} + 3d_{i-1}(z_{i-1}-z_{i-2})) + 6e_{i-1}(z_{i-1}-z_{i-2}))^2 + 10f_{i-1}(z_{i-1}-z_{i-2}))^3 \quad , \tag{V.18}$$

$$d_i = d_{i-1} + 4e_{i-1}(z_{i-1}-z_{i-2})) + 10f_{i-1}(z_{i-1}-z_{i-2}))^2 \quad , \text{and} \tag{V.19}$$

$$e_i = e_{i-1} + 5f_{i-1}(z_{i-1}-z_{i-2})) \tag{V.20}$$

specify the conditions for continuity of the zero through fourth derivatives, respectively. If we insert z_0=0 and equations (V.16) through (V.20) into equation (V.15), then we get the general result for $z_{i-1} < z < z_i$,

$$\sigma_i^2 = a_1 + b_1 z + c_1 z^2 + d_1 z^3 + e_1 z^4 + \sum_{j=1}^{i} (f_j - f_{j-1})(z - z_{j-1})^5 \tag{V.21}$$

where f_0=0. Differentiating three times with respect to z gives

$$T(z) = 6d_1 + 24e_1 z + 60 \sum_{j=1}^{i} (f_j - f_{j-1})(z - z_{j-1})^2 \tag{V.22}$$

as the scattering power, or if ρ=1, the mass scattering power. For the scattering power modification, equation (V.22) can then be inserted into equation (V.12) to calculate the pencil beam width. If the material is homogeneous, then the solution of equation (V.12) returns equation (V.21), except that the left hand side will be multiplied by ρ^2.

The general solution of equation (V.12) given the mass scattering power of equation (V.22) is slightly more complicated. If we define ρ_j as the density of the j^{th} region, then, for $z_{i-1} < z < z_i$, the solution is

$$\sigma_{MCS}^2(z') = \sum_{j=1}^{i} \left\{ \left(\frac{d_j}{\rho_j^2} - \frac{d_{j-1} + 4e_{j-1}(z'_{j-1} - z'_{j-2}) + 10f_{j-1}(z'_{j-1} - z'_{j-2})^2}{\rho_{j-1}^2} \right) (z' - z'_{j-1})^3 + \left(\frac{e_j}{\rho_j^2} - \frac{e_{j-1} + 5f_{j-1}(z'_{j-1} - z'_{j-2})}{\rho_{j-1}^2} \right) (z' - z'_{j-1})^4 + \left(\frac{f_j}{\rho_j^2} - \frac{f_{j-1}}{\rho_{j-1}^2} \right) (z' - z'_{j-1})^5 \right\} \tag{V.23}$$

where the intervals include the z_i' from the original spline fit, and the boundaries introduced by discontinuities in the phantom material.

Comparing equations (V.21) and (V.22), we see that the parameters a_1, b_1, and c_1 are not involved in the scattering power. Their physical significance can be seen if we compare equation (V.21) to the general solution for the width of a Gaussian beam (ICRU 1984a)

$$\sigma^2(z) = \sigma_0^2 + 2(\overline{\theta_x x})_0 z + \sigma_{\theta_x}^2 z^2 + \frac{1}{2}\int_0^z (z-u)^2\, T(u)\, du \qquad \text{(V.24)}$$

where σ_0^2 is the initial variance, $\sigma_{\theta_x}^2$ is the initial angular variance and $(\overline{\theta_x x})_0$ is the initial covariance of the Gaussian pencil beam. Therefore

$$a_1 = \sigma_0^2 \qquad \text{(V.25)}$$

$$b_1 = 2(\overline{\theta_x x})_0 \qquad \text{(V.26)}$$

$$c_1 = \sigma_{\theta_x}^2 \qquad \text{(V.27)}$$

are the additional parameters in equation (V.21). When we fit equation (V.21) to measured or calculated pencil beam data, the parameters a_1, b_1, and c_1 are used to define the initial parameters of the pencil beam.

C. Monte Carlo Results

To compare the various methods of modifying the pencil beam widths, we need some data for $\sigma^2(z')$ for homogeneous and heterogeneous slab phantoms. Measurements in water are fairly easy, but heterogeneous phantoms present a problem. Another way to test the modifications is to do a computer simulation. Using the EGS4 (Nelson *et al* 1985) user code DOSRZ, a series of simulations were performed to calculate pencil beam widths in semi-infinite water phantoms. Using the PEGS4 preprocessor, several different densities of water were simulated, from 0.32 g cm^{-3} to 2.0 g cm^{-3}. The simulation geometry consisted of a series of slabs of constant mass thickness (0.2 g cm^{-2}), but with varying densities. At every planar boundary, the electron's position and its square were accumulated so that the variance of the position could be computed at the end of the simulation. All of the simulations used a zero-radius monoenergetic, monodirectional pencil

beam of 12 MeV electrons. Most of the simulations consisted of 140,000 electron histories, and approximately 12 hours of CPU time (VAXstation 3520) was needed per simulation. To simplify the simulation, a CSDA approximation was used, so that secondary electrons and bremsstrahlung were not produced. The data were analyzed using a spreadsheet program (Microsoft Excel, Redmond, WA) on a personal computer.

1. Homogeneous phantoms

The first phantom simulated was a unit density water phantom. The resultant pencil beam widths were shown in figure V.1. The data was fit to equation (V.21) using three intervals in z. The best fit criteria was to minimize the sum of the squares of the differences between the Monte Carlo pencil beam standard deviation at 0.2 g cm^{-2} intervals and the standard deviation as calculated using equation (V.21). The parameters a_1, b_1, and c_1 were set equal to zero, since the simulated pencil beam had no initial variance. To ensure that the scattering power was positive at z=0, the parameter d_1 was constrained to be greater than zero.

Figure V.4 shows $\xi(z')$ derived for the *FMCS* correction, equation (V.4), the Werner correction, equation (V.8) and the Lax correction, equation (V.10). The Werner and Lax corrections are similar in that they start at unity and then decrease as the depth approaches the practical range, which is 5.75 cm in this case. The main difference is where the two corrections start to decrease the pencil beam width ($\xi(z')<1$). The *FMCS* correction does not necessarily start at unity, since it was derived from the ratio of Monte Carlo data and Fermi-Eyges predictions. For depths less than 4 g cm^{-2}, the *FMCS* correction enhances the scattering of the electrons, which is needed since the Monte Carlo data does not exclude large angle scattering. Lax *et al* (1983) have shown that the rms radial spread (standard deviation) of a pencil beam is significantly greater than the $1/e$ width of the pencil beam at shallow depths, mainly due to the large angle scattering tail in the scattering

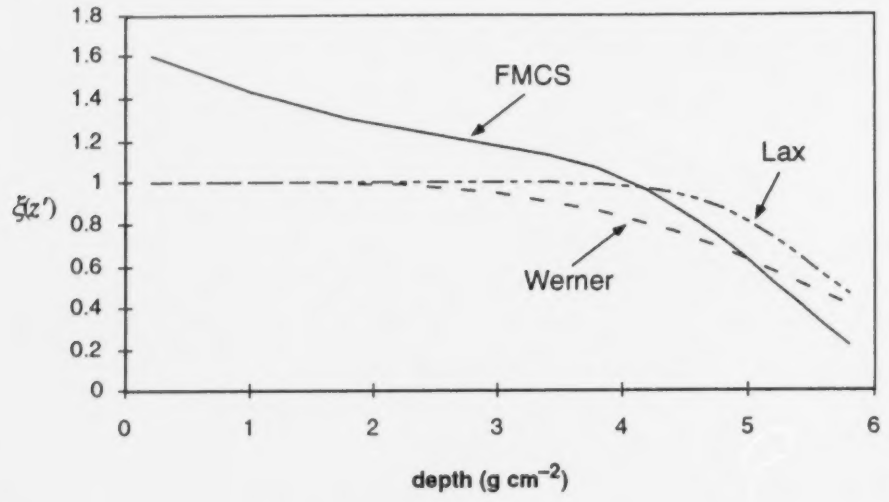

Figure V.4. Comparison of multiplicative pencil beam width correction factors calculated for a 12 MeV monoenergetic electron beam.

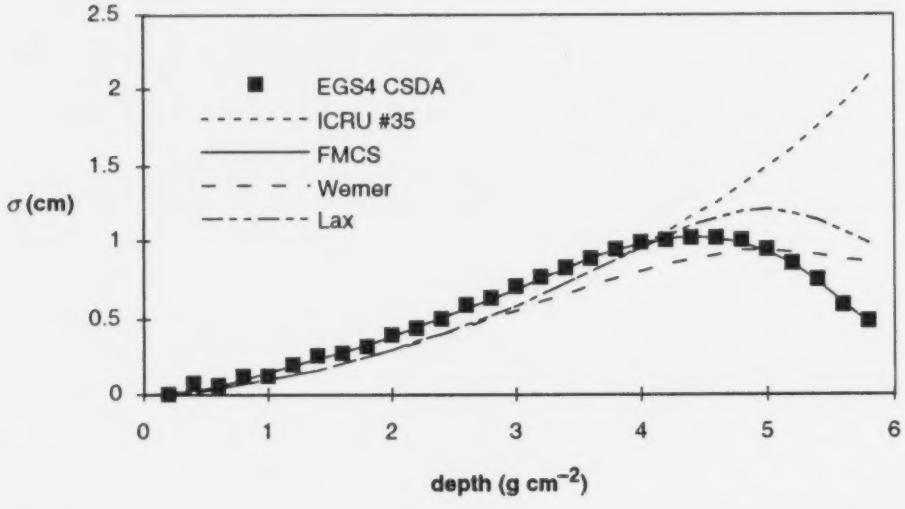

Figure V.5. Comparison of pencil beam width corrections calculated for a 12 MeV monoenergetic electron beam incident on a water phantom. The discrete points are Monte Carlo calculated results and the short dashed line is the pencil beam width predicted by Fermi-Eyges theory using ICRU scattering powers (ICRU 1984a).

distribution†. The Werner and Lax corrections are derived to predict the $1/e$ width, ignoring the large angle scattering tail at shallow depths. The parameter S, in the Lax correction method was also fit to radial dose profiles, as opposed to radial fluence profiles, which are slightly different (Lax *et al* 1983). In all of the pencil beam width correction methods, the pencil beam width is decreased at greater depths to account for electrons lost from the pencil beam due to range straggling.

Figure V.5 shows the result of applying the $\xi(z')$ corrections to the Fermi-Eyges predictions for the pencil beam width. The Monte Carlo data is shown as discrete points and the Fermi-Eyges prediction, solving equation (V.1) using accepted scattering powers corrected for electron-electron scattering (ICRU 1984a), is labelled ICRU #35. As expected, the result of applying the *FMCS* correction is to return the polynomial spline curve used to fit the unit density water data. The Werner correction underpredicts the maximum pencil beam width slightly, and the Lax correction overpredicts the maximum pencil beam width. The position of the maximum is also deeper than the Monte Carlo data, for both the Werner and Lax corrections. The results of the Werner and Lax pencil beam width corrections are qualitatively similar to previously published results (Sandison *et al* 1989). This is not really a fair test of the Werner and Lax pencil beam width corrections because, as noted above, they are trying to predict the $1/e$ width of the pencil beam, as opposed to the rms spatial spread, which is calculated in the Monte Carlo simulation. The inclusion of large angle scattering in the Monte Carlo simulation leads to larger pencil beam widths than predicted using simple Fermi-Eyges theory, which is seen in figure V.5 and observed by Lax *et al* (1983). The generalised Gaussian model (Lax *et al* 1983, Lax 1986a) was developed to include the effects of the large angle scattering tail, but will not be discussed here.

---

† For a purely Gaussian distribution, the rms spatial width is equal to the $1/e$ width.

In apparent contradiction to figure V.5, Sandison *et al* (1989) found that the Monte Carlo pencil beam width was consistently less than that predicted by Fermi-Eyges theory. Their data for pencil beam width was the $1/e$ width of the absorbed dose in a Monte Carlo simulation, and the $1/e$ width is much smaller than the rms width at small depths, and the width of the dose profile is actually slightly smaller than the width of the primary fluence profile (Lax *et al* 1983). Fermi-Eyges theory gives the $1/e$ width of the primary fluence profile. This implies that our data is not inconsistent with Sandison *et al* (1989).

The mass scattering power, to be used by the scattering power correction from equation (V.22), is shown in figure V.6, as a function of energy of the electrons, as given by equation (V.5). The pencil beam width predicted for the homogeneous water phantom is exactly the same as for the *FMCS* correction in figure V.5, as expected. Notice that the scattering power used by the scattering power correction is less than zero in the region where the pencil beam width is maximum. The negative scattering power can be interpreted as stripping away electrons, slowing down the increase in pencil beam width.

2. *Heterogeneous phantoms*

The next step was to compare the above pencil beam width corrections to data for heterogeneous phantoms to estimate their usefulness in clinical situations. The Monte Carlo phantoms consisted of slabs of water of different densities, from 0.32–2.0 g cm^{-3}. These phantoms were consistent with Fermi-Eyges theory, so any discrepancies were due to deficiencies in the scattering theory, and the pencil beam width corrections.

The first phantom consisted of a 1 cm slab of unit density water, followed by 7 g cm^{-2} of water with a density of 0.8 g cm^{-3}. The pencil beam width data for this phantom is shown in figure V.7. Because the density of the second slab of water is close to unit density, maximum pencil beam width for the Monte Carlo data increases only slightly, from about 1.0 cm in figure V.5 to about 1.25 cm in figure V.7. For both the Werner and

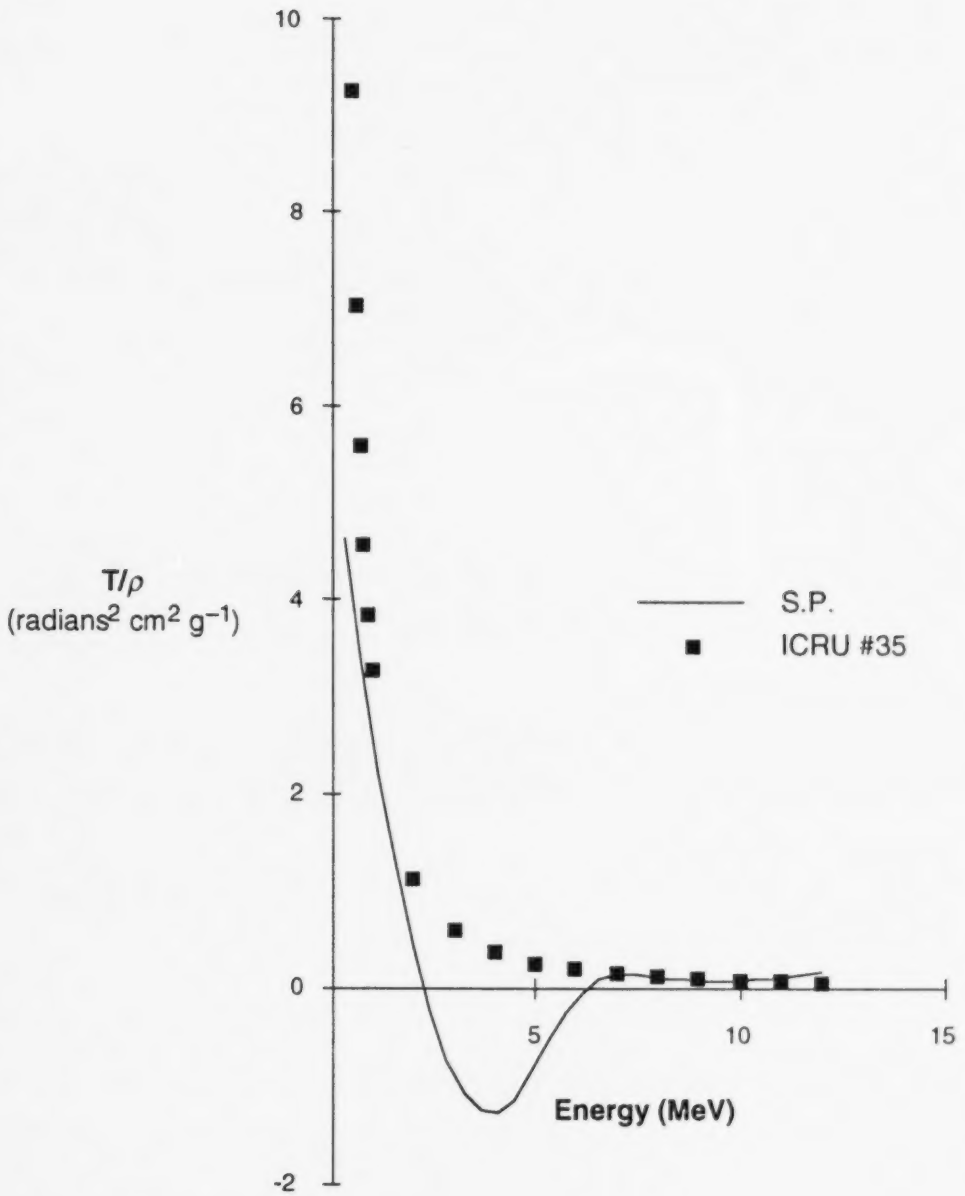

Figure V.6. Comparison of scattering power used by the scattering power correction (labelled S.P. in the following figures) to ICRU scattering powers (ICRU 1984a).

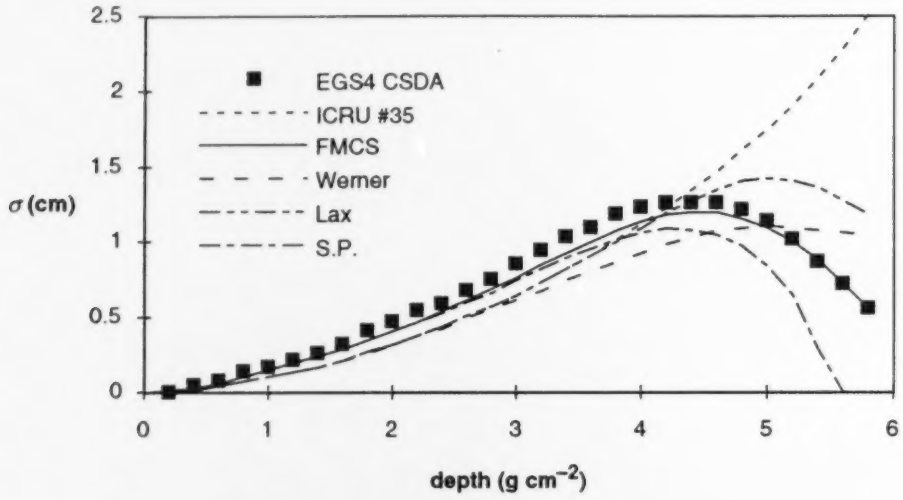

Figure V.7. Calculated pencil beam widths for 12 MeV electrons incident on a water phantom composed of 1 cm of unit density water followed by water of density 0.8 g cm^{-3}. See text for calculation details.

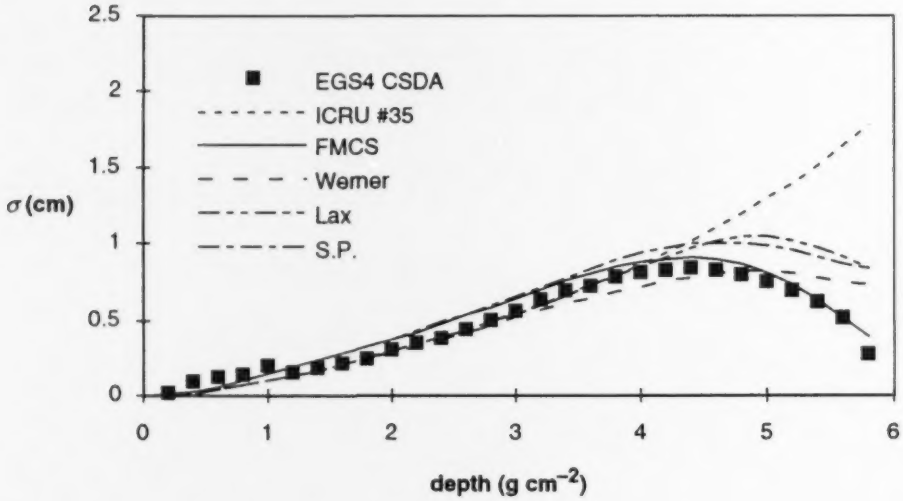

Figure V.8. Calculated pencil beam widths for 12 MeV electrons incident on a water phantom composed of 1 cm of unit density water followed by water of density 1.25 g cm^{-3}. See text for calculation details.

Lax pencil beam width correction methods, the discrepancies between the calculated pencil beam width and the Monte Carlo pencil beam width are qualitatively the same as in figure V.5, except that their magnitude is slightly greater. The *FMCS* method performs reasonably well, with a maximum discrepancy of about 0.1 cm. The scattering power method (labelled S.P.) performs very poorly, predicting that the pencil beam width goes to zero before the practical range.

The next phantom was the same as in figure V.7, except that the second slab had a density of 1.25 g cm^{-3}, and the data is shown in figure V.8. In this case, the maximum pencil beam width is decreased to 0.8 cm, and the *FMCS* method slightly overpredicts this value. The Werner and Lax methods are still not as good as the *FMCS* method, and the scattering power method again performs poorly, although similarly to the Lax method at the end of the range. If we increase the density of the second slab to 2.0 g cm^{-3}, then we get the data shown in figure V.9. The maximum Monte Carlo pencil beam width is about 0.5 cm. In this case the Werner method performs best up to a depth of about 5 g cm^{-2}, but it fails to decrease the pencil beam width sufficiently at the end of the range. The *FMCS* method overpredicts the maximum pencil beam width by 0.25 cm, and the Lax method overpredicts by a slightly greater amount. The scattering power method again performs very poorly, and predicts that the pencil beam width does not reach a maximum. In the rest of the figures, the scattering power method will not be considered, since it is obviously an incorrect model for range straggling of the electrons.

Figure V.10 shows the pencil beam widths resulting from a 0.32 g cm^{-3} slab following the 1 cm unit density slab. The maximum Monte Carlo pencil beam width is up to about 3 cm, and both the *FMCS* and Werner pencil beam width correction methods underpredict the pencil beam width by about 0.5 cm. The Lax method predicts the correct maximum, but the depth of maximum is not correct. Because the *FMCS* method enhances

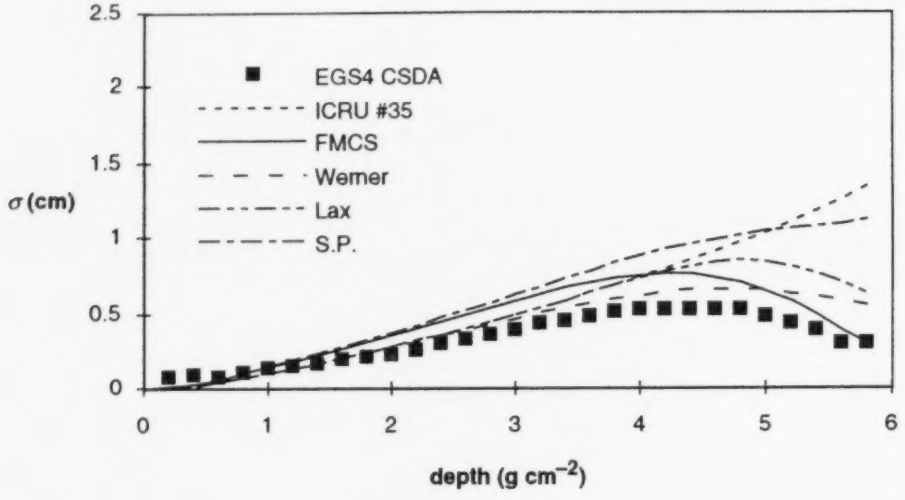

Figure V.9. Calculated pencil beam widths for 12 MeV electrons incident on a water phantom composed of 1 cm of unit density water followed by water of density 2.0 g cm^{-3}. See text for calculation details.

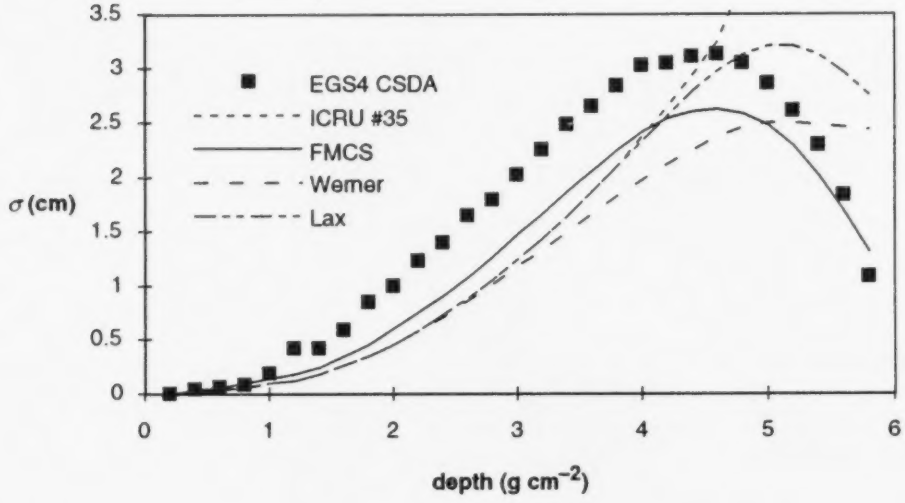

Figure V.10. Calculated pencil beam widths for 12 MeV electrons incident on a water phantom composed of 1 cm of unit density water followed by water of density 0.32 g cm^{-3}. See text for calculation details.

the scattering at shallower depths and is quite close to the Monte Carlo data at the end of the range, it performs the best of all the methods in this case.

If we consider figure V.5 and figures V.7 through V.10 together, the *FMCS* method is the method of choice. In all cases, it gives the best predictions, and in some ways this could be expected. Equation (V.12) was derived using theoretical considerations and involved assumptions about small angle scattering of the electrons. The inability of simple Fermi-Eyges theory to reproduce the upward curve of the Monte Carlo data in figure V.1 shows that small angle scattering is not sufficient to accurately model the beam. Equation (V.14) was obtained by an empirical fit to Monte Carlo data in a homogeneous phantom, however the Monte Carlo data was fit to the $1/e$ width of the dose profile of the pencil beam, so it cannot be expected to fit the rms width of the fluence profile of the pencil beam.

D. Application to Clinical Beams

We decided that the effect, on clinical beam calculations, of correcting the pencil beam width for range straggling should be tested using the algorithms currently available in the Alberta Treatment Planning (ATP) system (Battista *et al* 1984). Because of its good performance, the *FMCS* pencil beam width correction was chosen. The first step is to gather pencil beam width data for the clinical beams. Various methods have been described for obtaining pencil beam spread information from broad beam measurements (Sandison *et al* 1989), however the method chosen for this study is the straightforward, approximate method used to obtain the $\sigma^2_{\theta_x}$ parameter in the MDAH pencil beam algorithm. If you assume that the broad beam is a convolution of a constant source function, and a Gaussian pencil beam kernel, then an approximate formula for the pencil beam spread is given by

$$\sigma \approx \frac{w_{20}-w_{80}}{2} \times 0.595 \qquad \text{(V.28)}$$

where w_{20} (w_{80}) is the width of a profile at 20% (80%) of the central value (Hogstrom 1987). Equation (V.28) is valid as long as lateral scatter equilibrium has been established,

which is true for a 10×10 cm^2 electron beam. Equation (V.21) should enable us to obtain the variance of the pencil beam with sufficient accuracy for our needs.

Using a three dimensional scanning dosimetry system (RFA-7, Scanditronix), dose profiles were obtained at regular depth intervals for a 10×10 cm^2 stationary electron beam at an source-surface distance (SSD) of 90 cm. The beam was produced by a medical linear accelerator (Varian Clinac 2100C), and a p-type diode was used as a dosimeter, because of good spatial resolution and the equivalence of ionization to dose (Rikner 1985). As noted above, the MDAH algorithm separates the electron beam into a primary electron beam and a bremsstrahlung component. This constant bremsstrahlung component was subtracted from each dose profile, before calculating w_{80} and w_{20} for the dose profile. Equation (V.21) was used to calculate the pencil beam spread of the clinical beam. It should be noted that this procedure is not quite the same as for the Monte Carlo experiments, since we are using dose profile as opposed to planar fluence profiles.

As in the MDAH algorithm, the beam was assumed to have an angular variance, $\sigma^2_{\theta_x'}$, at the end of the electron applicator. The end of the applicator was located 5 cm away from the water surface. If we assume that there is no scattering in this air space, as in the MDAH algorithm, then the pencil beams (which form the broad beam) will also have an initial spatial variance and spatial angular covariance at the surface of the water phantom. The initial parameters of the pencil beam are therefore

$$a_1 = 25\ \sigma^2_{\theta_x'},\ b_1 = 10\ \sigma^2_{\theta_x'},\ \textit{and}\ c_1 = \sigma^2_{\theta_x'}, \qquad \text{(V.29)}$$

as given by equations (V.25) through (V.27). Figure V.11 shows the resulting pencil beam widths and the spline curve that was fit to the data for 12 MeV and 16 MeV beams. The parameter d_1, which corresponds to the initial scattering power of the beam, was found to be 0.01344 and 0.00748 for the 12 MeV and 16 MeV beams respectively. This implies scattering powers of 0.0806 cm^{-1} and 0.0449 cm^{-1}, which are greater than the accepted

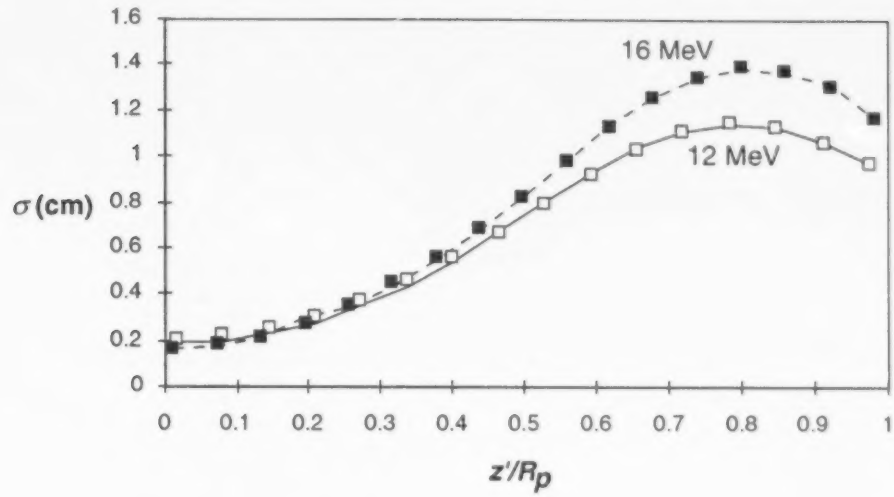

Figure V.11. Pencil beam widths for a clinical electron beam. The discrete points were calculated from broad beam penumbra measurements, and the continuous lines are spline curves fit to the data, as described in the text.

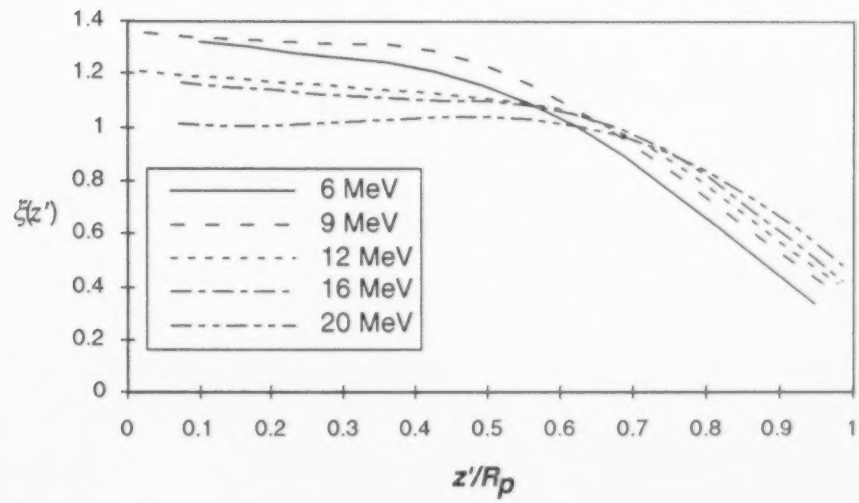

Figure V.12. *FMCS* correction parameter, $\xi(z')$, for the range of electron energies available from a Varian 2100C linear accelerator. The horizontal axis is the depth in water compared to the practical range of the electron beam.

values of 0.055 cm^{-1} and 0.033 cm^{-1}, but must be, to include the large angle scattering tail.

To calculate the *FMCS* correction parameter, the effect of the initial pencil beam angular variance at the electron applicator was subtracted from the spline curve before calculating $\xi(z')$. This is done by subtracting the contributions of the parameters a_1, b_1, and c_1 from equation (V.21), which gives the equation of the spline curve fitted to the pencil beam width data. Figure V.12 shows the $\xi(z')$ for all of the electron energies available on the linear accelerator. All energies show the same general curve, with a relatively constant portion at shallow depths, and then decreasing more towards the end of the range. Except for 6 MeV, there is a systematic variation in the initial constant value, which decreases with energy. For 20 MeV, the initial portion of the curve is very close to unity. For higher energies, there is less large angle scattering, so it would be expected that Fermi-Eyges theory would be a good approximation. For the lower energies, large angle scattering plays a larger role, which implies that $\xi(z')$ would have to be greater than unity. The amount of pencil beam width decrease at the end of the range is also energy dependent. The pencil beam width decrease is not as great for higher energies, which is to be expected.

In the MDAH algorithm, the pencil beam spread due to multiple scattering is given by equation (V.2). To incorporate $\xi(z')$ into the MDAH algorithm, the constant *FMCS* was replaced by a function call, which returns $\xi^2(z')$, as in equation (V.4). The results for a homogeneous water phantom are shown in figure V.13. The solid lines show measured isodose lines in 10% increments. The dashed lines on the left hand side show the default MDAH results, using a constant *FMCS*. The right hand side has been modified with $\xi(z')$, and shows great improvement in matching the isodose lines at all depths.

We stated above that another benefit of improving the pencil beam width calculation would also be more accurate prediction of arc electron dose output. Figures V.14 and V.15 show the depth dose for a 90° arc of 16 MeV and 20 MeV electrons, respectively. The

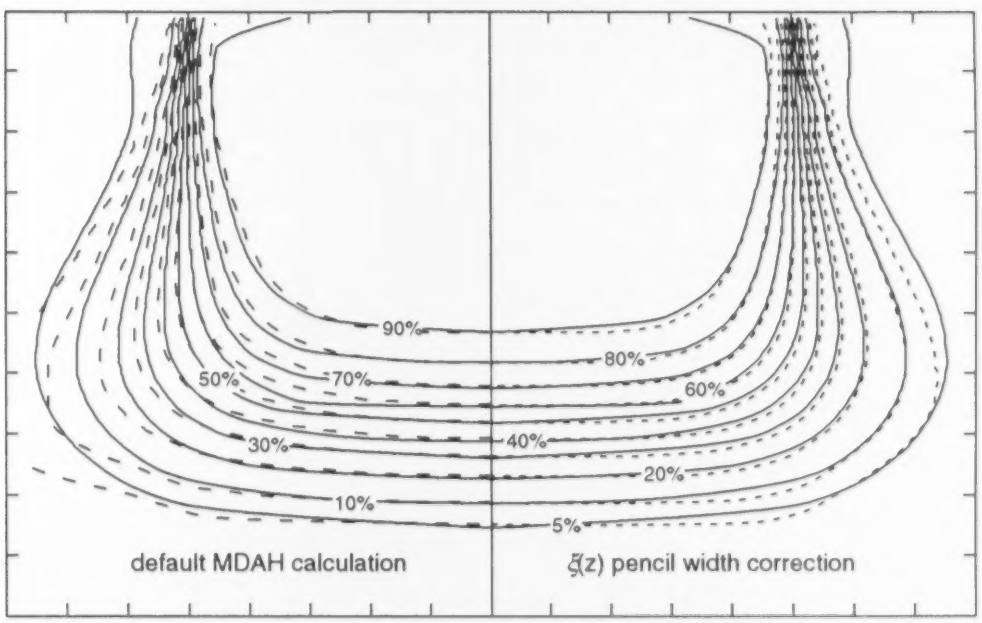

Figure V.13. Isodose lines for a 10×10 cm^2 field of 16 MeV electrons incident on a water phantom. The solid lines are measured data; the dashed line on the left hand is the default MDAH calculation; and the dashed line on the right hand side is calculated using $\xi(z')$.

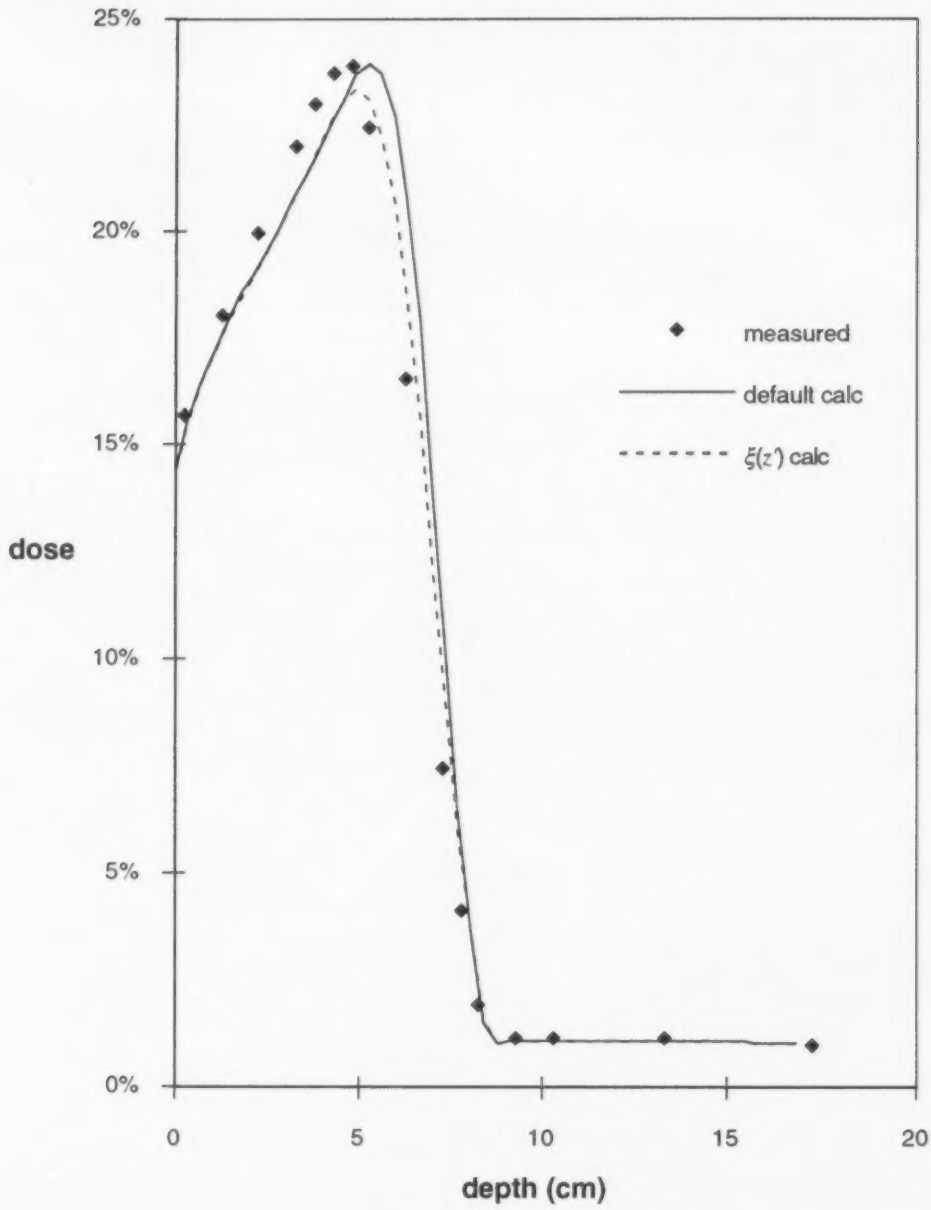

Figure V.14. Mid-arc percentage depth dose for a 16 MeV 90° arc on a 17.5 cm radius phantom. The discrete points are measured with a diode in a water phantom; the solid line is calculated using the default MDAH arc electron pencil beam algorithm; and the dashed line is calculated using $\xi(z')$.

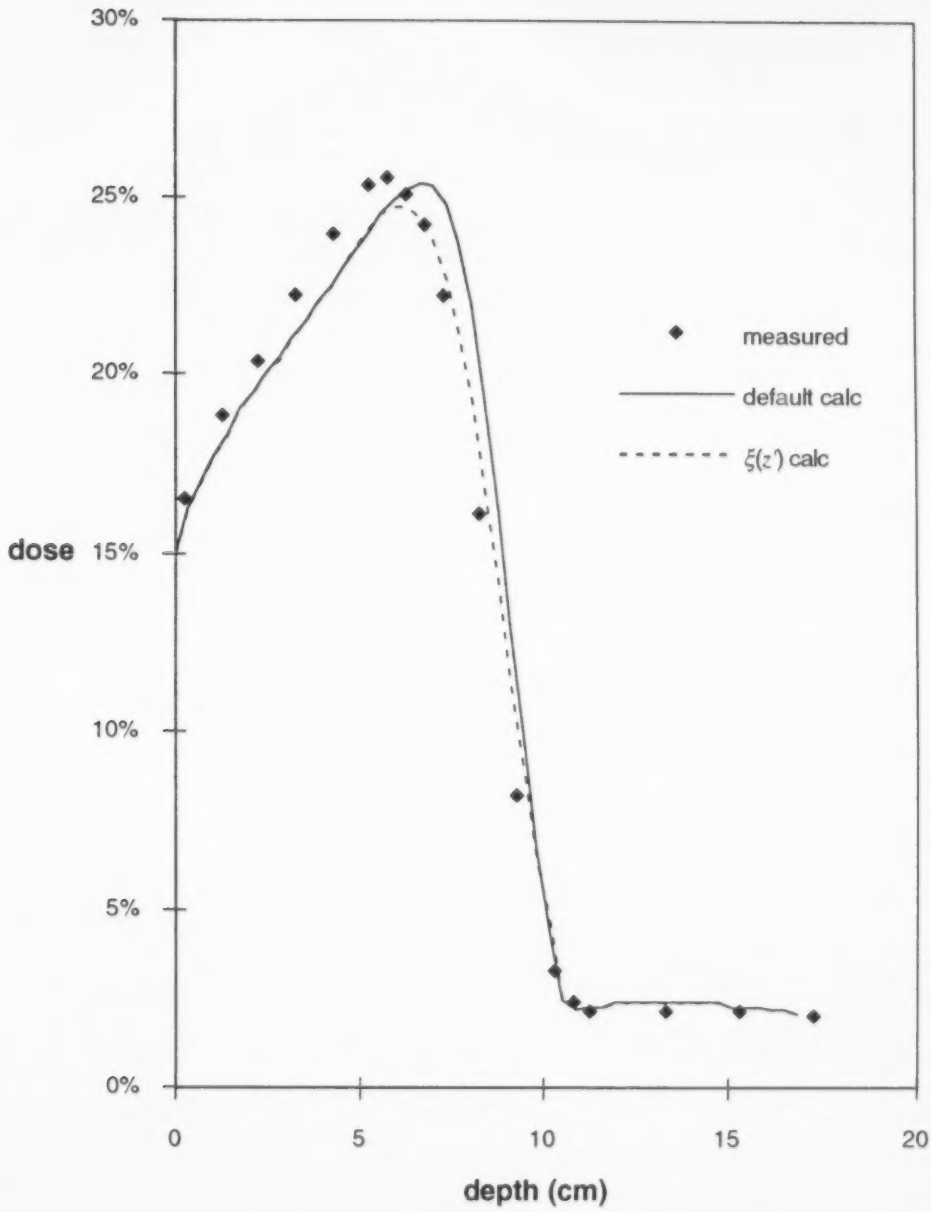

Figure V.15. Mid-arc percentage depth dose for a 20 MeV 90° arc on a 17.5 cm radius phantom. The discrete points are measured with a diode in a water phantom; the solid line is calculated using the default MDAH arc electron pencil beam algorithm; and the dashed line is calculated using $\xi(z')$.

discrete points are measured water data, and the solid line show the results of the MDAH arc electron pencil beam algorithm. It would also be expected that the scattering enhancement or reduction due to $\xi(z')$ should be mainly a function of the 'quality' of the beam, or its initial spectrum, and not very dependent on distance from the electron source. For this reason, the same $\xi(z')$ derived above for stationary beams, was used to modify the arc electron algorithm. The results are shown as the dashed lines in figures V.14 and V.15. The maximum output of the arced electron beam is slightly reduced, but the depth of maximum dose is also reduced, giving better agreement between calculation and measurement in the falloff region of the depth dose curve. This has a real clinical benefit since the depth at some level of the descending part of the depth dose curve (usually 80% of maximum dose) is chosen to cover the treatment volume. Figure V.16 also shows an improvement in the depth dose and isodose matching in the penumbral region for a 90° arc of 12 MeV electrons.

In figures V.13 through V.16, the amount of energy deposited by the MDAH algorithm using $\xi(z')$ is less than the amount of energy deposited by the default MDAH algorithm. This can be expected since we are decreasing the pencil beam width, and the total integral dose in the MDAH depends on the magnitude of the pencil beam width. The integral dose for a stationary beam incident on a semi-infinite phantom is

$$\mathcal{D} = \int_{-\infty}^{\infty} dx \int_{-\infty}^{\infty} dy \int_{0}^{\infty} dz \; D(x,y,z) \quad , \tag{V.30}$$

where $\mathcal{D}$ is the total dose deposited in the phantom, and $D(x,y,z)$ is the dose distribution due to the broad beam. If we assume the assume a non-devergent beam with dimensions $2A$ and $2B$ in the x and y directions, and unit incident planar fluence, then

$$D(x,y,z) = \int_{-B}^{B} dy' \int_{-A}^{A} dx' \; d(x-x',y-y',z) \quad , \tag{V.31}$$

where $d(x-x',y-y',z)$ is the pencil beam dose distribution. As we have seen above, the

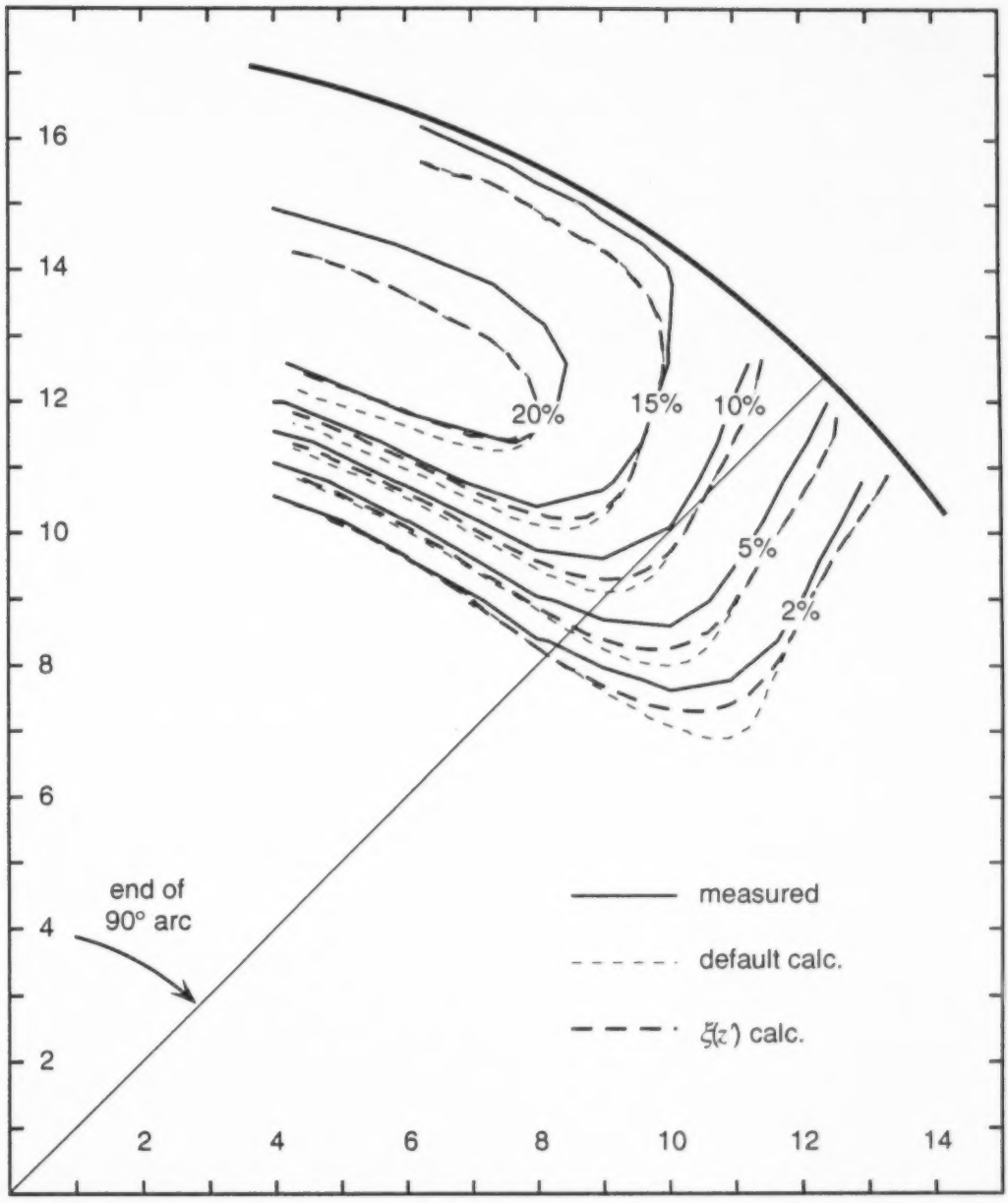

Figure V.16. Calculated and measured (film) isodose lines for a 90° arc of 12 MeV electrons incident on a 17.5 cm radius polystyrene phantom. The short dashed line is the default calculation, and the long dashed line is the new calculation, using $\xi(z')$.

MDAH algorithm assumes that

$$d(x-x',y-y',z) = f(x-x',y-y',z) \times g(z) \tag{V.32}$$

where $f(x-x',y-y',z)$ is the Gaussian planar fluence of the pencil beam at (x',y'), and $g(z)$ is the fluence to dose conversion factor. If we insert equations (V.31) and (V.32) into equation (V.30), the integration over dx and dy is unity, which leaves

$$\mathcal{D} = \int_0^\infty dz\ g(z) \int_{-B}^{B} dy' \int_{-A}^{A} dx' = 4AB \int_0^\infty dz\ g(z)\ . \tag{V.33}$$

The fluence to dose conversion factor, $g(z)$, depends on the reference depth dose, which is measured, and the pencil beam width. The dependence of $g(z)$ on the pencil beam width is such that if the pencil beam width is decreased, as for the *FMCS* modification, then $g(z)$ also decreases. This implies that the integral dose, $\mathcal{D}$, is smaller, which is consistent with our observations.

The *FMCS* modification method is a practical and reasonable solution to the problem of range straggling in electron beam treatment planning. Until other more accurate algorithms (redefinition, Monte Carlo…) become clinically acceptable with respect to computing time required, the added measured data needed to derive $\xi(z')$ is a small price to pay for the improved penumbral characteristics in stationary beams and easier output prediction for arced electron beams. The results of the Monte Carlo simulations in figures V.7–V.10 also indicate that the *FMCS* modification method should perform well for heterogeneous phantoms.

VI. Conclusion

This thesis has examined many aspects of electron beam dose measurements and calculations under various conditions. The first series of experiments with wax phantoms, evaluated the performance of the MDAH 2D pencil beam algorithm (Hogstrom *et al* 1981) for stationary beams. For aluminum and air heterogeneities, the discrepancies between measurement and calculation can be quite large in some cases. This is mainly due to the limitations of the 'central axis approximation' and the 2D nature of the algorithm.

For more reasonable high density heterogeneities, such as hard and soft bone analogs, the deviations between calculation and measurement are considerably smaller. The polystyrene phantom data also show the progression between 2D and 3D heterogeneities. For both calculation and measurement, the average rms deviation between the dose distributions for the 10 cm rod (calculation or measurement) and the dose distributions for the other length rods shows little variation after the rod length reaches approximately 4 cm for aluminum and 2 cm for hard and soft bone analogs. This implies that high density heterogeneities must be less than 2 cm in extent, for the 3D heterogeneity correction to have a significant effect. The effect of the 3D heterogeneity correction also decreases as the differences between the materials becomes smaller, as expected. For practical purposes, the above data can be used as a guideline for deciding on the necessity of a 3D heterogeneity correction in a given circumstance.

The last stationary beam investigation is a practical example of the use of the MDAH algorithm for treatment planning. For the neck irradiation, the variation in anatomy was not very great from one CT image to the next. The depth of the trachea and spinal cord are slowly varying with respect to the surface contour. Thus the 3D heterogeneity correction did not have a large effect in this case. However, the results do point out the need for the pencil beam calculation, taking scattering of the electrons into account. The shape and size of the beam modifier necessary to shield the spinal cord is vastly different if

scattering is ignored. The results also highlight a shortfall of the central axis approximation at depth. Because the pencil beams have spread out significantly at the depth of the trachea, the algorithm can only account for the trachea to first order, effectively becoming a broad beam ray tracing algorithm at depth.

The MDAH arc electron pencil beam algorithm shows great promise for treatment planning of electron arcs because the algorithm includes a heterogeneity correction similar to the stationary beam algorithm. Results show that the algorithm accurately predicts the dose distribution for an arced electron beam, provided that the multiple Coulomb scattering factor, *FMCS*, is adjusted properly. The calculated mid-arc depth doses show systematic deviations with measured depth doses. These deviations can be explained by the lack of a mechanism in Fermi-Eyges theory to allow for large angle scattering and range straggling of the electrons.

Both the stationary beam and arc electron calculation algorithms benefit from a more accurate description of the scattering process. Simple multiplicative corrections to the Fermi-Eyges pencil beam variance have been suggested (Werner *et al* 1982, Lax *et al* 1983), and a similar approach (replacing *FMCS*) gives good predictions of the pencil beam width in both homogeneous and heterogeneous phantoms, for Monte Carlo simulations. For stationary beams, the new range straggling correction gives much better agreement between calculation and measurement in the penumbral region. This implies that multiple beam treatment planning should give more accurate results. For arc electron beams, the *FMCS* replacement removes the ambiguity of the *FMCS* parameter and gives accurate predictions of the arc electron output. It is very straightforward to implement and should prove very useful for routine treatment planning.

Further work is needed to effectively unify the stationary beam and arc electron algorithms. The electron transport within the patient is handled almost identically, so this should be quite straightforward. The resulting algorithm should be able to handle most

routine electron treatment planning problems. For cases where there is concern about heterogeneities at depth, the redefinition algorithm (Shiu and Hogstrom 1987, 1989) could be used to give more accurate results. The redefinition algorithm can more accurately account for heterogeneities at greater depth than the normal MDAH algorithm. Because calculation times are prohibitive for routine planning, a compromise which may be sufficient in most cases, would be to modify the redefinition algorithm to allow for 2D heterogeneity corrections, if a significant speed advantage could be achieved.

The MDAH pencil beam algorithms give good dose predictions under many circumstances, and are very useful clinically. However, we need to be aware of circumstances where the dose calculations can systematically vary from the actual dose deposition. This allows for a better 'educated guess' as to the 'real' accuracy of the computed dose distribution. This thesis presents data showing some of the systematic errors involved in the theory and implementation of the MDAH algorithms. The implication for 3D treatment planning is that heterogeneities with an extent of greater than 2 cm will not show significantly different results with 2D and 3D heterogeneity corrections. This also implies that to do effective 3D treatment planning, CT information is required on a scale of less than 2 cm, and probably less than 1 cm. A real limitation in most cases is the ability to efficiently manipulate such large amounts of patient information, after it is obtained by the CT scanner. Surface and internal contours usually need to be obtained and this process is very time consuming, even with computer assistance. For this reason, better understanding of the applicability of 2D and 3D heterogeneity corrections is necessary to ensure that treatment planning time is used efficiently.

References

Antolak J, Mah E, Battista JJ and Scrimger JW 1988 Acquisition and display of radiation dose distributions using microcomputer technology *Med Phys* **15** 924-929

Antolak JA, Scrimger JW and Mah E 1992 Optimization of cord shielding technique for electrons *Aust Eng & Phys Sci in Med* (in press)

Battista JJ, Field C, Santon L and Barnett R 1984 Radiotherapy planning on a VAX-11/780 computer *Proc. 8th Int. Conf. on the Use of Computers in Radiotherapy* (New York: IEEE) pp 489-492

Bielajew AF and Rogers DWO 1986 *PRESTA-The Parameter Reduced Electron-Step Transport Algorithm for Electron Monte Carlo Transport, Report PIRS 0042* (Ottawa, Canada: NRCC)

Brahme A (ed.) 1983 *Computed electron beam dose planning* (Stockholm: Acta Radiologica suppl. 364)

Brahme A 1985 Correction for the angular dependence of a detector in electron and photon beams *Acta Radiol Onc* **24** 301-304

Brahme A and Svensson H 1976 Specification of electorn beam quality from the central axis depth absorbed dose distribution *Med Phys* **3** 95-102

Cygler J, Battista JJ, Scrimger JW, Mah E and Antolak J 1987 Electron dose distributions in experimental phantoms: A comparison with 2D pencil beam calculations *Phys Med Biol* **32** 1073-1086

Dutreix J and Dutreix A 1969 Film dosimetry of high energy electrons *Ann NY Acad Sci* **161** 33

El-Khatib E, Antolak JA, and Scrimger JW 1992 Radiation dose distributions for electron arc therapy using electrons of 6–20 MeV *Phys Med Biol* (in press)

El-Khatib E, Scrimger JW, and Murray B 1991 Reduction of the bremsstrahlung component of clinical electron beams: Implications for electron arc therapy and total skin electron irradiation *Phys Med Biol* **36** 111-118

Eyges L 1948 Multiple scattering with energy loss *Phys Rev* **74** 1534-1535

Hall EJ 1988 *Radiobiology for the Radiobiologist* (Philadelphia, USA: Lippincott)

Harder D 1965, cited in Hogstrom *et al* 1981

Hogstrom KR 1987 Evaluation of electron pencil beam dose calculation *Radiation Oncology Physics* (Medical Physics Monograph No 15) ed. Kereiakes JG, Elson HR, and Born CG (New York: American Institute of Physics) 532-557

Hogstrom KR and Almond PR 1983 Comparison of experimental and calculated dose distributions *Computed Electron Beam Dose Planning, Acta Radiol.* **suppl. 364** 89-99

Hogstrom KR, Kurup RG, Shiu AS and Starkschall G 1989 A two-dimensional pencil-beam algorithm for calculation of arc electron dose distributions *Phys Med Biol* **34** 315-341

Hogstrom KR, Mills MD and Almond PR, 1981 Electron beam dose calculations *Phys Med Biol* **26** 445-459

Hogstrom KR, Mills MD, Meyer JA, Palta JR, Mellenberg DE, Meoz RT and Fields RS 1984 Dosimetric evaluation of a pencil-beam algorithm for electrons employing a two-dimensional heterogeneity correction *Int J Rad Oncol Biol Phys* **10** 561-569

ICRU 1984a *Radiation Dosimetry: Electron Beams with Energies Between* 1 *and* 50 *MeV* Report 35 (USA: ICRU)

ICRU 1984b *Stopping Powers of Electrons and Positrons* Report 37 (USA: ICRU)

Jette D 1991 Electron dose calculation using multiple scattering theory: Localized inhomogeneities—A new theory *Med Phys* **18** 123-132

Jette D and Bielajew AF 1989 Electron dose calculations using multiple-scattering theory: second-order multiple-scattering theory *Med Phys* **16** 698-711

Kurup RG, Hogstrom KR, Otte VA, Moyers MF, Tung S and Shiu AS 1992 Dosimetric evaluation of a two-dimensional, arc electron, pencil-beam algorithm in water and PMMA *Phys Med Biol* **37** 127-144

Lax I 1986 Development of a generalized Gaussian model for absorbed dose calculation and dose planning in therapeutic electron beams *PhD thesis* University of Stockholm

Lax I, Brahme A and Andreo P 1983 Electron beam dose planning using Gaussian beams—improved radial dose profiles *Acta Radiol Suppl.* **364** 49-59

Leavitt DD, Peacock LM, Gibbs FA, and Stewart JR 1985 Electron arc therapy: Physical measurements and treatment planning techniques *Int. J. Rad. Oncol. Biol. Phys.* **11** 987-999

Low DA, Starkschall G, Bujnowski SW, Wang LL, and Hogstrom KR 1992 Electron bolus design for radiotherapy treatment planning: Bolus design algorithms *Med Phys* **19** 115-124

Mackie TR, Kubsad SS, Bielajew AF, and Rogers DWO 1990 The OMEGA Project: Electron dose planning using Monte Carlo simulation *Med Phys* **14** 732 (abstract)

Mah E, Antolak J, Scrimger JW and Battista JJ 1989 Experimental evaluation of a 2D and 3D electron pencil beam algorithm *Phys Med Biol* **34** 1179-1194

Markus B 1961 *Strahlentherapie* **116** 280

Mott NF 1929, cited in Rossi and Greissen 1941

Nelson WR, Hirayama H and Rogers DWO 1985 *The EGS4 Code System, SLAC-265* (Stanford, California: Stanford University)

Pla M, Pla C, and Podgorsak EB 1988 The influence of beam parameters on percentage depth dose in electron arc therapy *Med Phys* **15** 49-55

Pla M, Podgorsak EB, Pla C, Freeman CR, Souhami L, and Guerra J 1989 Physical aspects of the angle-ß concept in electron arc therapy *Int J Rad Oncol Biol Phys* **20** 1331-1339

Rikner G 1985 Characteristics of a p-Si detector in high energy electron fields *Acta Radiol Onc* **24** 71-74

Rikner G and Grusell E 1987 General specifications for silicon semiconductors for use in radiation dosimetry *Phys Med Biol* **32** 1109-1117

Rossi B and Greissen K 1941 Cosmic-Ray Theory *Rev. Mod. Phys.* **13** 240-309

Sandison GA, Huda W, Savoie D and Battista JJ 1989 Comparison of methods to determine electron pencil beam spread in tissue equivalent media *Med Phys* **16** 881-888

Shiu AS and Hogstrom KR 1987 A pencil-beam redefinition algorithm for electron dose distributions *Proc. 9th Int. Conf. on the Use of Computers in Radiotherapy* (New York: IEEE) pp 69-72

Shiu AS and Hogstrom KR 1991 Pencil-beam redefinition algorithm for electron dose distributions *Med Phys* **18** 7-18

Späth H 1974 *Spline Algorithms for Curves and Surfaces* (Winnipeg, Canada: Utilitas Mathematical Publishing) (translated from German original, *Spline–Algorithmen zur Konstruktion glatter Kurven und Flächen*, 1973)

Starkschall G, Shiu AS, Bujnowski SW, Wang LL, Low DA and Hogstrom KR 1991 Effect of dimensionality of heterogeneity correction on three-dimensional electron pencil-beam calculations *Phys Med Biol* **36** 207-227

Storchi PRM and Huizenga H 1985 On a numerical approach of the pencil beam model *Phys Med Biol* **30** 467-473

Werner BL, Khan FM and Deibel FC 1982 A model for calculating electron beam scattering in treatment planning *Med Phys* **9** 180-187